High power ultra-short pulse lasers based on fiber driven OPCPA

Dissertation

zur Erlangung des akademischen Grades

doctor rerum naturalium (Dr. rer. nat.)

vorgelegt dem Rat der Physikalisch-Astronomischen Fakultät,
der Friedrich-Schiller-Universität Jena

von Dipl.-Phys. Jan Rothhardt

geboren am 20. November 1981 in Jena

Gutachter

1. Prof. Dr. Andreas Tünnermann
2. Prof. Dr. Christian Spielmann
3. Prof. Dr. Uwe Morgner

Tag der Disputation: 29.11.2010

Contents

1 Introduction

Ultra-short laser pulses allow for groundbreaking studies in the femtosecond timescale such as spectroscopy [1], triggering and tracing chemical reactions [2] or optical metrology [3]. In addition, intense ultra-short laser pulses enable phenomena in high field physics, such as high order harmonic generation (HHG) [4], which have attracted great interest in the scientific community in the last years. The outstanding properties of the generated radiation in the extreme ultra violet (XUV) wavelength range allow for exciting applications such as the study of molecular motion [5], new high resolution XUV imaging techniques [6] or investigation of surface processes [7]. Furthermore, by applying extremely short laser pulses containing only a few optical cycles [8], isolated pulses have been generated in the XUV with pulse durations as short as 80 as [9]. Such pulses allow for real-time observation of electronic motion in atoms and molecules, leading to a new field of research named attoscience [10].

However, many ultra-fast processes have very small probabilities of occurrence. In addition, applications of laser generated XUV radiation suffer from the low conversion efficiency of HHG, which is typically of the order of 10^{-6}. As a result, the photon flux is low and sophisticated detectors and long integration times are required. Consequently, a higher laser repetition rate and average output power is desired, in order to improve the performance of current ultra-fast studies. In addition, such laser systems will also pave the way for new exciting applications. As an example, seeding of free electron lasers, such as FLASH [11] with laser generated XUV light [12] will significantly improve the stability and brilliance as well as spectral and temporal properties of the amplified radiation, but requires a driving laser which operates at a very high repetition rate.

Since nearly two decades, ultra-fast science relies on Kerr-lens mode-locked Ti:Sa lasers [13]. Today, pulses shorter than two optical cycles can be delivered directly by the oscillator [14]. Furthermore, table-top high peak power amplifier systems based on Ti:Sa technology are commercially available and employed by a broad scientific community. Unfortunately, conventional Ti:Sa systems do not support few-cycle pulse durations directly from the amplifier due to gain narrowing effects. Nevertheless, few-cycle pulses can be generated by applying hollow fiber or filament based post compression schemes [15, 8, 16]. However, these techniques are accompanied with additional losses and are limited in scalability. Furthermore, the average output power of the Ti:Sa based laser is itself limited due to thermo-optical effects. Even with sophisticated cryogenic cooling of the laser medium, several ten watts of output power have not been exceeded so far [17].

A different approach for amplification of ultra-short laser pulses is optical parametric am-

plification. Under certain circumstances an optical parametric amplifier (OPA) can provide very large amplification bandwidths, supporting few-cycle pulse durations. Pulses as short as 3.9 fs have already been achieved using this approach [18]. Merging the technique of chirped pulse amplification (CPA) with an optical parametric amplifier reveals a powerful laser concept, named optical parametric chirped pulse amplification (OPCPA), first demonstrated by Dubietis et al. in 1992 [19]. Since then, remarkable progress has been achieved in the development of OPCPA based laser systems [20, 21, 22]. In particular, the pulse peak power of few-cycle laser pulses has been boosted to 10 TW recently [23], demonstrating the virtue of the OPCPA concept.

In contrast to Ti:Sa lasers and amplifiers, negligible absorption and absence of energy storage in the nonlinear medium lead to a strongly reduced thermal load. Hence, OPCPA is a promising concept for amplification of ultra-short optical pulses to unprecedented average power levels. For this purpose a suitable high power pump laser is required. Although, thermo-optical effects limit power scaling of conventional rod laser designs, advanced geometries such as thin-disk, slab and fiber reduce thermal issues clearly. In addition, diode pumped Yb-based lasers provide enhanced optical-to-optical efficiency. Nearly 10 kW average power with diffraction limited beam quality are delivered by continuous wave Yb-doped fiber lasers nowadays [24], demonstrating their suitability for high average output powers. In addition, 830 W of average power have been demonstrated with a femtosecond Yb-doped fiber laser recently [25]. Such laser systems typically deliver pulses with several hundreds of femtoseconds pulse duration which are suitable pump pulses for few-cycle OPCPA systems.

Application of a femtosecond Yb-doped fiber laser as pump for OPCPA has already been demonstrated before this work. However, the achieved laser parameters of sub-microjoule pulse energy and 46 fs pulse duration cast a pulse peak power of only 10 MW [26] at below 1 W of average output power. For applications in high field physics the pulse peak power has to be increased by more than two orders of magnitude. Furthermore, significant increase in average power is desired.

The objective of this thesis is to develop ultra-short pulse lasers, simultaneously providing sufficient peak power for high field applications and high average power. Additionally, pulse durations in the few-cycle regime are desired. This is achieved by merging OPCPA technology with state-of-the-art Yb-doped fiber based pump lasers.

The thesis is structured as follows: At first, current ultra-short pulse laser technology is briefly introduced and the special properties of OPCPA are discussed. The following chapter introduces the basic theoretical descriptions for ultra-short pulses in linear and nonlinear media. Chapter 4 is focused on numerical modeling of the OPA, to achieve the largest amplification bandwidth as well as the highest conversion efficiency. In consequence, suitable nonlinear crystals and configurations as well as requirements on the pump laser are defined. The main properties of Yb-doped fiber lasers and amplifiers will be briefly introduced in chapter 5. In addition, two high power fiber laser systems are presented which will serve

as pumps for OPCPA at a later stage. A state-of-the-art fiber based femtosecond laser system is adapted and improved to serve as OPCPA pump and a nanosecond fiber amplifier is developed, as an alternative compact pump laser.

The main experimental task of this thesis is the design and assembly of three OPCPA laser systems, operating at different wavelengths and with different pulse parameters. Chapter 6 presents these laser systems and summarizes the experimental results, including a detailed characterization of the performance. In addition, high harmonic generation is demonstrated in a Krypton gas target, highlighting the great potential of these unique laser sources. The scaling potential of the developed laser systems and new concepts for the combining of multiple pumps are discussed in chapter 7. Finally, the thesis is summarized and a short outlook of potential future developments is given.

2 Few-cycle laser technology

2.1 Ti:Sa based few-cycle lasers

Today, few-cycle laser pulses as short as 5 fs are delivered directly by Ti:Sa oscillators [14]. Amplification of such pulses in Ti:Sa based amplifiers yields pulse energies of 28 J and peak powers approaching the petawatt level [27]. However, gain narrowing in the amplifiers reduces the spectral bandwidth severely, and sub-20 fs are typically not achieved. Nevertheless, active control of the spectral intensity can precompensate gain narrowing to a certain extend, and 10 fs pulse duration has been obtained with 3.5 mJ pulses [28]. Commercially available Ti:Sa amplifier systems, which are usually employed for ultra-fast studies, deliver ∼25 fs pulses with ∼1 mJ pulse energy at a repetition rate of ∼1 kHz [29]. However, the pulse durations of such laser systems can be significantly reduced by hollow fiber or filament based post-compression schemes . First experiments employing spectral broadening in a Krypton-filled hollow fiber and subsequent dechirping produced 20 µJ pulses as short as 4.5 fs [15]. This technique nowadays routinely generates 5 fs pulses with several hundred microjoule pulse energy, using chirped mirror pulse compression [8]. However, further scaling in pulse energy is hindered by occurrence of self-focusing and ionization of the gas medium near or around the entrance of the fiber, which degrades the coupling between the laser beam and the hollow fiber. Nevertheless, chirped input pulses and a differentially pumped Neon-filled hollow fiber could reduce these problems to a certain extend, and 3.7 fs pulse with 1.2 mJ pulse energy have been achieved recently [30]. In addition, it must be mentioned that perfect laser beam quality is required for efficient coupling to the hollow fiber. In consequence, scaling to higher average power remains challenging and the average power of hollow fiber based few-cycle lasers has not exceeded the watt level so far.

A second approach for pulse compression is based on filaments which allow to maintain high intensities in gaseous media over a long interaction length, hence resulting in efficient spectral broadening. These filaments are mainly formed by balance of two nonlinear effects, self-focusing due to the optical Kerr effect and defocusing which is caused by the generated plasma. With this technique, pulses with 5.7 fs duration and 380 µJ energy have been achieved [16]. When using a more complex two stage compression scheme, 180 µJ pulses as short as 5.1 fs have been generated . Detailed experimental studies using an Argon gas cell revealed that increasing the pulse energies beyond ∼0.8 mJ did not generate further spectral bandwidth due to saturation effects. In addition, the recompressed pulse duration is increased and the pulse quality of the compressed output pulses is reduced. This effect is

attributed to a nonlinear phase which is imposed onto the spectrum and cannot be compensated by the chirped mirror compressor [31]. In addition, scaling to higher pulse energies is also limited due to multiple filament formation. Furthermore, beam pointing instabilities which are caused by thermal density fluctuations in the gas cell are an inherent problem of white light filaments.

In general, both methods of few-cycle pulse compression rely on Ti:Sa based lasers and scaling of these lasers to higher average power is limited due to thermo-optical effects. Although cryogenic cooling helps to reduce these effects, the output power of Ti:Sa based lasers is currently limited to several ten watts. Hence, an alternative power scalable concept for amplification of few-cycle pulses is desirable. It is found in optical parametric chirped pulse amplification, which will be introduced in the next section.

2.2 Optical parametric chirped pulse amplification

Optical parametric amplification is an alternative concept for few-cycle pulse amplification. Pulses as short as 3.9 fs have been achieved with an OPA so far [18]. In principle, the OPA is scalable both in average power and pulse energy. However, the highest pulse energies can be achieved with the concept of optical parametric chirped pulse amplification (OPCPA), which is illustrated in fig. 2.1. Generally, a broadband seed is generated, chirped by a pulse stretcher, parametrically amplified in a nonlinear crystal and recompressed by means of a pulse compressor. Additionally, a pump laser is required to drive the parametric amplifier[1]. Clearly, OPCPA provides multiple advantages compared to Ti:Sa laser technology. Nonetheless, some properties can also become challenges in OPCPA development. Both challenges and advantages will be briefly discussed in the following section of this thesis.

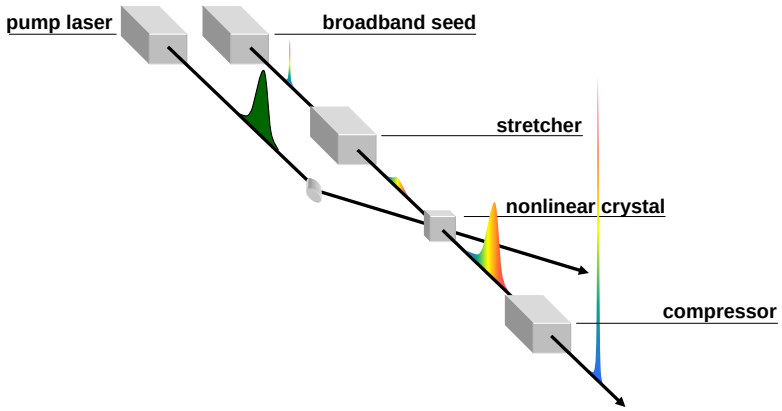

Figure 2.1 – Principle setup of an OPCPA system.

[1] In this thesis, the high energy pump pulses are generated with seeded amplifiers. Throughout this thesis, the expression "pump laser" includes seeded amplifier systems which emit coherent light.

Advantages

- gain bandwidth: Optical parametric amplifiers possess a large amplification bandwidth, which supports the amplification of few-cycle pulses under certain circumstances. In order to achieve the largest amplification bandwidth an optimized noncollinear configuration is required and very short nonlinear crystals have to be employed.
- single pass gain: The single pass gain can reach several orders of magnitude with only a few millimeters of crystal length, superseeding complicated multipass configurations.
- high power capability: Optical parametric amplification is not accompanied by energy storage in the medium. Since the residual absorption of the interacting light waves in the crystal is very low, the thermal load is typically negligible. In consequence, the optical parametric amplifier is average power scalable and the average output power is mainly defined by the pump laser.

Challenges

- phase matching: In order to achieve efficient conversion in the parametric amplifier, the interacting optical waves have to be phase matched. In that regard, nonlinear crystals hold several degrees of freedom but also require precise alignment and pointing stability of the interacting beams.
- pump requirements: The requirements on the pump laser are demanding. The concept of OPCPA transfers the main part of thermal problems to the pump laser, since it should deliver the highest possible energy and average power. In addition, the pump pulses have to be precisely temporally synchronized with the signal pulses. Furthermore, high temporal and spatial quality of the pump is desired, since intensity modulations are transferred onto the amplified signal.
- stretching and compression: To ensure efficient energy transfer from pump to signal, their pulse durations have to be matched. While nanosecond pump pulses require a large stretching ratio for the signal, the demands on stretcher and compressor are relaxed when using pico- or femtosecond pump pulses.
- efficiency: In theory, the pump can be depleted completely. In practice, the non-uniform temporal and spatial profiles of signal and pump reduce the overall efficiency. Additionally, a part of the energy is transferred to a third, typically undesired wave, which is called the idler wave. Nevertheless, about 20 % conversion efficiency from pump to signal are usually achieved.
- polarization: A specific polarization state is required for signal and pump to participate in the nonlinear process. On the other hand the polarization is inherently determined at the output of the OPA, which could be beneficial for certain applications.

- parasitic nonlinear effects: Parasitic nonlinear effects, such as second harmonic generation of signal or idler wave, are usually undesired. They have to be avoided which is especially challenging for ultra-broad signal spectra.

These special properties of OPCPA will be considered within this thesis in order to fulfill the numerous requirements but also to exploit the full potential of the OPCPA approach. Numerical modeling will address gain limitations, phase matching and gain bandwidth optimization, improvement of conversion efficiency as well as suppression of parasitic nonlinear effects. Yb-doped fiber lasers will be employed as high power pump lasers according to the pump laser requirements. In addition, broadband signal generation, stretching and recompression will be achieved by different approaches in each OPCPA system, respectively. Furthermore, experiments will demonstrate the potential of the OPCPA concept for high power intense few-cycle laser systems and finally the scaling potential will be discussed. However, at first the basic theoretical descriptions for ultra-short pulses in linear and nonlinear media will be introduced in the next chapter of this thesis.

3 Linear and nonlinear optics of ultra-short laser pulses

Generally, optics describes the generation, propagation and detection of light. Most phenomena can be accounted for by a classical electromagnetic description. However, light can also be seen as particles (photons), which is subject of quantum optics. Anyway, a simplified description of light by electromagnetic waves is sufficient in many cases.

The propagation of light is governed by the interaction with the medium. In the electromagnetic description the response of the medium is governed by the macroscopic polarization $\mathbf{P}$. When an electric field $\mathbf{E}$ is applied, it can be expressed as a Taylor expansion in $\mathbf{E}$:

$$\frac{\mathbf{P}}{\epsilon_0} = \chi^{(\mathbf{1})} \cdot \mathbf{E} + \chi^{(\mathbf{2})} : \mathbf{E} + \chi^{(\mathbf{3})} \vdots \mathbf{E} + \dots . \tag{3.1}$$

The first term is related to linear optics, where the properties of matter do not depend on the intensity of light, which is the case for low intensities. In transparent media, the linear refractive index is related to the real part of the linear electric susceptibility $\chi^{(1)}$ by the following expression:

$$n(\omega) = 1 + \frac{1}{2} Re[\chi^{(1)}(\omega)]. \tag{3.2}$$

As a consequence of the frequency dependent material response, the phase velocity $c = {}^{c_0}/_{n(\omega)}$ and the wave vector $|\mathbf{k}| = {}^{\omega}/_{c}$ of a propagating wave are frequency dependent, where the vacuum speed of light $c_0 = (\mu_0 \epsilon_0)^{-1/2}$ is given by the vacuum electric and magnetic permittivities ϵ_0 and μ_0. In consequence, the propagation of ultra-short laser pulses is strongly influenced by dispersion of the group velocity, which is described in the second section of this chapter.

At high intensities of light, which can especially be achieved with laser pulses, the optical parameters of the material become functions of the intensity and nonlinear effects of various orders can be observed. In a classical view, a high intensity of light, applied to a transparent medium, leads to large oscillation amplitudes of the bound electrons. Therefore, these oscillations become strongly anharmonic, which causes the emission of new frequencies. In a dipole approximation of the electron-photon interaction, the second (third) order susceptibility is a third (fourth)-order tensor, whose components represent various orientations of the medium and the polarization of the interacting waves.

Two important second order nonlinear effects, which are strongly related to this work, are

second harmonic generation and optical parametric amplification. They will be introduced in the second part of this chapter. It is worth mentioning, that in media with inversion symmetry $\chi^{(2)}$ is identical to zero. In this case third order nonlinear effects, such as the optical Kerr-effect are most relevant. They will be discussed later, in chapter 5, as these effects heavily influence the propagation of ultra-short pulses in fused silica fibers and fiber amplifiers.

3.1 Ultra-short laser pulses

In optics, an ultra-short light pulse is an electromagnetic pulse, whose time duration is of the order of femtoseconds to picoseconds. Such pulses are composed of a broad spectrum of optical frequencies and can be described as a Fourier synthesis of monochromatic waves [32]. In consequence, the frequency bandwidth $\Delta\upsilon$ and the duration Δt of a laser pulse are linked. Their so called time bandwidth product (TBP), meets the following uncertainty relation

$$\Delta t \Delta\upsilon \geqq K \tag{3.3}$$

The minimum time-bandwidth product K is shown in tab. 3.2 for various pulse shapes. For practical reasons, the full width at half-maximum (FWHM) of the intensities in frequency $\Delta\upsilon$ and temporal domain Δt is used. Equality with the minimum TBP is only achieved for the so-called Fourier transform limited pulse, with a time independent instantaneous frequency (unchirped pulse). A meaningful measure for the pulse quality is the Strehl ratio, which is defined as the achieved pulse peak power divided by the peak power of the Fourier limited pulse [33].

Shape	I(t)	K
Gaussian	$e^{[-(2t/t_0)^2]}$	0.441
Hyperbolic secant	$\frac{1}{\cosh^2(t/t_0)}$	0.315
Rectangle	$1\ \lvert t\rvert > t_0$	0.892

Table 3.2 – Minimum time bandwidth product for various pulse shapes. ($I(t)$ represents the intensity envelope) [32].

3.2 Dispersion

In dispersive media, the wave vector $\mathbf{k}$ is frequency dependent, meaning that every spectral component travels with a different phase velocity. This is especially relevant for the propagation of ultra-short laser pulses due to their large spectral bandwidth.

In order to describe the influence of dispersion on ultra-short pulse propagation, the wave vector can be expressed as a Taylor expansion around the central angular frequency ω_0, when assuming that the angular frequency bandwidth $\Delta\omega$ is much smaller than ω_0 ($\Delta\omega \ll \omega_0$)[34]:

$$k(\omega) = k_0 + \frac{\partial k}{\partial \omega}(\omega - \omega_0) + \frac{1}{2}\frac{\partial^2 k}{\partial \omega^2}(\omega - \omega_0)^2 + \frac{1}{6}\frac{\partial^3 \varphi}{\partial \omega^3}(\omega - \omega_0)^3 + \dots . \tag{3.4}$$

The zero order term describes a phase shift, related to the phase velocity at ω_0, while $\partial k/\partial\omega = 1/v_g$ is the inverse group velocity, the second order term $\beta^{(2)} = \partial^2 k/\partial\omega^2$ is the group velocity dispersion (GVD), $\beta^{(3)} = \partial^3 k/\partial\omega^3$ is named third order dispersion (TOD). Dispersion effects become relevant on length scales of the dispersive length, which is defined as

$$L_D = \frac{t_0^2}{|\beta^{(2)}|}, \tag{3.5}$$

where t_0 is the pulse duration [35]. Certainly, the properties of a laser pulse are seriously changed in presence of dispersion. A transform limited pulse, which has a time independent instantaneous frequency (no frequency chirp) is shown in fig. 3.1a. Positive GVD, for example, leads to a positive linear chirp, meaning that the long (short) wavelength components are found in the leading (trailing) edge of the pulse as illustrated in fig. 3.1b. Consequently, the pulse duration is usually increased and the pulse peak power is reduced.[1] In order to obtain the shortest and most intense pulses from an ultra-short pulse laser system, precise dispersion management is required. Note that throughout this thesis positive dispersion is defined by $\beta^{(2)} > 0$ and negative dispersion by $\beta^{(2)} < 0$. In consequence, for positive (negatives) dispersion the group velocity decreases (increases) with increasing optical frequency. Most transparent media provide positive dispersion in the visible spectral region, while negative dispersion typically occurs at longer wavelengths, e.g. in fused silica for wavelengths longer than approx. 1.3 µm.

3.3 $\chi^{(2)}$-effects

At the beginning of this section, the general mathematical description for monochromatic plane wave interactions in $\chi^{(2)}$ media is introduced. Then, the principles of second harmonic

[1] For Gaussian and sech^2 pulses the shortest pulse is obtained in the transform limited case. However this is not necessarily true for arbitrary pulse shapes and additionally depends on the measure of the pulse duration.

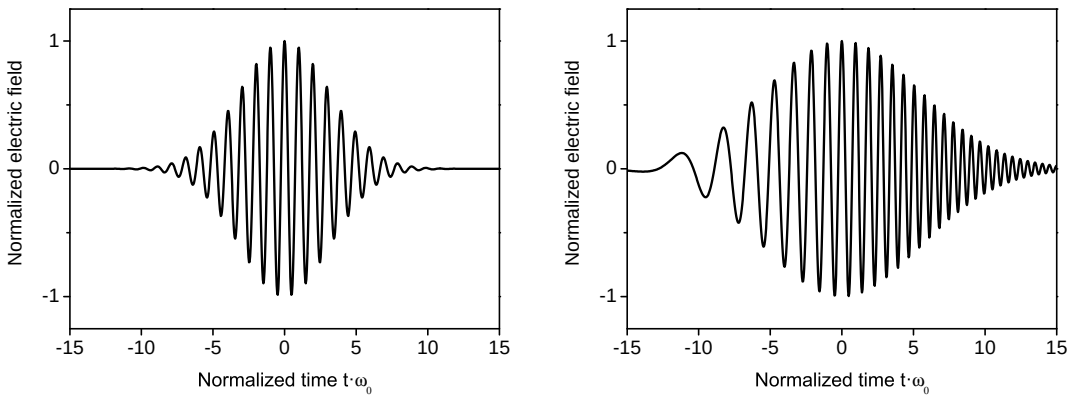

(a) **(b)**

Figure 3.1 – Normalized electric field of a) a transform-limited ultra-short laser pulse b) an ultra-short laser pulse which is linearly chirped by positive GVD.

generation and optical parametric amplification are described. The next subsection deals with phase matching and its influence on the nonlinear process. The nonlinear interaction of real optical beams, with divergence and finite transverse dimension, is subject of the fourth subsection. Finally, the spectral bandwidth of the nonlinear process as well as dispersive and group velocity effects are discussed, which are of great importance for ultra-short laser pulses.

3.3.1 General description

The propagation of electromagnetic waves can be described by a wave-equation, directly derived from Maxwell's equations [36]:

$$\left[\nabla \times (\nabla \times) + \frac{1}{c_0^2}\frac{\partial^2}{\partial t^2}\right]\mathbf{E}(\mathbf{r},\mathrm{t}) = -\frac{1}{\epsilon_0 c_0^2}\frac{\partial^2}{\partial t^2}\mathbf{P}(\mathbf{r},\mathrm{t}). \tag{3.6}$$

Decomposition of the vector field in linearly polarized plane waves, propagating along the z-axis, and Fourier transform into the frequency domain leads to a set of wave equations, which are coupled by the nonlinear polarization. For practical reasons the pulse envelope $A(z)$ is separated from the rapid oscillating term and each monochromatic, linearly polarized, electrical field can be written as

$$E(z,t) = A(z)e^{i(kz-\omega t)} + c.c.. \tag{3.7}$$

By using the slowly varying envelope approximation $\left|\frac{\partial^2 A}{\partial z^2} \ll 2k\frac{\partial A}{\partial z}\right|$ and ignoring the backward generated waves, a set of coupled wave equations for the amplitudes of the interacting plane waves can be found. For further simplification, negligible absorption is assumed. The strength of the nonlinear interaction is described by the effective nonlinear coefficient d_{eff}. It is

a scalar, which is contracted from the $\chi^{(2)}$-tensor, typically consisting of a sum of terms, determined by the polarization of the interacting waves and the orientation of the nonlinear crystal. Detailed information on this topic can be found e.g. in [36]. The intensity of each wave, which is the quantity of interest in nonlinear optics, is calculated from the electric field amplitude by

$$I(z) = 2\epsilon_0 c_0 n |A(z)|^2. \tag{3.8}$$

3.3.2 Second harmonic generation

Second harmonic generation (SHG) was the first frequency mixing effect to be observed after the invention of the laser [37]. In the photon model it is a mixing process of two photons with the same angular frequency ω, giving rise to a single photon with the frequency 2ω. For this specific case, the coupled differential equations for the fundamental field and the second harmonic, propagating along the z-axis, are [36]

$$\frac{dA_\omega}{dz} = i\frac{2\omega}{n(\omega)c_0} d_{eff} A_\omega^* A_{2\omega} e^{-i\Delta k z}, \tag{3.9}$$

$$\frac{dA_{2\omega}}{dz} = i\frac{2\omega}{n(2\omega)c_0} d_{eff} A_\omega^2 e^{i\Delta k z}, \tag{3.10}$$

where $\Delta k = 2k_\omega$-$k_{2\omega}$ is the wave vector mismatch. In case of perfect phase matching ($\Delta k = 0$), efficient energy transfer is possible and an analytical solution for the intensities can be found [36]:

$$\begin{aligned} I_\omega(z) &= I_\omega(0)\mathrm{sech}^2(z/l_{SH}), \\ I_{2\omega}(z) &= I_\omega(0)\tanh^2(z/l_{SH}) \end{aligned} \tag{3.11}$$

with

$$l_{SH} = \frac{1}{4\pi d_{eff}} \sqrt{\frac{2\epsilon_0 n(\omega)^2 n(2\omega)^2 c_0 \lambda_\omega^2}{I_\omega(0)}}. \tag{3.12}$$

In this thesis, second harmonic generation of Yb-doped fiber laser systems is exploited to generate the pump for OPCPA.

3.3.3 Optical parametric amplification

An optical parametric amplifier (OPA) is based on three-wave mixing in a nonlinear crystal. Typically, a signal wave (ω_s) is amplified while a pump wave is depleted (ω_p). The remaining energy is transferred to an idler wave with the angular frequency $\omega_i = \omega_p - \omega_s$. If three interacting waves propagating collinearly along the z-axis are assumed, the coupled wave equations for the slowly varying envelopes can be found as [36, 20]

$$\frac{dA_i}{dz} = i\frac{\omega_i d_{eff}}{n(\omega_i)c_0} A_s^* A_p e^{i\Delta k z}, \tag{3.13}$$

$$\frac{dA_s}{dz} = i\frac{\omega_s d_{eff}}{n(\omega_s)c_0} A_i^* A_p e^{i\Delta kz}, \tag{3.14}$$

$$\frac{dA_p}{dz} = i\frac{\omega_p d_{eff}}{n(\omega_p)c_0} A_i A_s e^{-i\Delta kz}, \tag{3.15}$$

where $\Delta k = k_p - k_i - k_s$ is the wave vector mismatch for that process. For negligible pump depletion ($A_p \simeq$ const.) an analytical solution for signal and idler intensity is found:

$$I_s(z) = I_s(0)\left[1 + \frac{\Gamma^2}{g^2}\sinh^2(gz)\right], \tag{3.16}$$

$$I_i(z) = I_s(0)\frac{\omega_i}{\omega_s}\frac{\Gamma^2}{g^2}\sinh^2(gz), \tag{3.17}$$

if no initial idler is assumed ($I_i(0) = 0$) and the gain parameter g is defined as:

$$g = \sqrt{\Gamma^2 - \left(\frac{\Delta k}{2}\right)^2}, \tag{3.18}$$

$$\Gamma^2 = \frac{2\omega_i\omega_s d_{eff}^2 I_p}{n_i n_s n_p \epsilon_0 c_0^3}. \tag{3.19}$$

The parametric gain of the signal G is defined as:

$$G = \frac{I_s(z)}{I_s(0)}. \tag{3.20}$$

As an example, the parametric gain for a λ_s=800 nm signal is displayed in fig. 3.2a versus the pump intensity (λ_p=515 nm) for various crystal lengths. The effective nonlinear coefficient has been chosen to represent the widely used nonlinear material BBO[2], ($d_{eff} = 2.1$ pm/V). It can be seen that an enormous single pass gain can be achieved with only a few millimeters of crystal length. E.g. at 50 GW/cm^2 pump intensity and 3 mm crystal length a gain factor larger than 10^8 is achieved.

Optical parametric generation, parametric fluorescence and optical parametric oscillator

The high gain factor of a parametric amplifier enables amplification of spontaneously emitted photons which arise from vacuum fluctuations of the electric field interacting with the pump field [36]. The spontaneous effect is called optical parametric generation (OPG), while the amplified radiation, that will peak at the frequency and direction of best phase matching, is called parametric fluorescence. If the OPG crystal is enclosed in a suitable cavity and the parametric gain exceeds the losses of a cavity round-trip an optical parametric oscillator (OPO) will be obtained. On the one hand, due to the resonant enhancement in the cavity OPOs can be pumped by small-scale oscillators at very high repetition rates (∼100 MHz).

[2]Beta barium borate (β-barium borate, BBO or β-BaB_2O_4)

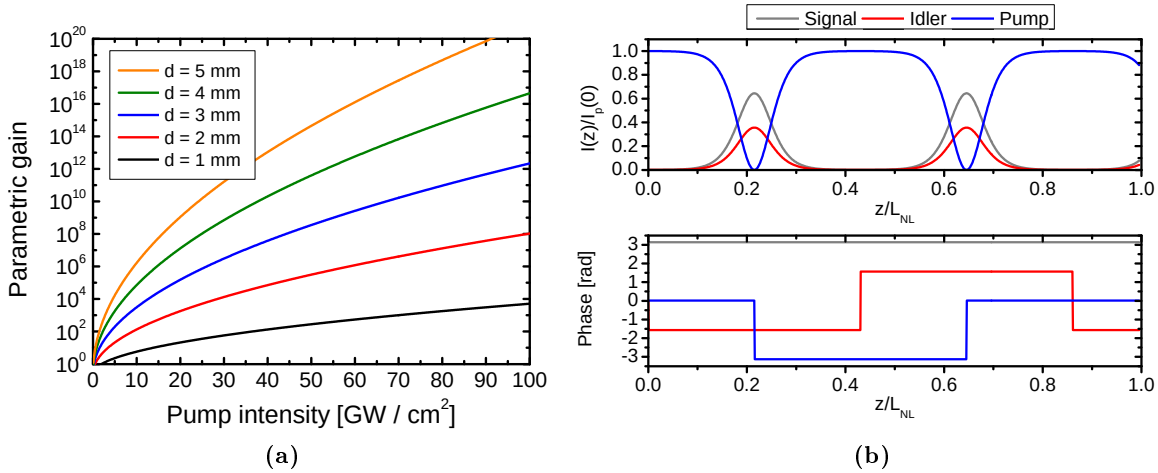

(a) (b)

Figure 3.2 – a) Calculated parametric gain versus pump intensity for various crystal lengths. (λ_p=515 nm, λ_s=800 nm, d_{eff}=2.1 pm/V, non-depleted pump approximation), b) Calculated evolution of the intensities (top) and phases (bottom) of signal idler and pump wave in an OPA with strong pump depletion and back-conversion (λ_p=515 nm, λ_s=800 nm, $I_s(0)/I_p(0) = 10^{-3}$).

On the other hand, the output energies of these high repetition rate OPOs are typically in the nJ range and the pulse duration is typically of the order of the pump pulses (50 to 100 fs) [38]. Nevertheless, sub-20 fs pulses have been generated in OPOs, albeit only with nanojoule pulse energies [39].

OPAs require higher pump energies and are therefore usually driven by amplified laser systems at lower repetition rates. But OPAs provide higher output energies, ultra-broadband amplification, which is only limited by the phase matching properties, and easier operation, since no stabilized cavity is needed [20]. In addition, energy scaling of an OPA is possible by increasing the beam diameters and the crystal apertures.

Phase in optical parametric amplifiers

The phase of the three interacting waves plays an important role in OPAs. The evolution of the phases, for the case of zero initial idler is found from the coupled wave equations [40]:

$$\phi_s(z) = \phi_s(0) - \frac{\Delta k z}{2} + \frac{\Delta k \gamma_s^2}{2} \int \frac{dz}{f + \gamma_s^2}, \tag{3.21}$$

$$\phi_i(z) = \phi_p(0) - \phi_s(0) - \frac{\Delta k z}{2} + \frac{\pi}{2}, \tag{3.22}$$

$$\phi_p(z) = \phi_p(0) - \frac{\Delta k}{2} \int \frac{f dz}{1 - f}, \tag{3.23}$$

where $f = 1 - I_p(z)/I_p(0)$ is the fractional depletion of the pump and $\gamma_s^2 = \omega_p I_s(0)/\omega_s I_p(0)$ is the input photon intensity ratio of signal and pump. From these expressions several important

statements can be extracted. First it is worth mentioning that the direction of energy flow in the OPA is governed by the OPA phase $\phi_{opa} = \phi_p - \phi_s - \phi_i$. Interestingly, the generated idler wave automatically takes a phase of $\phi_i = \phi_p(0) - \phi_s(0) + \frac{\pi}{2}$, maximizing the parametric gain which is achieved for $\phi_{opa} = -\frac{\pi}{2}$. Moreover, phase distortions of the pump wave are transferred to the idler wave , but the signal phase is independent of the initial pump phase. Consequently, it is possible to maintain the optical quality of a signal beam, even if a pump beam with spatial phase aberrations is applied. In addition, temporal phase distortions of the pump (e.g. a chirped pump pulse) do not affect the signal. Finally, in case of perfect phase matching ($\Delta k = 0$), there is no temporal evolution of the phase. Phase changes, resulting from parametric amplification, occur only if a phase mismatch is present.

Depleted pump and saturated OPA

If pump depletion is not negligible, the solutions of eqs. 3.13 ... 3.15 are given by Jacobi elliptic functions [36]. Alternatively, the solutions are found by solving the coupled wave equations numerically by standard approaches such as the Runge-Kutta method. As an example, the intensity and phase of signal (grey), idler (red) and pump wave (blue) are displayed in fig. 3.2b versus the propagation length z, which has been normalized to the characteristic nonlinear length $L_{NL} = 1/\Gamma$. Perfect phase matching has been assumed and the initial phase of the signal and the pump wave have been set to π and 0, respectively. It can be seen that the generated idler automatically takes a phase of $-\frac{\pi}{2}$ to ensure efficient parametric amplification of signal and idler ($\phi_{opa} = -\frac{\pi}{2}$). This results in full depletion of the pump wave at $z = 0.215 \cdot L_{NL}$. At this point the phase of the pump waves jumps to $-\pi$ and back-conversion starts due to the changed OPA phase $\phi_{opa} = \frac{\pi}{2}$. Interestingly, the fully back-converted idler wave can change its phase at $z = 0.43 \cdot L_{NL}$ and parametric amplification starts again ($\phi_{opa} = -\frac{\pi}{2}$).

The influence of phase mismatch

A phase mismatch of the interacting waves Δk is accumulated over the crystal length z and severely reduces the conversion efficiency of the nonlinear process. Neglecting pump depletion, the conversion efficiency η of optical parametric amplification is calculated as [36]

$$\eta = \eta_{max} \frac{\sin^2\left(\frac{\Delta k z}{2}\right)}{\left(\frac{\Delta k z}{2}\right)^2}, \tag{3.24}$$

where η_{max} is the maximum conversion efficiency which is obtained in the case of perfect phase matching[3]. The $\mathrm{sinc}^2\left(\frac{\Delta k z}{2}\right) = \sin^2\left(\frac{\Delta k z}{2}\right) / \left(\frac{\Delta k z}{2}\right)^2$ dependence of the accumulated wave vector mismatch describes the influence of the different phase velocities on the interacting waves. This function is plotted in fig. 3.3. The first minimum of this function is found at $|\Delta k| = \pi / z$

[3] The same dependence is also observed for second harmonic generation.

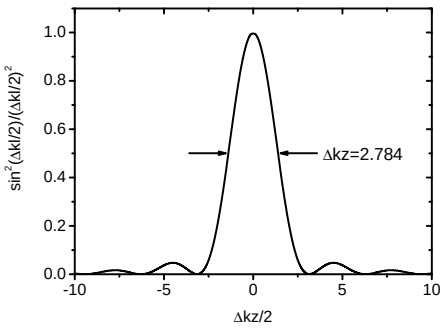

Figure 3.3 – Plot of the sinc function, which describes the effects of phase mismatch in the non-depleted pump approximation of nonlinear $\chi^{(2)}$ frequency conversion processes.

and the full width at half maximum is given by $\Delta kz = 2.784$. The corresponding length, up to which energy transfer in the desired direction occurs, is defined as the coherence length $l_c = \frac{\pi}{\Delta k}$. If the intensity of the amplified signal wave reaches a maximum, then ϕ_{OPA} changes its sign from negative to positive prior to full depletion of the pump and back conversion occurs for $l_c < z < 2l_c$. Hence, it is important to keep the phase mismatch low over the entire crystal length, which is the objective of phase matching.

3.3.4 Phase matching in birefringent crystals

Phase matching ($\Delta k = 0$), which means that the desired wave and the driving nonlinear polarization have the same phase velocity, can also be seen as a momentum conservation of parametric nonlinear processes. For homogeneous, isotropic and normally dispersive media the refractive index increases monotonically with the frequency, thus phase matching is impossible. In birefringent crystals the refractive index additionally depends on the polarization state. For uniaxial crystals the k-vector and the optical axis of the crystal span over a fundamental plane[4]. The so called ordinary wave is linearly polarized perpendicular to the fundamental plane, while the extraordinary wave is polarized parallel to it. The angle θ, measured between the k-vector and the optical axis, determines the refractive index of the extraordinary wave:

$$\frac{1}{n^e(\theta)^2} = \frac{\cos^2\theta}{[n^o]^2} + \frac{\sin^2\theta}{[n^e]^2}. \tag{3.25}$$

In negative uniaxial crystals, such as BBO, the refractive index of the extraordinary polarized wave is lower than the refractive index of the ordinary polarized wave ($n^e < n^o$). As a simple example, collinear phase matching (all wave vectors parallel) for SHG, can be achieved if

[4]Within a fundamental plane, a biaxial crystal can be seen as uniaxial and phase matching follows the same principles. More information on biaxial crystals and their phase matching properties can be found in [36].

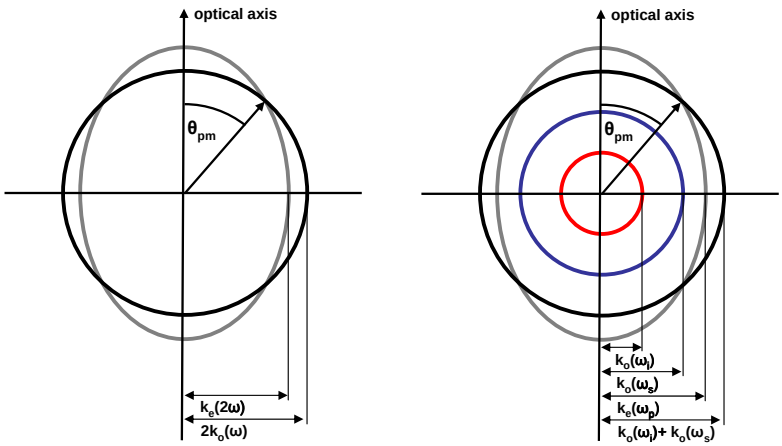

(a) SHG **(b)** OPA

Figure 3.4 – Illustration of Type I k-vector angular phase matching for a) SHG and b) OPA in a negative uniaxial crystal.

the second harmonic is extraordinary polarized, while the fundamental is ordinary polarized (Type I). In this case the phase matching angle θ_{pm} can be calculated by

$$\theta_{pm} = \arcsin\left[\frac{n^e(2\omega)}{n^o(\omega)}\sqrt{\frac{(n^o(2\omega))^2 - (n^o(\omega))^2}{(n^o(2\omega))^2 - (n^e(2\omega))^2}}\right] \tag{3.26}$$

and this kind of phase matching technique is named angular phase matching or critical phase matching, which will be applied throughout this thesis. The attribute "critical" is related to the fact that this technique is sensitive to the angular alignment of the crystal. This also implies limitations to the beam divergence, which will be discussed at the end of this chapter. In some special cases, phase matching can also be achieved along a principal axis of the nonlinear crystal by temperature tuning, named temperature phase matching or noncritical phase matching.

Type I angular phase matching of an OPA within a negative uniaxial crystal can be achieved if signal and idler wave are ordinary and the pump wave is extraordinary polarized. The corresponding phase matching angle is calculated by [20]

$$\theta_{pm} = \arcsin\left[\frac{n^e(\omega_p)}{n^e(\omega_p,\theta_{pm})}\sqrt{\frac{(n^o(\omega_p))^2 - (n^e(\omega_p,\theta_{pm}))^2}{(n^o(\omega_p))^2 - (n^e(\omega_p))^2}}\right]. \tag{3.27}$$

An illustration of the Type I k-vector phase matching for SHG and OPA is shown in fig. 3.4. Throughout this thesis only Type I phase matching is considered, as it normally offers the largest spectral bandwidth [20]. If either the signal or the idler has the same polarization as

the pump, one speaks of Type II phase matching, which shows a more pronounced wavelength dependence of the phase matching angle resulting in a generally smaller spectral bandwidth [20]. It is also worth mentioning that quasi phase matching has been achieved successfully e.g. in periodically poled lithium niobate (PPLN) and periodically poled lithium tantalate (PPLT) and these materials have been employed in OPCPA systems [41]. However, amplification of sub-10 fs has not been demonstrated yet in periodically poled nonlinear media [21] and therefore they are not the best choice for amplification of the shortest optical pulses. In addition, the limited aperture of the periodically poled crystals restrains the power and energy scalability of these optical amplifiers [22].

3.3.5 Real beams and ultra-short pulses

Phase matching bandwidths

Real beams are divergent and especially ultra-short pulses are not monochromatic. Additionally, for high power applications the temperature dependence of phase matching has to be considered as well. In a first order approximation, the variation of the phase mismatch around $\Delta k = 0$ with angle, temperature and frequency can be expressed by

$$\Delta k(\theta, \omega, T) \simeq \frac{\partial(\Delta k)}{\partial \theta}\Delta\theta + \frac{\partial(\Delta k)}{\partial T}\Delta T + \frac{\partial(\Delta k)}{\partial \omega}\Delta\omega. \tag{3.28}$$

The angular, temperature and spectral bandwidth ($\Delta\theta, \Delta T$ and $\Delta\omega$) are usually defined as

$$\Delta\theta = \frac{2\pi}{l}\left(\frac{\partial(\Delta k)}{\partial \theta}\right)^{-1}, \Delta T = \frac{2\pi}{l}\left(\frac{\partial(\Delta k)}{\partial T}\right)^{-1}, \Delta\omega = \frac{2\pi}{l}\left(\frac{\partial(\Delta k)}{\partial \omega}\right)^{-1}. \tag{3.29}$$

These bandwidths scale inversely with the crystal length l and therefore the bandwidth-length product is a characteristic constant for each specific crystal, nonlinear process and phase matching condition. This has to be taken into account for the design of a frequency converter, such as SHG or OPA. Please note that throughout this thesis only the angular bandwidth in the critical plane, which is most sensitive to angular detuning, is considered. The influence of limited phase matching bandwidths will be discussed in the next sections.

Beam divergence and focusing

Typically, the intensity of optical beams decreases outside the focus. To include this effect for Gaussian beams, Boyd and Kleinmann [42] defined an effective focus length as

$$l_f = \pi z_R. \tag{3.30}$$

The Rayleigh range z_R, for Gaussian like beams, is defined as

$$z_R = \frac{\pi w_0^2}{\lambda M^2}, \tag{3.31}$$

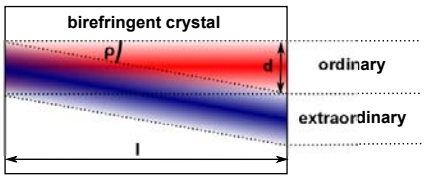

Figure 3.5 – Illustration of the walk-off effect between ordinary and extraordinary beams in birefringent crystals

with the beam quality factor M^2 and the beam waist radius w_0 ($1/e^2$ half width of the intensity profile).

Furthermore, for focused beams the angular bandwidth $\Delta\theta$ of the nonlinear interaction limits the useful crystal length for a given beam waist radius. The absolute angular acceptance of the nonlinear process is defined as $\Delta\theta^\star{=}\Delta\theta{\cdot}l$. For a Gaussian beam, the far field half divergence angle Θ is given by

$$\Theta = \frac{\lambda M^2}{\pi w_0}. \tag{3.32}$$

Consequently, the coherence length can be rewritten as

$$l_c = \frac{\Delta\theta^\star}{2\Theta} = \frac{\Delta\theta^\star \pi w_0}{2\lambda M^2}. \tag{3.33}$$

It can be seen as an upper limit for the useful interaction length and e.g. limit the gain of an optical parametric amplifier, which will be discussed in sec. 4.1.

Birefringence and walk-off

In birefringent media the direction of energy flow (Poynting vector) of an extraordinary wave is generally not the same as the propagation direction of the optical wave (wave vector). The extraordinary wave is seen to "walk off" from the ordinary beam as illustrated in fig. 3.5. Thus, beams of finite size will not necessarily overlap over the entire crystal length. In practice, for moderate peak power laser pulses, which have to be focused tightly into the nonlinear crystal, the walk-off effect can be a severe limit for the usable crystal length. For Gaussian beams with the beam radius w_0, the characteristic walk-off length can be written as [42]

$$l_a = \frac{\sqrt{\pi} w_0}{\rho}, \tag{3.34}$$

where ρ is the walk-off angle which depends on the specific crystal and the propagation direction.

Spectral bandwidth of the nonlinear process

Up to this point monochromatic waves have been assumed. However, ultra-short laser pulses are composed of a broad frequency spectrum. Therefore, the spectral bandwidth of the

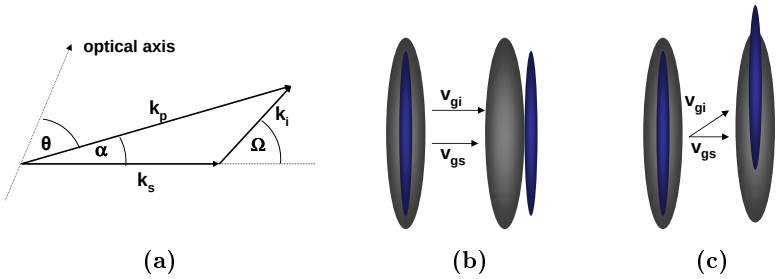

Figure 3.6 – a) Schematic of noncollinear phase matching of signal, pump and idler. k_s, k_i and k_p represent the wave vectors of signal, idler and pump respectively, b) Illustration of signal and idler group velocity mismatch in non-degenerate collinear case, c) Illustration of signal and idler group velocity matching, achieved in noncollinear geometry (grey: signal, blue: idler).

nonlinear process has to be considered, when working with ultra-short pulses. For efficient conversion of a laser pulse the spectral bandwidth defines the meaningful crystal length according to eq. 3.29.

For ultra-short pulse amplification it is necessary to obtain phase matching over a large spectral range. Around the phase matched central angular frequency ω_0 the phase mismatch can be expressed in a Taylor series as

$$\begin{aligned} \Delta k(\omega_0 + \Delta\omega) &= k_p - k_s - k_i - \left(\frac{\partial k_s}{\partial \omega} \Big|_{\omega_{s,0}} - \frac{\partial k_i}{\partial \omega} \Big|_{\omega_{i,0}} \right) \Delta\omega \\ &\quad - \frac{1}{2} \left(\frac{\partial^2 k_s}{\partial \omega^2} \Big|_{\omega_{s,0}} - \frac{\partial k_i^2}{\partial \omega^2} \Big|_{\omega_{i,0}} \right) (\Delta\omega)^2 + O\left[(\Delta\omega)^3 \right], \end{aligned} \tag{3.35}$$

if a quasi monochromatic pump and well collimated beams are assumed. For broadband phase matching $\Delta k(\omega_0)$ and its derivatives should be equal to zero. In the degenerate case, where $\omega_i = \omega_s$, the first derivatives, which represent the inverse group velocities of signal and pump, cancel out each other ($\partial\omega_s = -\partial\omega_i$ is given by energy conservation, assuming a monochromatic pump) and achromatic phase matching is achieved.

In the non-degenerate case $\omega_i \neq \omega_s$, the group velocities can be matched by a noncollinear geometry. Here, the same conditions can be applied to the component parallel and normal to the signal wave vector [43]:

$$\Delta k_{\parallel} = k_p \cos\alpha - k_s - k_i \cos\Omega, \tag{3.36}$$

$$\Delta k_{\perp} = k_p \sin\alpha - \sin\Omega, \tag{3.37}$$

where α is the angle between the pump an signal wave vector, and Ω is the angle between idler and signal wave vector, as illustrated in fig. 3.6a. When both equations 3.36 and 3.37 are differentiated with respect to ω_s and set to zero, a condition for broadband phase matching is found:

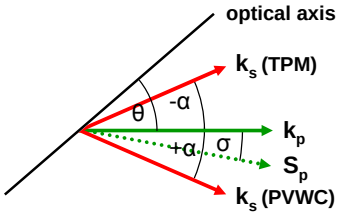

Figure 3.7 – Schematic of tangential phase matching (TPM) and Poynting vector walk-off compensating (PVWC) geometry for Type I phase matching in a negative uniaxial crystal. The Poynting vector of the pump wave $\mathbf{S}_p$ is shown for illustration purposes only, and is not true in scale.

$$\frac{\partial k_s}{\partial \omega}\,|_{\omega_0}\,\cos\Omega = \frac{\partial k_i}{\partial \omega}\,|_{\omega_0}\;\; v_{gs} = v_{gi}\cos\Omega. \tag{3.38}$$

For practical reasons the noncollinear angle α is typically used to characterize the geometry, which can be calculated according to [43]

$$\sin\alpha = \frac{k_i \sin(\pi - \Omega)}{\sqrt{k_s^2 + k_i^2 + 2k_s k_i \cos\Omega}}. \tag{3.39}$$

Both operation at degeneracy and noncollinear phase matching allow for a very large phase matched spectral bandwidth, as they zero the first order variation of Δk with ω. In order to achieve the largest possible gain bandwidth, higher order variations have to be considered as well. Optimization of the geometry, with the goal of either the shortest pulse duration or the highest pulse peak power at the output of an OPCPA system, will be the topic of sec. 4.2 of this thesis.

Note that for a given noncollinear angle the direction of the signal can be chosen in two directions within the fundamental plane as illustrated in fig. 3.7. Typically, the Poynting-vector walk-off compensation scheme (PVWC-scheme) is used to compensate the transverse walk-off, at least partly [44]. In this case, the signal wave propagates at an angle of $\theta + \alpha$ relative to the optical axis. The second possibility is tangential phase matching (TPM, see fig. 3.7). Here, the signal wave propagates between the optical axis and the pump beam vector at an angle $\theta - \alpha$ with respect to the optical axis, resulting in a larger angle between signal and pump wave pointing vector. A detailed investigation on the resulting limitations for the gain of a noncollinear OPA in both PVWC and TPM configuration will be topic of sec. 4.1 of this thesis.

Influence of group velocity and dispersion

The interacting ultra-short pulses usually travel with different group velocities within the crystal. Therefore, they will lose their temporal overlap after a certain propagation distance. Generally, the group velocities have to be considered in the coupled wave equations [20].

However, the group velocities can be neglected for pulses significantly longer than the group delay in the nonlinear crystal. Although laser pulses shorter than 10 fs have been generated within this work, the pulses were chirped to several hundreds of femtoseconds prior amplification in the nonlinear crystal. The pump pulse duration is usually chosen to be even longer to allow for uniform amplification of the whole signal pulse. Therefore, it is acceptable to neglect the group velocity effects in the nonlinear crystal, which is typically only a few millimeters long[5]. In addition, broadband OPAs already provide matched group velocities of signal and idler, as this has turned out as a requirement for broadband phase matching in the previous subsection.

As already shown in sec. 3.2, the presence of dispersion has a strong influence on the shape of ultra-short pulses. However, as we use stretched signal pulses and relatively narrow-band pump pulses ($L_D \gg l$), dispersion effects can be neglected for OPA modeling throughout this thesis.

Summary

At the beginning of this chapter the fundamental description of light as electromagnetic waves has been introduced. Then, ultra-short pulses and the influence of dispersion on their propagation have been discussed. The basic theory of SHG and OPA has been presented, assuming monochromatic plane waves. The importance of phase matching has been pointed out and phase matching techniques have been introduced. Finally, the special properties of the nonlinear process with respect to real optical beams and ultra-short laser pulses have been discussed. The angular bandwidth of the nonlinear process and transverse walk-off may limit the performance of an OPA severely. The spectral bandwidth of the OPA is found to be related to the group velocity mismatch of signal and idler. Either working at degeneracy or a noncollinear geometry are found to be convenient to significantly enhance the spectral bandwidth of and OPA. The next chapter of this thesis will include investigations on the gain limitations as well as the optimization of the spectral bandwidth of OPAs.

[5] The group delay of signal and pump in a collinear OPA is 93 fs/mm (BBO, λ_S=1030 nm, λ_P=515 nm and $\theta = 23.4°$) and 63 fs/mm (BBO,λ_S=800 nm, λ_P=515 nm and $\theta = 22.7°$).

4 Theoretical aspects of OPCPA development

This chapter deals with the main theoretical aspects of high repetition rate, high power OPCPA development. At first, different borate crystals are evaluated as potential nonlinear material. Their gain properties are compared for different geometries. The gain limiting effects are pointed out and requirements on the pump laser are given.

The second part of this chapter covers the optimization of the gain bandwidth of an OPCPA. At first, the influence of the applied pump pulse duration is discussed. Then, collinear OPCPA at degeneracy and OPCPA in noncollinear geometry are optimized in order to achieve the shortest and most intense pulses. As it turns out that different configurations are needed to achieve either the shortest pulses or the highest pulse peak power.

Gain narrowing and saturation effects which occur for non-uniform temporal and spatial profiles are the subject of the third part of this chapter. In addition, consequences for the design of efficient parametric amplifiers are presented.

Finally, parasitic nonlinear processes, such as SHG of signal or idler wave are discussed. These effects are particularly problematic for parametric amplification of ultra-broad spectra but can be avoided by choosing a proper interaction geometry.

4.1 Choice of nonlinear material

The nonlinear crystal has to fulfill a manifold of requirements. First of all, for ultra-short pulse amplification it is supposed to support broadband phase-matching. This is achieved either at degeneracy or in a noncollinear configuration as discussed in the previous chapter. The crystals transparency range should cover pump, signal and idler wavelengths. Most important, a high nonlinear coefficient and a high damage threshold are required, which allows for the use of short crystal lengths. Several crystals belonging to the borate group (BBO, LBO, BiBO) meet these requirements. Their main characteristics for broadband amplification at 800 nm central wavelength are shown in tab. 4.1.

Generally, OPAs are known for their high single pass gain, which results in simple single pass amplifier designs. However, when using moderate peak power pump lasers the single pass gain can be severely limited. As introduced in sec. 3.3.5 three characteristic lengths can be defined which limit the useful crystal length, namely the effective focus length l_f (eq. 3.30), the coherence length for focused optical beams l_c (eq. 3.33) and the walk-off length

Crystal material	BBO (beta barium borate)	LBO (lithium triborate)	BiBO (bismuth borate)
Chemical formula	β-BaB_2O_4	LiB_3O_5	BiB_3O_6
Nonlinear coefficient d_{eff}	2.08 pm/V	0.82 pm/V	2.95 pm/V
Nonlinear parameter γ	1.52 10^{-4} $W^{-0.5}$	0.65 10^{-4} $W^{-0.5}$	1.97 10^{-4} $W^{-0.5}$
Angular bandwidth (pump) $\Delta\theta^{\star}$	0.86 mrad·cm	6.86 mrad·cm	1.81 mrad·cm
Damage threshold (532 nm)	$\sim$7 GW/cm^2 (250 ps)	$>$ 10 GW/cm^2 (100 ps)	$\sim$4 GW/cm^2 (200 ps)
Transparency range	189 – 3500 nm	160 - 2600 nm	286 – 2500 nm
Crystal plane (n_x<n_y<n_z)	XZ	XY	YZ
Phase-matching angle θ	24.6 °	16.6 °	162.6 °
Noncollinear angle α	2.6 °	1.6 °	3.9 °
Walk-off angle ρ	3.2 °	0.4°	1.4 °

Table 4.1 – Properties of the nonlinear crystals BBO, LBO and BiBO for broadband type I interaction 800 nm + 1446 nm = 515 nm. The data are taken from manufacturer data sheets (Ekspla, Crystech) and from the freely available software SNLO [45].

l_a (eq. 3.34). As a figure of merit (FOM) the corresponding gain for perfect phase matching ($\Delta k = 0$) can be calculated for each crystal and geometry, according to eq. 3.17, where the minimum of the three characteristic lengths is assumed as crystal length l:

$$FOM = 1 + \sinh^2\left(\sqrt{I_p}\gamma l\right),\ l = \min\begin{cases} l_f = \frac{\pi^2 w_0^2}{\lambda M^2} \\ l_c = \frac{\Delta\theta^{\star}\pi w_0}{2\lambda M^2} \\ l_a = \frac{\sqrt{\pi} w_0}{\rho} \end{cases}. \tag{4.1}$$

Equation 4.1 is valid for Gaussian-like beams, with the beam quality factor M^2. The intensity I_p in the focus can be calculated as

$$I_p = \frac{2P_p}{\pi w_0^2}, \tag{4.2}$$

where P_p is the pulse peak power. Hence, eq. 4.1 can be rewritten as:

$$FOM = 1 + \min \begin{cases} \sinh^2\left(\gamma\sqrt{2\pi P_p}\frac{\pi w_0}{\lambda M^2}\right), & l = l_f \,(\text{eff. focus length}) \\ \sinh^2\left(\gamma\sqrt{\frac{1}{2}\pi P_p}\frac{\Delta\theta^\star}{\lambda M^2}\right), & l = l_c \,(\text{angular acceptance}) \\ \sinh^2\left(\gamma\sqrt{2P_p}\frac{1}{\rho}\right), & l = l_a \,(\text{walk-off}) \end{cases} . \tag{4.3}$$

Interestingly, for coherence length and aperture length the beam waist radius w_0 cancels out in eq. 4.3. Focusing to a smaller beam waist leads to a higher intensity which enhances the nonlinear interaction. However, as a consequence of limited angular acceptance or walk-off the crystal length has to be reduced, leading to a gain limitation within one crystal pass. In contrast, the product of effective focal length and square root of pump intensity scales with w_0, meaning that looser focusing and longer crystals would lead to a higher gain limit. However, in this thesis the effective focal length plays only a minor role, as it is not the limiting factor in all cases theoretically considered and experimentally observed[1]. Consequently, for further considerations, the effective focal length is neglected. In order to compare the properties of BBO, LBO and BiBO the small signal gain limits arising form angular acceptance and walk-off are calculated for both Poynting vector walk-off compensating scheme (PVWC) and Tangential phase matching scheme (TPM). The results are presented in fig. 4.1.

[1] Throughout this thesis, critical phase matching is utilized. However, for noncritical phase matching the effective focal length can be the limiting factor, as no walk-off is present and the angular bandwidth may be significantly enhanced.

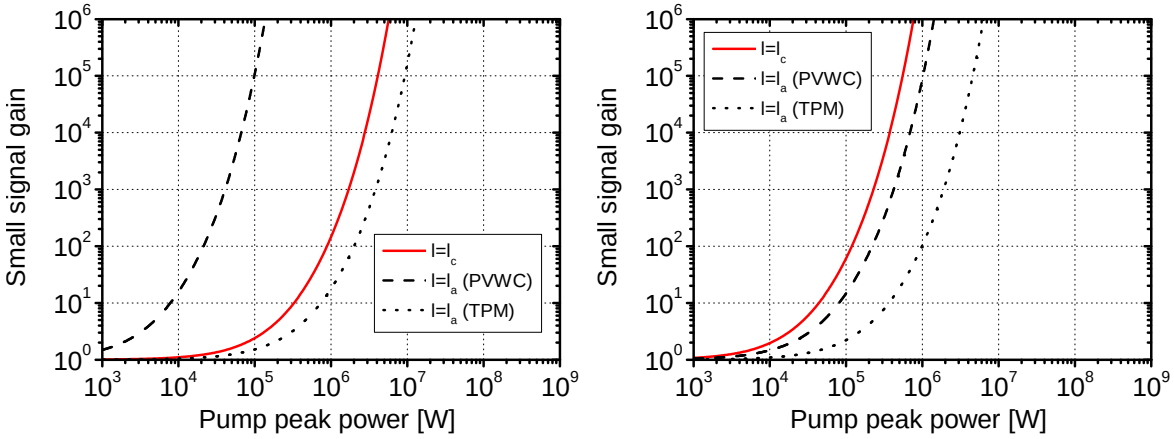

(a) BBO, M^2=1.0 **(b)** LBO, M^2=1.0

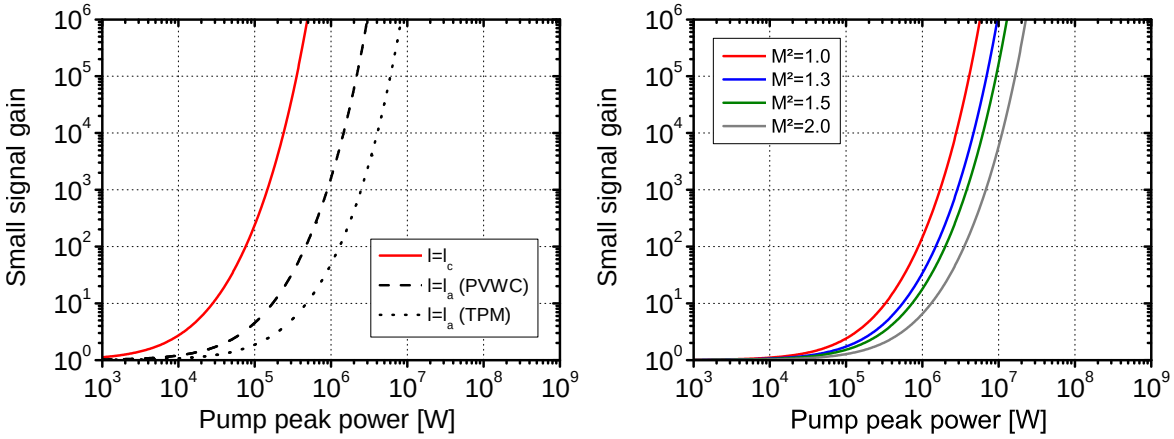

(c) BiBO, M^2=1.0 **(d)** BBO, $M^2 \geqq 1.0$

Figure 4.1 – Calculated small signal limits versus pump peak power for a) BBO, b) LBO and c) BiBO, red curve: gain limit due to angular acceptance ($l = l_c$), black curves: gain limit due walk-off ($l = l_a$), dotted curve: TPM, dashed curve: PVWC. d) Small signal gain limit for BBO in PVWC geometry, limited due to ($l = l_c$), for various beam quality factors (Broadband noncollinear type I interaction 800 nm + 1446 nm = 515 nm).

It is worth mentioning that the angular acceptance of the pump is the smallest of all interacting beams and it is therefore considered for the calculations. A few fundamental statements can be extracted from fig. 4.1. It can be seen that the highest gain can be achieved in PVWC geometry (black dashed curves), where walk-off and noncollinear angle partly cancel out. However, in case of BBO the gain is limited by the relatively low angular acceptance (red curve). In order to achieve significant small signal gain ($\sim 10^3$), a pump pulse peak power of ($\sim$2 MW, $\sim$1 MW, $\sim$0.4 MW) is required for BBO, LBO and BiBO crystals, respectively. In TPM configuration, the gain is limited for all crystals by the transverse separation of pump and signal, since walk-off angle and noncollinear angle add in this case. In this case, a useful small signal gain ($>10^3$) can only be achieved if the pump pulse peak power is higher

than ∼5 MW. The influence of pump beam quality is shown in fig. 4.1d, for BBO in PVWC configuration and pumped with a Gaussian like beam of various beam quality factors. In this case, the gain is limited by the angular acceptance. In addition, the gain is significantly reduced for larger M^2 values, as the focal spot diameter of Gaussian like beams increases linearly with the beam quality factor M^2. Consequently, a good beam quality is desired, especially when working with moderate peak power pump lasers.

4.2 Gain bandwidth optimization

As already mentioned in 3, it is necessary to keep the wave-vector mismatch small over the whole spectral range of the signal to enable ultra-broadband amplification. Two configurations were found which cancel the first order variation of Δk with the frequency, the degenerate OPA and a noncollinear configuration. Simulations of the parametric gain, based on the calculated wave-vector mismatch over the spectral range of an ultra-broadband signal, are performed to further optimize the noncollinear configuration.

The calculations presented in this chapter generally rely on several assumptions. Firstly, all interacting waves are assumed as plane waves, which is also valid for well-collimated beams. In addition, the description is a quasi-cw approximation, neglecting dispersion and group velocity effects, which is reasonable for chirped pulses and short crystal lengths (see sec. 3.3.5). The signal and pump angles are fixed, while the idler angle is chosen to close the k-vector triangle as illustrated in fig. 3.6a. Transverse walk-off of the interacting beams is neglected as well. Finally, the wave vector mismatch perpendicular to the signal wave vector is small and therefore neglected within the calculations. More details on the calculation methods as well as discussions of the validity of the approximations can be found in [43]. The calculations and optimizations have been performed for BBO, as it will be used in the experiments later. Since LBO and BiBO have very similar phase matching properties [46, 47], the main statements of this chapter are valid for these crystals, too. Of course, broadband amplification in these crystal is observed at different phase matching and noncollinear angles. In addition, the exact shape of the gain spectrum is different and would require further calculations, which are beyond the scope of this work.

4.2.1 Pump pulse duration - crystal length

In general, shorter nonlinear crystals can be used to decrease the accumulated phase mismatch caused by wave vector mismatch. In order to achieve sufficient gain, the pump intensity has to be increased accordingly. However, this is ultimately limited by the damage threshold of the nonlinear crystal. In this context it is important to know that the damage intensity threshold of transparent optical media, in a rough assumption, scales inversely with the square-root of the pulse duration [48]. For pulses shorter than 20 ps, the electrons have insufficient time to couple to the lattice during the laser pulse. The damage threshold continues to decrease

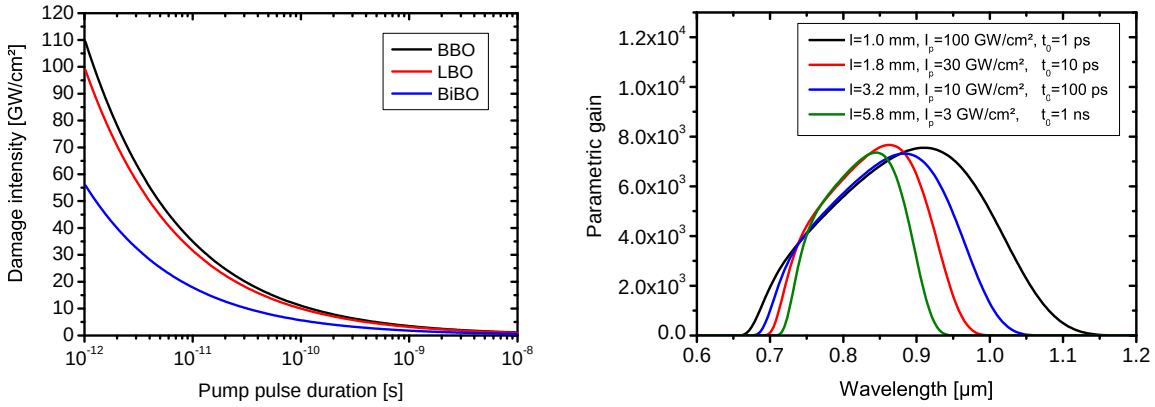

(a) **(b)**

Figure 4.2 – a) Damage threshold of BBO, LBO and BiBO versus pump pulse duration. b) Small signal parametric gain spectrum for different crystal lengths. The calculation assumes a wide rectangular input spectrum and uses BBO in a noncollinear geometry with the following parameters: θ=24.2°, α=2.6°, λ_p=515 nm, d_{eff}=2.1 pm/V.

with decreasing pulse width, but at a rate slower than $t^{0.5}$ in the range 0.1–20 ps [48].

Using the damage threshold data given in tab. 4.1, the damage threshold is calculated and plotted versus the pump pulse duration for BBO, LBO and BiBO in fig. 4.2a, applying the simple square root scaling law. In consequence, the displayed damage thresholds are slightly too low for pulses shorter than 20 ps.

As a result of the pulse duration dependent damage threshold, shorter pump pulses can be focused to higher intensities and therefore enable the use of shorter crystal lengths. Due to reduced phase accumulated mismatch $\Delta k \cdot l$ in the spectral wings, the spectral bandwidth of the OPA is increased. To illustrate this effect, the parametric gain spectrum is plotted for different BBO crystal lengths in fig. 4.2b. Note that the pump intensity is adjusted to achieve the same maximum parametric gain for each crystal length. It can be seen that the amplified spectral bandwidth (FWHM) is increased by nearly a factor of two when using 1 ps pump pulses (black curve), which allow for 100 GW/cm² pump intensity, compared to 1 ns pulses which only permit 3 GW/cm² (green curve). As a consequence, ultra-broadband amplification, which is in needed for sub-10 fs pulses, requires preferably sub-nanosecond pump lasers. Typically, pump pulse are few-ten to a few hundred picoseconds long pump pulses in sub-10 fs OPCPA systems [49, 50, 51]. The use of sub-ps pump pulses allows for even higher intensities and consequently shorter nonlinear crystals. Such short pump pulses are in particular interesting for amplification of few-cycle laser pulses in an optimized noncollinear geometry, which will be presented in section 4.2.3 of this chapter.

4.2.2 Degenerate OPA

As already mentioned, a degenerate OPA implies that the signal and the idler wavelengths are equal. This intrinsically zeroes the group velocity mismatch, making it suitable for broadband parametric amplification. Moreover, this alternative allows the use of a single oscillator for simultaneous seeding of the parametric amplifier and the pump laser. As an example, the parametric amplifier is then driven by the second harmonic of the pump laser and a broadband signal is generated via additional spectral broadening e.g. in optical fibers.

In order to investigate the spectral gain characteristics of an OPA around the point of degeneracy, simulations are performed. Type I collinear phase matching in a 2 mm long BBO is applied using a pump wavelength of 515 nm. The pump intensity is set to 50 GW/cm², while the flat-top signal spectrum is set to 100 kW/cm². The resulting amplified signal spectrum is first calculated within the non-depleted pump approximation. Additionally, a numerical solution of the coupled wave equations (eqs. 3.13, 3.14 and 3.15), including pump depletion, is calculated. The results are plotted in fig. 4.3 for various phase matching angles together with the wave vector mismatch. It is worth mentioning that the spectral phase which is imposed by the OPA is small and can be almost completely compensated by second and third order dispersion of the pulse compressor [40, 52]. Perfect phase matching at the signal central wavelength, which is assumed at the degeneracy point λ_s=1030 nm, is achieved at θ=23.33°. As a result, the phase mismatch is zero at 1030 nm and its absolute value increases both for shorter and longer wavelengths, which reduces the parametric gain at these wavelengths. Nevertheless, in the undepleted pump approximation (grey curve, fig. 4.3a) an amplification bandwidth as large as 280 nm (FWHM) is achieved, which supports pulses as short as 9.3 fs if a flat spectral phase is assumed. If pump depletion and the resulting gain saturation effects are included, the amplification drops in the perfect phase matched center and remains unchanged in the weakly amplified spectral wings. This results in an effectively larger bandwidth of the amplified signal. Consequently, gain saturation can be helpful to further increase the gain bandwidth. At this point it is worth mentioning that within the simulation each spectral component depletes the pump pulse independently, which is a reasonable model for a flat-top, narrow-band nanosecond or picosecond pulse. For femtosecond pump pulses, the results are only an approximation, since group-velocity and dispersion effects are not considered within the calculations. As already discussed in sec. 3.3.5, these effects can be neglected as long as the pump pulse duration exceeds a few hundred femtoseconds and the crystal length is only a few millimeters.

Figures 4.3 b), c) and d) show the results for stepwise decreased phase matching angles. As a result, the vicinity of the degeneracy point undergoes positive wave-vector mismatch, which reduces the gain in the center of the signal spectrum. At the same time the spectral wings are better phase matched. Especially around the two zero phase mismatch points the parametric gain is significantly increased. The resulting amplification bandwidth increases with angular detuning of the nonlinear crystal, although splitting of the two sub-spectra (fig. 4.3d) leads

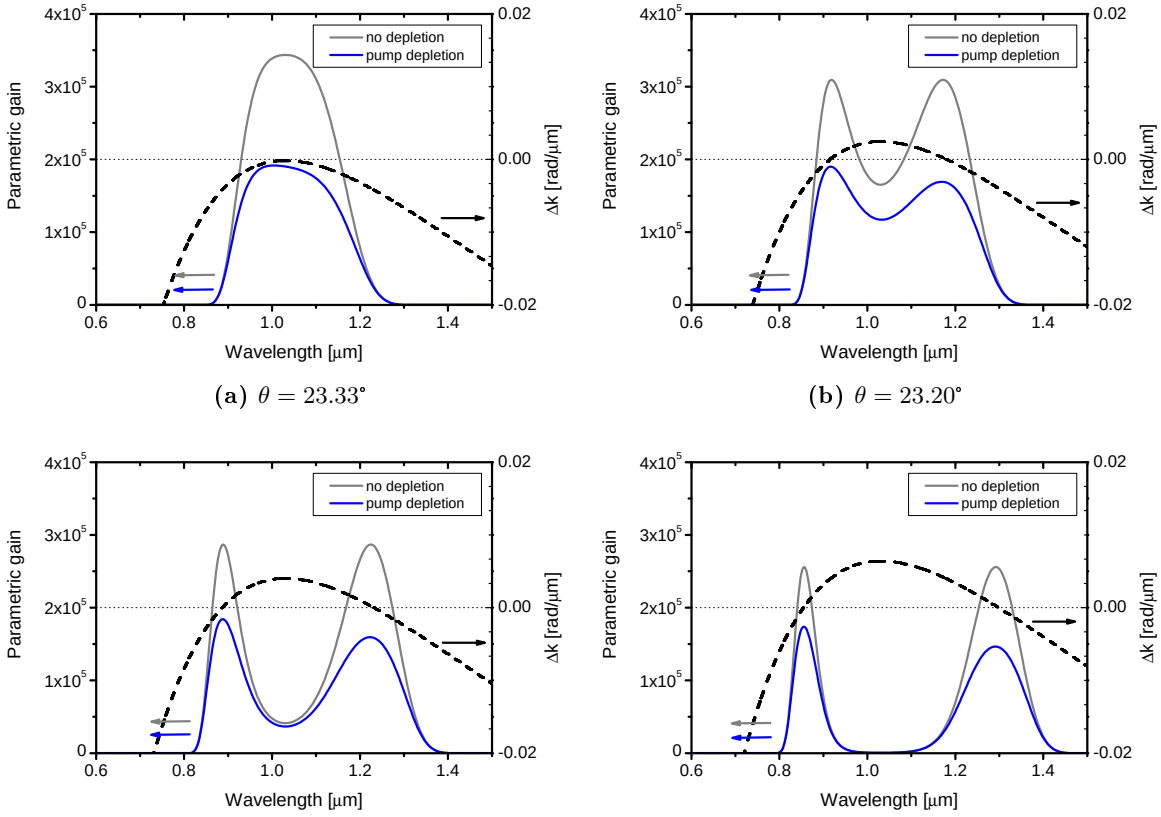

(a) $\theta = 23.33°$ **(b)** $\theta = 23.20°$

(c) $\theta = 23.12°$ **(d)** $\theta = 23.00°$

Figure 4.3 – Calculated spectral distribution of the parametric gain for various phase matching angles of a collinear OPCPA near degeneracy (BBO, λ_p=515 nm, d_{eff}=2.01 pm/V, I_p=50 GW/cm^2, I_s=100 kW/cm^2, l=2 mm).

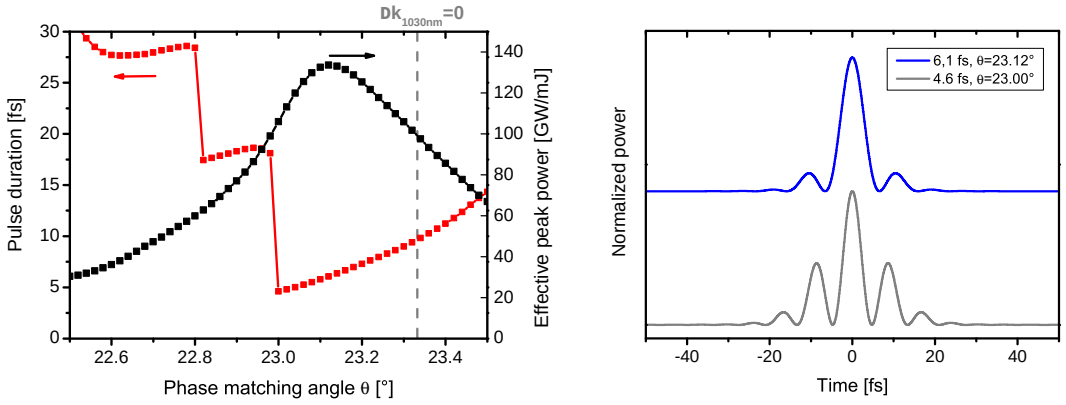

(a) (b)

Figure 4.4 – a) Pulse duration (FWMH) (red squares) and effective pulse peak power (black squares) versus phase matching angle (lines for eye guidance only). The gray dashed line represents the angle of perfect phase matching at 1030 nm. b) Corresponding temporal envelope of the Fourier limited pulses for θ=23.00°(grey) and θ=23.12° (blue), revealing the shortest pulse duration and the highest pulse peak power (BBO, λ_p=515 nm, d_{eff}=2.01 pm/V, I_p=50 GW/cm^2, I_s=100 kW/cm^2, l=2 mm).

to sub-pulses in the temporal domain, which is typically undesired and decreases the pulse peak power. In experimental applications a compromise has to be found. Optimization of the phase matching angle can be done with respect to the spectral bandwidth, the minimum pulse duration (via Fourier transform, assuming a flat-spectral phase) or the effective pulse peak power, depending on the requirements of the application. The latter quantity is most relevant to achieve high laser intensities. It is calculated as a figure of merit and specifies the peak power per pulse energy, assuming a flat spectral phase (Fourier limited case). With regards to the experiments, GW/mJ is chosen as a meaningful unit. The spectral bandwidth, the pulse duration and the effective pulse peak power are plotted in fig. 4.4a versus the phase matching angle. The steps in the pulse duration curve are caused by the FWHM measure and the multipeak nature of the output pulses. Please note that the grey line represents the angle of perfect phase matching at 1030 nm. In this case, a pulse duration of 9.6 fs and an effective peak power of 100 GW/mJ are observed. It can be seen that the shortest pulses, with only 4.6 fs duration (less than 1.5 optical cycles), are achieved at θ=23.00°, while the highest relative peak power is obtained at θ=23.12°, revealing a pulse duration of 6.1 fs. For both cases, the pulse envelopes of the temporal intensity profiles are plotted in fig. 4.4b.

4.2.3 Optimization of noncollinear phase matching

Noncollinear phase matching offers the possibility of group velocity matching even far from degeneracy. The noncollinear angle between signal and pump wave-vector offers superior phase matching properties due to the additional degree of freedom. Furthermore, using

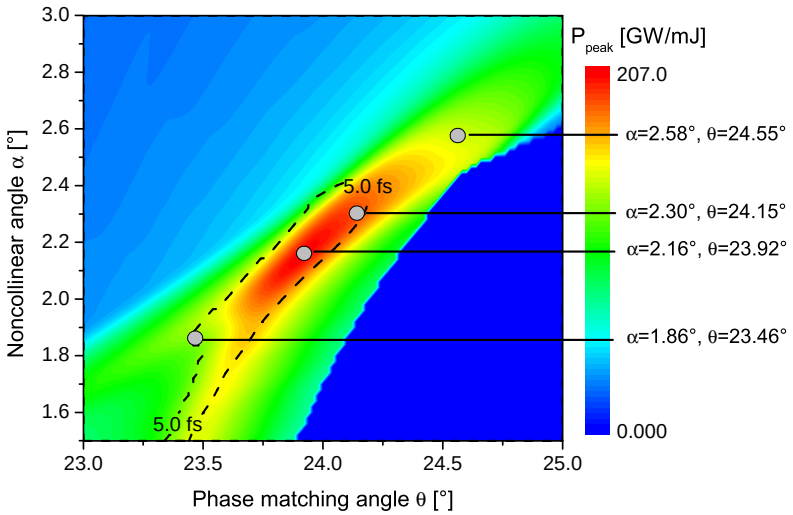

Figure 4.5 – Effective pulse peak power versus phase matching angle θ and noncollinear angle α. The black dashed line encloses the region with sub-5 fs pulse duration (BBO, λ_p=515 nm, d_{eff}=2.08 pm/V, I_p=50 GW/cm^2, I_s=100 kW/cm^2, l=2 mm).

515 nm pump wavelength, ultra-broadband phase matching can be achieved around 800 nm central wavelength, which fits well to Ti:Sa oscillators. A combination of ultra-broadband Ti:Sa oscillators and ultra-broadband noncollinear OPCPA is therefore ideal to generate the shortest and most intense laser pulses. To exploit the full potential of the noncollinear arrangement, its geometry has to be optimized by varying both the phase matching angle θ and the noncollinear angle α. Again, the effective peak power of the amplified pulses is taken as a measure to find the optimum geometry. The results of this two-dimensional analysis are presented in fig. 4.5. The effective peak power has been set to zero when a significantly reduced peak gain (a tenth of the value for $\Delta k = 0$) is observed. In these cases a large phase mismatch is present over the whole spectral range, reducing the parametric gain, which is not desired in practice.

The shortest pulse duration of only 2.9 fs (FWHM) is achieved at $\alpha = 1.86°$ and $\theta = 23.46°$. The corresponding spectrum is shown in fig. 4.6a, while the temporal pulse shape is shown in fig. 4.7 (grey curve). Certainly, the gap in the center of the spectrum results in several pre- and post-pulses which lower the pulse peak power (130 GW/mJ). The optimization reveals the highest pulse peak power (207 GW/mJ) for $\alpha = 2.16°$ and $\theta = 23.92°$. The spectral profile (fig. 4.6b) is flatter due to a reduced phase mismatch in the center. Consequently, the shape of the resulting 4.1 fs pulse (fig. 4.7, blue curve) is cleaner, with a reduced amount of energy in satellite pulses. The amplified spectral bandwidth ranges from 650 nm to 1200 nm. Achieving such a broad spectrum, covering nearly one optical octave, is challenging especially if it has to be recompressed to nearly transform limited pulses later. Methods for spectral broadening, such as white light generation in bulk media or SPM in fibers exist. A more straight forward approach is to use an ultra-broadband Ti:Sa oscillator to seed the OPCPA. Their spectral

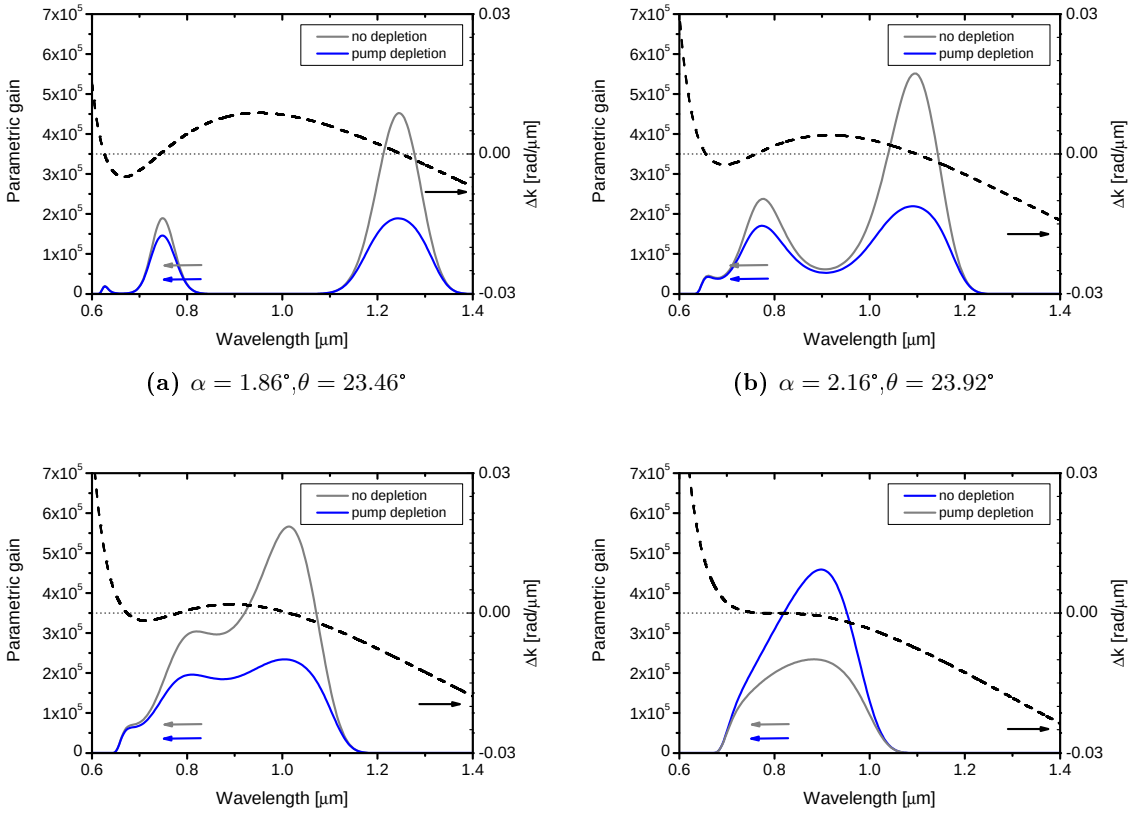

(a) $\alpha = 1.86°, \theta = 23.46°$ **(b)** $\alpha = 2.16°, \theta = 23.92°$

(c) $\alpha = 2.30°, \theta = 24.15°$ **(d)** $\alpha = 2.58°, \theta = 24.55°$

Figure 4.6 – Calculated spectral distribution of the parametric gain for various phase matching an noncollinear angles (BBO, λ_p=515 nm, d_{eff}=2.08 pm/V, I_p=50 GW/cm^2, I_s=100 kW/cm^2, l=2 mm).

bandwidth is typically around 300 nm (-10 dB), and the emitted spectrum typically does not reach far beyond 1000 nm. In this case, a gain spectrum as shown in fig. 4.6c is most suitable. Interestingly, three zero wave-vector mismatch points are present and therefore the phase mismatch is kept very low over a large spectral range, resulting in a smooth shape of the amplified spectrum, which reveals very clean pulses as short as 4.9 fs (red curve, fig. 4.7). The corresponding geometrical angles are $\alpha = 2.3°$and $\theta = 24.15°$ and the effective peak power of 189 GW/mJ is only 8.7 % lower than the maximum value. Hence, this configuration is applied in most of the experiments presented in this thesis. If the noncollinear angle is increased to $\alpha = 2.58°$ and the phase matching angle is set to $\theta = 24.55°$, both the wave-vector mismatch Δk and its first derivative are zero (fig. 4.6d). The angle α is often called the "magic" angle, as it provides phase and group velocity matching simultaneously. The angle can be found easily with eq. 3.38 and supports 6.5 fs pulse duration (4.7, green curve), whereas the effective peak power is only 146 GW/mJ.

In summary, the two dimensional optimization has identified the noncollinear configuration of a BBO OPCPA which is needed to achieve either the shortest pulses or the highest pulse

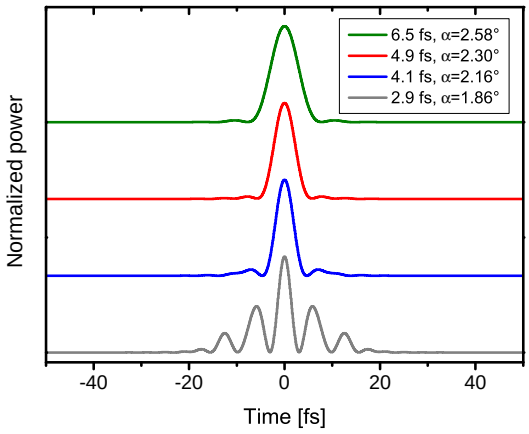

Figure 4.7 – Temporal envelope of the perfectly recompressed output pulses (flat spectral phase) for different noncollinear configurations.

peak power. In comparison to a linear analysis, including solely phase- and group-velocity matching, the effective pulse peak power is increased by 42 %. In addition, a slightly modified geometry has been found, resulting in only slightly lower peak power. It reduces the amount of energy in pre- and post-pulses, fits well to typical Ti:Sa oscillator spectra, still supports sub-5 fs pulses and is therefore used in most of the experiments presented in this thesis.

4.3 Gain narrowing and saturation effects

The parametric gain is local and instantaneous and thereofore strongly depends on the current pump intensity. If nonuniform temporal and spatial pump profiles are used, the parametric gain varies over the beam profile and the pulse shape. For Gaussian pump beam profiles, this leads to spatial gain narrowing which reduces the beam diameter towards the end of the nonlinear crystal, where most of the energy conversion takes place. The same behavior is observed in the temporal domain, when nonuniform (e.g. Gaussian) pump pulses are used. In consequence, high gain and high conversion efficiency can typically not be simultaneously achieved in a single parametric amplifier [53].

4.3.1 Spatial gain narrowing effects

For illustration of the spatial gain narrowing effect, the evolution of a signal beam with an initiall Gaussian distribution is shown in fig. 4.8 for different gain factors. A Gaussian pump beam with the same diameter as the initial signal is applied. The intensity profile of the depleted pump beam is also shown for the highest gain factor. As expected, the signal beam becomes narrower, because of the nonuniform gain and, finally, it depletes only the central part of the pump beam, thus reducing the conversion efficiency.

This effect has also been experimentally studied. For this purpose, a 1 mm long BBO crystal operated at degeneracy has been driven by different pump intensities. The average

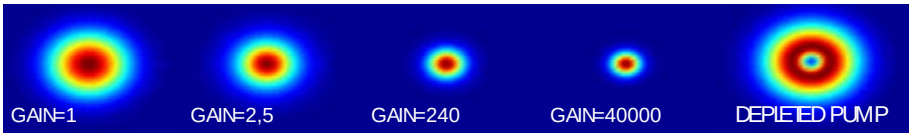

Figure 4.8 – Calculated intensity profile of an initially Gaussian signal beam after parametric amplification with a Gaussian pump beam for various gain factors. In addition the intensity profile of the depleted pump beam is shown for the highest gain.

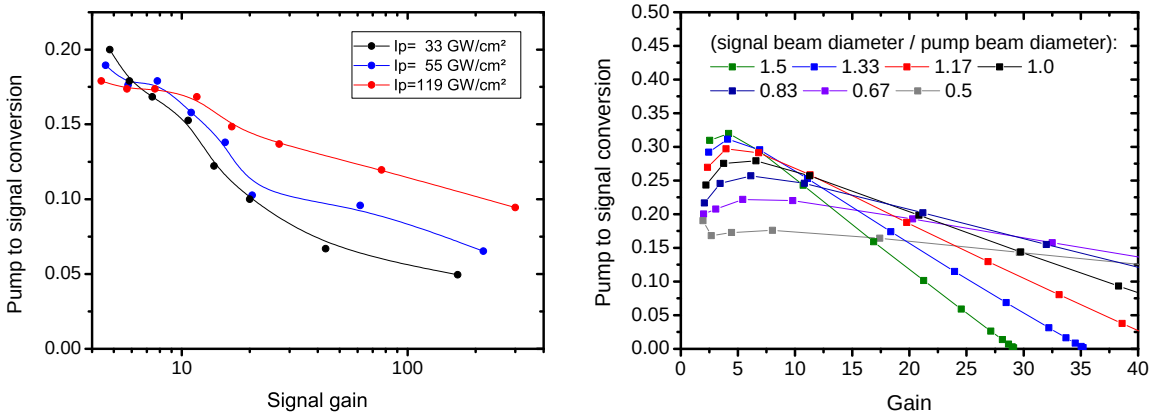

Figure 4.9 – a) Pump to signal conversion efficiency versus signal gain. Lines for eye guidance only (BBO, λ_s=1030 nm, λ_p=515 nm, nearly Gaussian pulses withτ_s=920 fs, τ_p=770 fs, $\alpha = 0.5°$, l=1 mm). b) Calculated pump to signal conversion efficiency plotted versus the signal gain. The different colors represent different signal diameters (BBO, collinear configuration, λ_s=1030 nm, λ_p=515 nm, d_{eff}=2.01 pm/V, I_p=57 GW/cm^2, l=1 mm, Gaussian pulses and beams).

output power of the amplified signal has been measured for various input signal powers. The achieved pump to signal conversion efficiency is plotted in fig. 4.9a versus the signal gain. It can be seen that the higher the signal gain the lower is the achieved conversion efficiency due to spatial narrowing of the signal beam. Nevertheless, a pump- to signal-conversion efficiency of 20 % is achieved for a gain factor of 4.8.

Clearly, to overcome this limitation, the use of flat-top beam profiles is beneficial. This leads to a uniform gain and uniform conversion without gain narrowing effects. A record high conversion efficiency of 29 % has been achieved by using spatio-temporal shaped pump pulses [54], but throughout this thesis Gaussian like beam profiles are inherently provided by the fiber amplifiers.

Another approach is to use a high gain preamplifier stage and a second low gain amplifier, which enables high conversion efficiency. The second amplification stage can be pumped by using the nearly undepleted remainder of the pump beam after the first, low conversion, amplifier. It is important to properly match the signal and pump beam diameters in both stages. In particular, the signal beam, which experiences strong spatial narrowing in the first

high gain OPA, has to be expanded prior further amplification, in order to achieve a high conversion efficiency.

In addition, spatial gain narrowing can be pre-compensated, at least partly, by using a signal input diameter which is slightly larger than the pump beam diameter. Figure 4.9 shows the results of a numerical calculation of the coupled wave equations (3.13 ... 3.15), which has been performed for a collinear OPA at degeneracy, utilizing different ratios of signal to pump beam diameter at the crystal input. Obviously, an increased signal diameter results in higher conversion efficiency for a low gain parametric amplifier and is therefore utilized in the experiments presented in this thesis.

4.3.2 Temporal gain narrowing effects

Since the parametric gain of the OPCPA sensitively depends on the instantaneous pump intensity, a uniform temporal pulse shape is desirable to achieve high conversion efficiency and to avoid gain narrowing effects. However, in most cases a pump pulse with a Gaussian or sech^2 temporal profile is delivered by the pump laser. In this case, the pump pulse has to be significantly longer than the signal pulses to avoid spectral narrowing of the chirped signal pulses during amplification and, in consequence, a large fraction of the pump pulse is not involved in the nonlinear process. This, in turn, lowers the overall conversion efficiency of the OPA. In contrast, a uniform rectangular temporal profile provides a uniform gain for all spectral components of the chirped signal, thereby avoiding spectral narrowing and increasing the pump to signal conversion efficiency. To investigate these effects in more detail, the coupled wave equations of the optical parametric amplifier (3.13 ... 3.15) are solved numerically for four different pump pulse shapes, shown in fig. 4.10a. Either a flattop pulse, a Gaussian shaped pulse or two temporally shaped pulses are assumed. The temporally shaped pulses consist of two or four overlapping Gaussian replicas and their generation will be studied in sec. 5.4 of this thesis. Since we want to simulate reasonable experimental conditions, the maximum number of Gaussian replicas is limited to four. It is important to know that the signal pulses are assumed to have a Gaussian spectrum (in frequency) with a spectral bandwidth of 100 nm (FWHM) at 800 nm central wavelength and these pulses are stretched to a pulse duration of 250 ps ($1/e^2$) by second order dispersion, in order to model a grating-type stretcher. For simplicity, uniform flat-top beams with the same diameter are assumed. Additionally, their transversal separation, due to the noncollinear angle, is neglected. Furthermore, perfect phase matching, which is satisfied for a large spectral range around 800 nm (see sec. 4.2.3), is assumed. The signal pulse energy has been chosen to result in 100 % pump depletion at the peak of the pump and signal pulses. Back conversion is avoided as it is known to distort the beam profile in real-world OPAs [53].

The resulting normalized spectra of the amplified signal are displayed in fig. 4.10b. The results, such as amplified signal pulse energies and pump to signal conversion efficiency, are summarized in tab. 4.2. Additionally, the Fourier-limited pulse duration and pulse peak

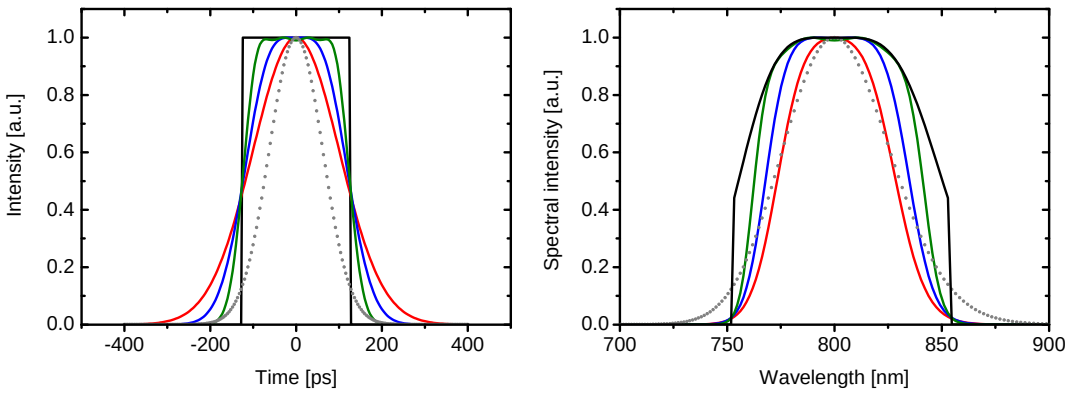

Figure 4.10 – a) Temporal pump pulse profiles b) corresponding spectra of the amplified signal pulses for different pump pulses (flattop - black; Gaussian - red, shaped of two Gaussian pulses - blue, shaped of four Gaussian pulses - green, signal - dotted grey). Simulation parameters: Pump pulse energy 5 mJ, signal pulse energy 2.3 µJ, pump pulse peak power 20 MW, λ_p=515 nm, l=10 mm, BBO, d_{eff}=2.0 pm/V, I_p =10 GW/cm².

pulse shape	pump pulse duration [ps]	signal pulse energy [mJ]	pump to signal conversion	compressed pulse duration [fs]	pulse peak power [GW]
flat-top	250	2.76	55.2 %	19.5	130.7
Gauss	236	1.79	35.8 %	21.7	78.5
shaped two Gauss	246	2.15	43.0 %	21.2	96.7
shaped four Gauss	251	2.45	49.0 %	20.6	112.4

Table 4.2 – Results of the simulation for different shaped pump pulses

power of the amplified signal pulses has been calculated, assuming zero phase for all spectral components, thus a perfect compressor.

It can be seen that the best results, in terms of conversion efficiency and pulse peak power of the recompressed amplified signal pulse, can be achieved with a flat-top pump pulse. In contrast, a Gaussian pump pulse leads to reduced conversion and, additionally, narrows the spectral bandwidth. This results in 40 % lower peak power of the recompressed amplified signal pulse. A temporal pump pulse profile, which consists of several Gaussian replicas, helps to increase the conversion efficiency substantially in comparison to a Gaussian pendant. Obviously, the more uniform the pump pulse (more Gaussian replicas), the higher is the conversion efficiency and the gain bandwidth.

Note that for real beam profiles and especially for Gaussian beams the overall conversion efficiencies is reduced, as already mentioned. However, the qualitative behavior in the temporal and spectral domain remains the same. Techniques to generate flat-top like temporal pulse profiles, to enhance the performance of OPCPA, will be presented in sec. 5.4 of this

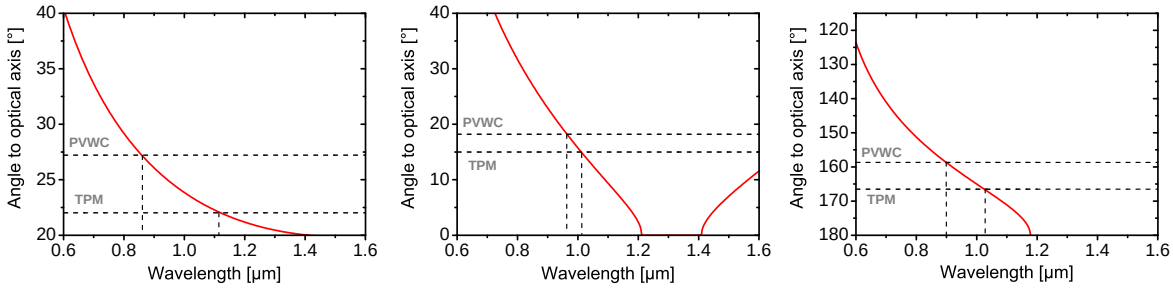

(a) BBO (b) LBO (c) BiBO

Figure 4.11 – Type I SHG phase matching curves (red) and internal signal angles for PVWC and TPM configuration (black dashed) for different nonlinear crystals. The crossing points represent the resulting SHG phase matched signal wavelength.

thesis.

4.4 Parasitic nonlinear effects

Crystal material	BBO		LBO		BiBO	
Phase-matching angle θ	24.2 °		15.2 °		166.6 °	
Noncollinear angle α	2.6 °		1.6 °		3.9 °	
Walk-off angle ρ	3.2 °		0.4 °		1.4 °	
	PVWC	TPM	PVWC	TPM	PVWC	TPM
Signal - pump angle	0.6 °	5.8 °	1.2 °	2.0 °	2.5 °	5.3 °

Table 4.3 – Geometrical angles of PVWC and TPM configuration, resulting signal- pump pointing vector angle for BBO, LBO and BiBO (λ_p=515 nm).

Parasitic SHG of the signal can be a severe limitation in optical parametric amplifiers. It leads not only to unwanted power loss, but also to distortions in the amplified spectrum. Table 4.3 outlines the important parameters for noncollinear BBO, LBO and BiBO optical parametric amplifiers. The noncollinear angle is chosen for group velocity matching of signal and idler. The angle between pump and signal pointing vector is calculated for both PVWC and TPM geometry. The resulting signal angle within the crystal is plotted in grey dashed lines for both configurations together with the corresponding SHG phase matching curves, in fig. 4.11 respectively. The SHG phase matched signal wavelength is recorded in tab. 4.4.

Certainly, also parasitic SHG of the idler wave may occur in OPCPA. For a detailed analysis, the internal angles of the idler wave has been calculated for both noncollinear configurations (PVWC and TPM) and the three crystals materials BBO, LBO and BiBO. The idler was assumed to compensate the wave vector component of the pump, which is perpendicular to the signal wave vector. The resulting internal idler angle with respect to the optical axis is plotted in fig. 4.12 together with the SHG phase matching curve.

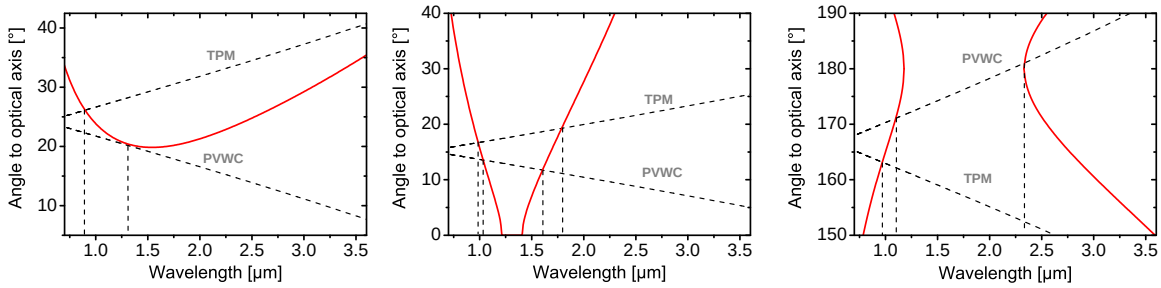

(a) BBO **(b)** LBO **(c)** BiBO

Figure 4.12 – Type I SHG phase matching curves (red) and internal idler angles for PVWC and TPM configuration (black dashed) for different nonlinear crystals. The crossing points represent the resulting SHG phase matched idler wavelength.

The resulting idler wavelengths, which are phase matched for second harmonic generation, and the corresponding signal wavelength (calculated due energy conservation law) are also displayed in tab. 4.4. The last row of tab. 4.4 represents the usable parasitic SHG-free signal wavelength range around 800 nm central wavelength. It has to be taken into account for the design of a broad band OPCPA system. Please note that deviations from the assumed noncollinear angles will shift the SHG phase matched wavelength slightly, though the general behavior remains the same.

Crystal material	BBO		LBO		BiBO	
	PVWC	TPM	PVWC	TPM	PVWC	TPM
Signal SHG wavelength [nm]	860	1119	963	1012	889	1025
Idler SHG wavelength [nm]	1265	864	1031 / 1607	983 / 1794	1102 / 2338	969
Signal wavelength for idler SHG [nm]	869	1275	1029 / 758	1082 / 722	966 / 660	1099
parasitic SHG free wavelength range [nm]	<860	<1119	758 ... 963	722 ... 1012	660 ... 889	<1025

Table 4.4 – SHG phase matched signal- and idler wavelength for BBO, LBO and BiBO in both PVWC and TPM configuration (λ_p=515 nm). The corresponding signal wavelength for parasitic idler SHG is calculated from the energy conversion. The parasitic SHG free wavelength range is summarized in the last row.

In summary, it can be stated that BBO in TPM configuration provides the largest spectral range (until ∼1119 nm) without parasitic SHG and should be preferably used for ultrabroadband amplification of few-cycle laser pulses. It is worth mentioning, that the occurrence of other parasitic nonlinear effects, such as DFG of signal and idler waves has been reported as well, for multiple beam pumped OPCPA [55].

Summary

In this chapter the most important theoretical aspects of high repetitive, high power OPCPA development have been discussed. It has been found that the OPA gain is limited by the angular acceptance of the crystal and by the transversal walk-off of the pump and signal waves. As a consequence, a pump pulse peak power of at least 2 MW is required to achieve significant parametric gain (G=10^3) in case of BBO in PVWC configuration.

In the second part of this chapter, the gain bandwidth of an OPCPA has been optimized both for collinear interaction at degeneracy and for noncollinear geometry. In both cases sub-5 fs pulses can be amplified, comprising an optimized geometry. To avoid optical damage of the crystals pump pulses shorter than 10 ps are required in this case. For nanosecond pump pulses, longer crystals operated at lower pump intensities are needed, resulting in reduced amplification bandwidth. Nevertheless, sub-20 fs pulses are still supported in this case.

In the third part gain narrowing effects in the spatial and temporal domain have been discussed. For the design of and efficient high gain parametric amplifier, which is driven by a Gaussian pump beam, a two amplification stage setup and flat-top temporal pulse profiles are found to be advantageous.

Lastly, phase matching for parasitic SHG of the signal or idler waves is calculated. A BBO in TPM geometry turned out to be the most suitable crystal for ultra-broadband parametric amplification in noncollinear OPCPA without distortions due to parasitic SHG. However, in this configuration a higher peak power pump laser is required. The next chapter will deal with the question: How to achieve the desired pump pulse parameters form a Yb-doped fiber laser, combined with very high average output power and good beam quality?

5 High average power pump laser for OPCPA

The pump laser mainly defines the pulse energy and the average power of the OPCPA system. In contrast to Ti:Sa lasers, Yb-doped gain media offer a significantly lower quantum defect [56]. Especially the fiber geometry allows for efficient heat dissipation, due to its large surface to active volume ratio. Average powers as high as 9.6 kW in diffraction-limited beam quality have been achieved in continuous-wave operation, demonstrating the high power capability of Yb-doped fiber lasers and amplifiers [24]. In pulsed operation 830 W average power have been recently generated with femtosecond pulses [25]. In addition, ultra-large mode area fibers, which reduce the intensity in the fiber core, enabled pulse energies as high as 2 mJ with nanosecond pulses [57]. By exploiting chirped pulse amplification, 1 mJ pulse energy has been achieved with femtosecond pulses [58]. Although the gain bandwidth of Yb-doped fibers does not support sub-100 fs pulses from high energy amplifiers [56], they are prominent candidates for driving OPCPA systems to the highest average power levels.

Pump laser requirements

As shown in the previous chapter, there are several requirements on the pump laser for OPCPA.

1. The peak power of the pump pulse needs to be at least several MW (with good beam quality) to achieve sufficient gain in the OPA.
2. The pump pulses have to be temporally synchronized with the signal pulses.
3. For a few-cycle OPCPA, very short pump pulses are advantageous, as they allow for higher pump intensities without crystal damage and, consequently, shorter crystal lengths.
4. Second harmonic generation of near infrared pump lasers is required in order to drive OPAs in the visible and near infrared spectral region.
5. A flat-top temporal and spatial profile can be helpful to avoid gain narrowing effects in the temporal domain.

Yb-doped fiber lasers can fulfill these requirements and, at the same time, emit very high average powers. The general properties of Yb-doped fiber amplifiers are presented at the

beginning of this chapter. In order to achieve the necessary peak power for OPCPA pumping, short laser pulses are required. However, short pulse fiber lasers suffer especially from nonlinear effects, which will be briefly introduced. It turns out that the performance of short pulse fiber amplifiers basically and essentially relays on the reduction of the peak intensity inside of the active fiber core. This strategy simultaneously prevents optical damage and nonlinear distortions of the laser pulses. Despite avoiding nonlinear distortions of the pump pulses, their synchronization with the signal pulse plays a key role in OPCPA systems. This topic will be discussed in the third part of this chapter.

Experimentally, the pump pulses for OPCPA have been generated by two different approaches. Very high peak power femtosecond pulses can be achieved with the well known chirped pulse amplification technique (CPA) [59]. A fiber CPA system (FCPA), delivering millijoule femtosecond pulses is presented in the third part of this chapter. An alternative way is to extract MW peak power nanosecond or sub-ns pulses directly from an ultra-large-mode area fiber. In the frame of this work, such a high energy nanosecond fiber amplifier has been developed, assembled and successfully employed as OPCPA pump. The setup and the experimental results are presented in the fourth part of this chapter.

5.1 Properties of Yb-doped fiber lasers

5.1.1 Double-clad step-index and photonic crystal fibers

When compared with bulk laser media, optical fibers posess several outstanding properties. When properly designed and manufactured, the core guides only the fundamental mode, which exhibits a nearly Gaussian intensity distribution and, therefore, excellent beam quality. In step-index fibers, the light guidance is given by the refractive index difference between core and cladding (see fig. 5.1a). In addition, active fibers are doped with rare-earth ions within the core region. So-called double-clad fibers [60] have a special low index polymer coating around the fiber cladding to provide guidance of low brightness pump light within a second pump core. This feature enables efficient coupling of the pump light emitted by high power laser diode bars and stacks. The pump light is absorbed in the doped region of the fiber (active core) as it propagates along the fiber and, therefore, allows for high average power pumping of fiber lasers and amplifiers.

Micro-structured or photonic crystal fibers (PCFs) provide additional degrees of freedom in the fiber design. Here the fiber core is surrounded by air holes, which define the guiding properties of the fibers (see fig. 5.1b). Precise control of the air hole pitch Λ and diameter d allows for ultra-large mode field diameters [61], thus significantly reducing the intensity in the fiber core. In addition, the pump core can be surrounded by a so-called air-clad which results in a large refractive index difference. The resulting numerical aperture (NA) of the pump core can exceed 0.6 [61], which is significantly higher than that for polymer coated fibers with a typical pump core NA of 0.46 [62]. Consequently the requirements on the pump

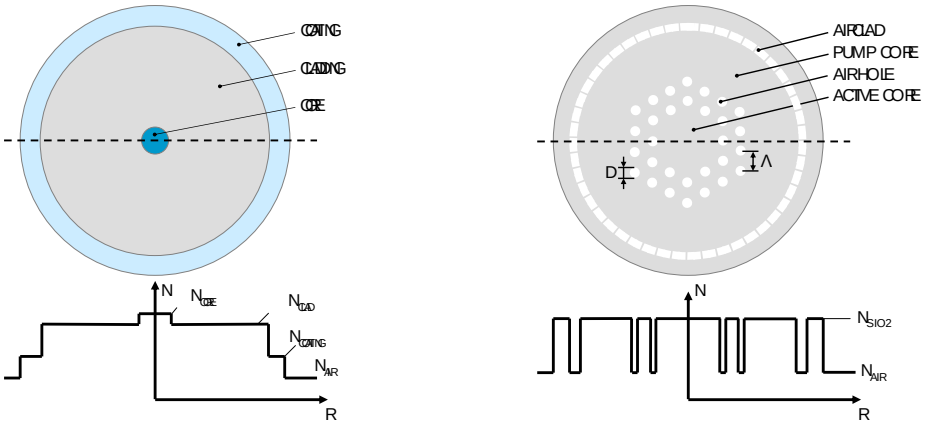

(a) Step-index fiber **(b)** Photonic crystal fiber (PCF)

Figure 5.1 – Cross-section and refractive radial index profile of a) double-clad step-index fiber and b) air-clad PCF.

diode beam quality are lowered.

5.1.2 Yb^{3+}-doped fiber as high average power lasers and amplifiers

The Yb^{3+}-ion is one of the most prominent rare-earth ions in laser physics due to its outstanding properties. First, it possesses very simple energy levels, with only one exited state manifold within reach of the ground state manifold, when absorbing visible or near-infrared photons [56]. In Yb^{3+}-doped glass media a relatively large emission bandwidth is found, which supports about one hundred femtoseconds pulse durations. In addition, the upper state lifetime is relatively long (∼1 ms). The corresponding absorption and emission cross-sections of Yb^{3+} doped germanosilicate glass are shown in fig. 5.2. It can be seen that a strong absorption is present at 976 nm, which is typically used for pumping, resulting in a low quantum defect of less than 6 %, for 1030 nm emission. In combination with the fiber geometry, which offers a very large ratio of cooling surface to active volume and, therefore, relaxed thermal management, extraordinarily high average output powers have been achieved in cw operation [24], demonstrating the sutability of Yb-doped fibers for high average power lasers.

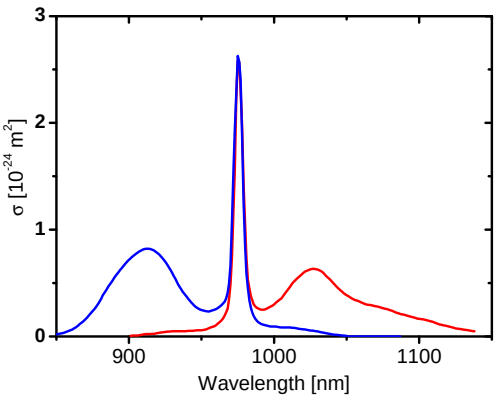

Figure 5.2 – Absorption (blue) and emission cross-section (red) of Yb^{3+}-doped germanosilicate glass [56].

5.1.3 Nonlinear effects in fused silica fibers

Besides their manifold advantages, optical fibers they suffer from nonlinear effects. Due to the tight confinement of the light in the fiber core, large intensities are present over long interaction lengths, thus enhancing nonlinear effects. As a result of symmetry in fused silica, the second order susceptibility is zero and third order nonlinear effects, such as the optical Kerr effect, dominate the propagation of ultra-short pulses in optical fibers.

Kerr effect

The Kerr effect is an intrinsically phase matched nonlinear effect, whereas only photons of the same frequency interact. As a result an intensity dependence of the refractive index is observed

$$n(I) = n_0 + n_2 I, \tag{5.1}$$

where the nonlinear refractive index for linearly n_2^l and for circularly polarized light n_2^c is given by [63]

$$\begin{aligned} n_2^l &= \frac{3Re(\chi^{(3)}_{xxxx})}{4\epsilon_0 c_0 n_0^2}, \\ n_2^c &= \frac{2Re(\chi^{(3)}_{xxxx})}{4\epsilon_0 c_0 n_0^2}. \end{aligned} \tag{5.2}$$

The intensity dependent refractive index is assumed to be instantaneous and local. It has consequences for the propagation of light in the temporal domain, namely self-phase modulation, as well as in the spatial domain in form of self-focusing.

Self-focusing

Self-focusing occurs, when a beam with nonuniform intensity profile is propagating through a medium with a nonlinear index of refraction. Neglecting saturation effects, the refractive index $n(I)$ follows the intensity profile and forms an index gradient. For positive n_2 the

high intensity parts, typically located in the center of the beam, travel slower than the low intensity wings, leading to focusing of the beam, as illustrated in fig. 5.3a. For high peak power pulses and long propagation distances, self-focusing can lead to a beam collapse. In contrast to other nonlinear effects, self-focusing is proportional to the pulse peak power P_P, because a larger beam with lower intensity is more sensitive to phase distortions. If a critical value of power P_P^{cr} is reached, the beam collapses. Already below this threshold ($P_P < P_P^{cr}$) this leads to mode shrinking in large mode optical fibers and the damage threshold can be reached. In the literature, for fused silica at 1030 nm wavelength, the critical power is found to be 5.2 MW for linear polarization [64]. It is worth mentioning that for circular polarized light the critical power is increased by a factor of 1.5, due to the reduced value of n_2. For pulses longer than ∼1 ns the contribution of electrostriction has to be additionally accounted for, thus reducing the critical power of self focusing to 4.25 MW and 5.83 MW for linear and circular light respectively [64]. In optical fibers, self-focusing can significantly contribute to optical damage, due to shrinking of the mode field area or beam collapse. Therefore, the peak power in a fiber amplifier has to be lower than the critical power of self-focusing in order to prevent optical damage. In large mode area fibers mode shrinking, caused by self-focusing, is already observed at peak powers far below the critical power [65]. Detailed discussions on the performance limitations of pulsed fiber amplifiers will be the topic of sec. 7 of this thesis.

Self-phase modulation

Self-phase modulation (SPM) is the temporal counterpart of self-focusing. If an intense laser pulse with the intensity profile $I(t)$ propagates through a nonlinear medium, it accumulates an additional time dependent phase $\varphi_{NL}(t)$, which is caused by the nonlinear index of refraction and can be written as

$$\varphi_{NL}(t) = -\frac{\omega_0}{c_0} n_2 I(t). \tag{5.3}$$

As a result, an instantaneous frequency shift can be calculated as

$$\omega(t) = \omega_0 + \frac{\partial \varphi_{NL}}{\partial t}, \tag{5.4}$$

if a slowly varying envelope is assumed. Thus, the frequency shift at the peak is zero and the leading edge is red shifted while the trailing edge is blue shifted in a positive nonlinear medium, leading to a spectral broadening of initially positively or unchirped laser pulses. If anomalous dispersion is present, SPM and dispersion can balance. As a result, the so-called optical solitons propagate in optical fibers with constant shape and amplitude, as long as perturbations by higher order dispersion and other nonlinear effects are small [35].

In pulsed fiber amplifiers, spectral broadening due to SPM is typically unwanted. Additionally, in case of chirped pulse amplification, the imposed nonlinear phase results in a spectral phase, which cannot be easily compensated for and degrades the recompressed pulse quality. A measure for the accumulated nonlinear phase produced by the peak intensity$I(z)$

along the fiber length l is the B-Integral, which is defined as

$$B = \frac{2\pi}{\lambda} \int_0^l n_2 I(z)\, dz.$$

The influence of the nonlinear phase on the output pulses of a CPA system is displayed in fig. 5.3b. The accumulated nonlinear phase leads to energy transfer into pre- and post-pulses and to an increased pulse duration of the main pulse, hence the pulse peak power is reduced dramatically. In high energy FCPA systems the B-Integral is reduced by using short length large mode area fibers and stretching to the highest possible pulse durations [58]. Another possibility is to control or compensate the nonlinear phase in FCPA by amplitude and phase shaping strategies, which have been presented in detail in [33].

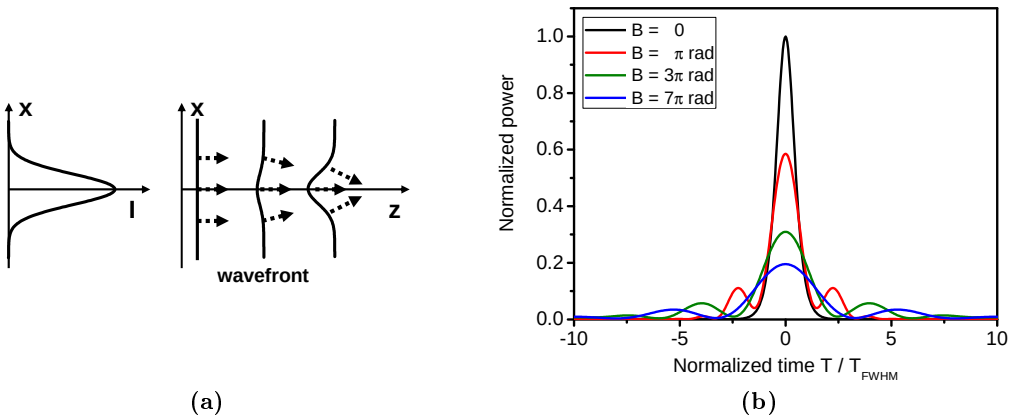

(a) **(b)**

Figure 5.3 – a) Illustration of a Gaussian beam, which propagates in a positive nonlinear medium and is focused due to the Kerr effect. b) Pulse profile of a FCPA output pulse at the point of best compression (maximum peak power) for various B-Integrals, assuming a transform-limited sech^2- input pulse.

5.1.4 Stimulated Raman scattering

Raman scattering is a non-instantaneous inelastic process, which can be described as scattering between photons and optical phonons, as illustrated in fig. 5.4a. In the case of stimulated Raman scattering (SRS) the generated Stokes-wave propagates with the driving laser field. Thus, it gives rise to a coherent stokes emission, resulting in amplification of the stokes wave (fig. 5.4b). In fused silica at 1 µm pump wavelength the maximum Raman gain is observed at 13 THz frequency shift. The corresponding Raman gain spectrum is shown in fig. 5.4c).

In fiber lasers and amplifiers SRS leads to a typically undesired energy loss at the fundamental wavelength if the Raman threshold intensity is exceeded. However, the use of short length large mode area fibers in the experiments presented in this thesis, effectively avoids the onset of SRS. Nevertheless, it still remains an issue for further scaling considerations, which will be the toppic of chapter 7.

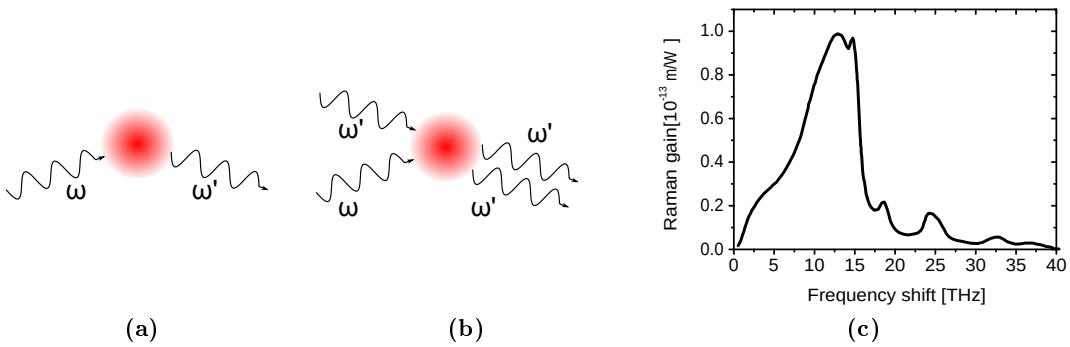

Figure 5.4 – Schematic diagram of a) spontaneous Raman scattering and b) stimulated Raman scattering, c) measured Raman gain spectrum for fused silica at 1 µm pump wavelength [35].

In special cases Raman scattering is desired, e.g. to achieve an effectively shifting of the spectral envelope of ultra-short optical pulses towards longer wavelengths. This Raman self-frequency shift, also-called soliton self-frequency shift is useful for the optical synchronization of pump laser and seed oscillator for ultra-short pulse OPCPA, which is discussed more precisely in subsection 5.2 of this chapter.

For the sake of completeness, it has to be mentioned that photons can also be scattered by acoustical phonons. This effect is called Brillouin scattering and the resulting frequency shift is three orders of magnitude smaller than the Raman shift, due to the lower phonon energy. Stimulated Brillouin scattering (SBS) is typically not observed for short optical pulses ($<$1 ns) as the spectral bandwidth of the pulses is significantly larger than the Brillouin gain bandwidth [35].

5.2 Optical synchronization - soliton self frequency shift

Nonlinear effects are typically unwanted in a fiber laser system. Despite of this, they can also be useful for spectral broadening or frequency conversion in optical fibers, which can be employed for optical synchronization of signal and pump pulses for OPCPA. This temporal synchronization is required due to the instantaneous nature of the optical parametric processes. Known synchronization techniques are e.g. based on costly GHZ electronics [66], however they cannot achieve femtosecond accuracy and are, therefore, inapplicable for sub-ps pump lasers. An alternative is to use the same pulsed laser in order to generate a broadband signal via SPM based spectral broadening and a frequency doubled pump. This technique has been applied for an OPCPA system, operated at degeneracy, which will be presented in sec. 6.1 of this thesis.

In contrast, few-cycle laser pulses are delivered directly by Ti:Sa based oscillators, without the need of complex spectral broadening [67]. Unfortunately, the emission bandwidth of these oscillators normally does not significantly overlap with the gain bandwidth of a 976 nm-

pumped Yb-doped fiber amplifier, which is typically located around 1030 nm. In principle, it is possible to seed a short pulse Yb-doped fiber amplifier with Ti:Sapphire oscillators, utilizing specially designed output couplers and cavity mirrors [68]. However, with typical Ti:Sa oscillators it is difficult to ensure picojoule energy levels within the bandwidth of a typical Yb - doped fiber amplifier, which is required to efficiently compete with the amplified spontaneous emission (ASE).

To enhance the seed pulse energy, a resonant frequency conversion is needed. The special properties of soliton phenomena in optical fibers suggest an interesting possibility. Specially designed photonic-crystal fibers, possessing very small mode field diameters, substantially enhance nonlinear optical processes due to a strong field confinement, which is exactly the opposite aim, compared to large-mode area fibers. Furthermore, the dispersion properties of these fibers can be tailored to some extent. Tighter confinement in the fiber core leads to smaller mode field areas and, normally, shifts the zero dispersion wavelength (ZDW) towards lower wavelengths due to waveguide dispersion. Within the negative dispersion region, formation of solitons gets feasible [35] which experience continuous frequency downshifting due to the Raman-effect. This so-called soliton self-frequency shift (SSFS) provides a convenient way of tuning the central wavelength of the generated ultra short pulse [69], and has been successfully implemented in few-cycle OPCPA systems [23]. One possibility is to launch the pulses in the negative dispersion region. In case of Ti:Sa oscillators this requires a fiber with a ZDW lower than 800 nm. The photonic crystal fiber NL-PM-750 fulfills these requirements, and provides a ZDW of 750 nm, a mode field diameter of 1.6 µm at 780 nm wavelength and, in addition, a polarization-maintaining core design.

Another possibility is to launch the seed pulse below the ZDW. Here, spectral broadening and dispersive pulse stretching occur. If the broadened spectrum grows into the negative dispersion region, formation of solitons is feasible. If the pulse parameters are properly chosen, a single fundamental soliton can be exited. For special cases, e.g. if the pulses are launched at 800 nm central wavelength into a 975 nm ZDW fiber (crystal fiber NL-3.7-975) the soliton is exited exactly at the desired wavelength and no SSFS is required at all. The experimentally measured spectra and the corresponding numerical results[1] (black) are shown in fig. 5.5 for both cases. In addition, the spectral evolution is displayed over the fiber length (fig. 5.5) b) and d)). In the case of NL-975 fiber, large spectral broadening occurs initially, resulting in a spectral overlap with the negative GVD region. In consequence, a fundamental soliton is formed, which propagates through the fiber without significant frequency shift. Experimentally, about 5 pJ pulse energy within the Yb-gain bandwidth (1030 nm±5 nm) is measured and confirmed by numerical simulations for 1.1 nJ, 20 fs input pulses.

Within the NL-PM-750 fiber, a fundamental soliton is initially generated and continuously frequency shifted towards longer wavelengths. In this case, the measurements show

[1] The numerical simulation is based on a split-step method, solving the nonlinear Schrödinger equation including dispersion, SPM, SRS and self-steepening. Please note that the wavelength dependence of the mode field diameter and losses are not included in the simulation.

a 2 pJ pulse energy within the Yb-gain bandwidth for 250 pJ, 10 fs input pulses, while the corresponding numerical simulation yields 39 pJ pulse energy (1030 nm±5 nm). This difference can be attributed to fabrication tolerances, which can shift the ZDW slightly towards longer wavelengths. Hence, a larger amount of the initial spectrum is not involved in soliton generation and remains unconverted.

Interestingly, numerical simulations revealed that amplitude fluctuations (<1 %) at the input of the NL-PM-750 result in nearly 3 times larger energy fluctuations within the Yb-gain bandwidth (1030 nm±5 nm), measured at the fiber output. In contrast, using the NL-975 fiber reducedes input ampliftude fluctuations due to the wavelength shift mechanism. The amplitude fluctuations, found within the Yb-gain bandwidth at the output are a factor of two lower compared the the amplitude noise of the input pulses.

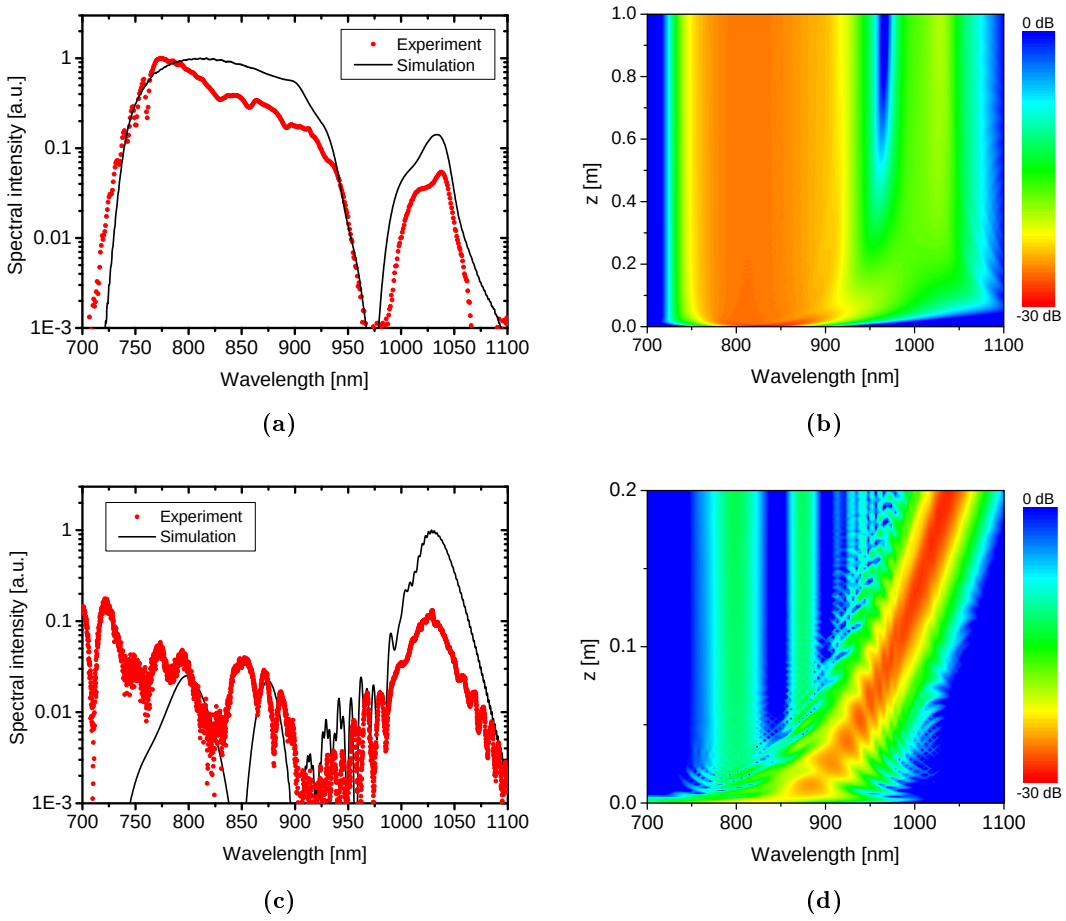

Figure 5.5 – Generation of synchronized pulses in the Yb-gain region around 1030 nm: a) Measured spectrum (red dots) and corresponding numerical result (black line) for 1.1 nJ, 20 fs pulses, launched into 1 m NL-3.7-975 fiber. b) Results of a numerical simulation showing the spectral evolution of the launched 1.1 nJ, 20 fs pulses within 1 m of NL-3.7-975 fiber. c) Measured spectrum (red dots) and numerical result (black line) for 250 pJ, 10 fs pulses, launched into 0.13 m NL-PM-750 fiber. d) Results of a numerical simulation showing the spectral evolution of the launched 200 pJ, 10 fs pulses within 0.2 m of NL-PM-750 fiber.

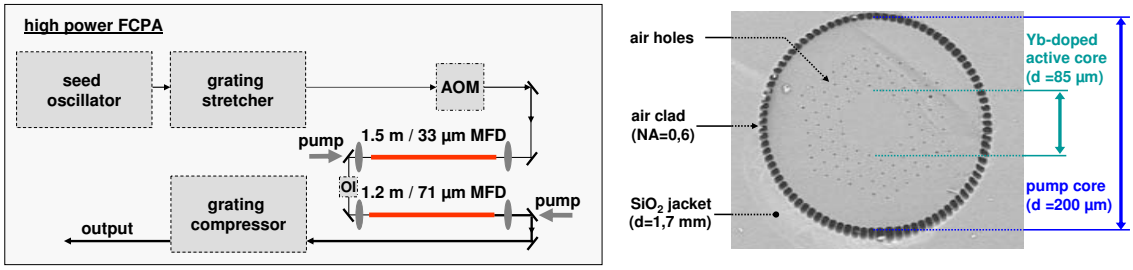

(a) (b)

Figure 5.6 – a) Schematic setup of the mJ-class FCPA system, including seed oscillator, grating stretcher and compressor, acousto-optical modulator (AOM), preamplifier (33 µm mode field diameter photonic crystal fiber), main amplifier (71 µm mode field diameter PCF) and optical isolator (OI), b) Scanning electron microscope image of the 85/200 rod-type PCF.

5.3 Femtosecond mJ-class FCPA

As already mentioned, chirped pulse amplification significantly reduces the impact of nonlinear effects on the amplified pulses. Therefore, high pulse energies can be extracted from a fiber amplifier, providing the highest peak power femtosecond pulses after recompression. Applying these pulses as OPCPA pump comes along with the advantage of a high damage threshold intensity and low stretching ratio within the OPCPA setup, which is especially suitable for few-cycle amplification.

Today, the highest pulse energy femtosecond pulses (1 mJ) extracted from a fiber amplifier have been achieved with an FCPA system, which is briefly presented in this section [58]. Figure 5.6a shows the experimental setup of the mJ-FCPA system. This system is used to amplify either Yb:KGW oscillator pulses (see fig. 5.6a) or alternatively, a Ti:Sa oscillator that has been frequency shifted by the soliton based methods presented above. To lower the influence of nonlinear effects (mainly SPM) on the amplified laser pulses, three approaches have been simultaneously implemented in the FCPA system. At first, the well-known CPA principle is applied and femtosecond laser pulses are stretched to 1.5 ns duration prior amplification in a grating stretcher. Second, large mode area fibers are used in both amplifier stages. The preamplifier fiber consists of a 1.2 m long 170/40 double-clad PCF, with a MFD of 33 µm [70]. For the main amplifier a special ultra-large mode area rod-type fiber has been developed, which offers a mode field diameter (MFD) as large as 71 µm and good beam quality (see fig. 5.7b), if the fundamental mode is properly exited. The resulting mode field area (4000 μm^2) is more than two orders of magnitude larger than that of standard step-index fibers (MFD: 6 µm, mode field area 28 μm^2), reducing the intensity in the fiber core by more than two orders of magnitude. Third, due to the high Yb^{3+}-concentration ($3.2 \cdot 10^{25} ions/m^3$) and the large ratio of active core diameter to pump core diameter, the fiber possesses a high pump absorption at 976 nm (30 db/m) and, therefore, allows for efficient pump absorption at

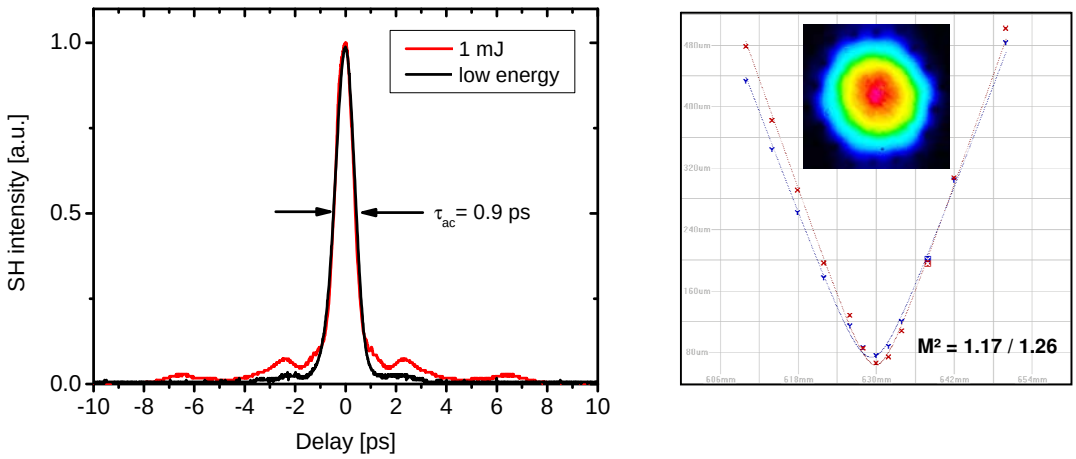

Figure 5.7 – a) Measured autocorrelation trace of the compressed output pulses at low pulse energy (black) and 1 mJ pulse energy (red), b) Caustic of the beam quality measurement of the emitted radiation at 100 W compressed output power, inset: near field image of the emitted fundamental mode [73].

very short fiber lengths. The cross-section of the fiber is shown in fig. 5.6b. The Yb-doped active core (d=85 µm) is surrounded by very small air-holes. An additional air-clad confines the pump light in a 200 µm diameter pump core (NA=0.6). Both fiber amplifiers are pumped by fiber coupled laser diodes operating at 976 nm, which are imaged into the pump core of the active fibers, respectively. An acousto-optical modulator (AOM) is employed to reduce the repetition rate, and an optical isolator (OI) avoids optical feedback between the amplifiers. After amplification the pulses are recompressed by a dielectric grating pair with a throughput efficiency of 70 %. More details on the FCPA system and its modifications for OPCPA pumping can be found in [58, 71, 72]. A measured autocorrelation trace of the infrared output pulses (λ_c=1030 nm) is shown in fig. 5.7a for low (∼5 µJ) pulse energy (black) and 1 mJ pulse energy (red), revealing a pulse duration of 640 fs (Gaussian pulse shape assumed). The pulse quality degrades for high output pulse energies. This is caused by the nonlinear phase which is imposed onto the chirped pulse in the fiber amplifier. The resulting spectral phase cannot be fully compensated by the compressor and therefore sets a limit to the meaningful pulse energy which can be extracted from the laser system at reasonable pulse quality. For 1 mJ compressed pulse energy the corresponding B-Integral within the FCPA system is already as high as 8.5 rad [73]. A detailed discussion of the limits and scalability of the presented FCPA system is found in chapter 7 of this thesis.

Lastly, it is worth mentioning, that the FCPA system possesses excellent beam quality with a measured M^2<1.3 at 100 W output power (see fig. 5.7b). Within the frame of this work the second harmonic of the presented FCPA system is used to drive both an OPCPA operating at degeneracy (see sec. 6.1) and a few-cycle OPCPA system, which is seeded by a broadband Ti:Sa oscillator (see sec. 6.3).

5.4 High energy ns fiber amplifier

An interesting alternative to FCPA systems as OPCPA pump are ns fiber amplifiers. Here, the pulse energy is not limited by nonlinear distortion of the temporal pulse profile. When working with ultra-large mode area fibers, as presented in the previous section, the extractable pulse energy is only limited by the onset of self focusing at a peak power of several MW. Applying these fibers for ns amplifiers, spectral broadening due to SPM is normally negligible and SRS is not observed up to the highest peak powers [74, 57, 75].

Due to their buildup from noise [76], q-switched oscillators typically suffer from timing jitter (typically in the ns rage) and therefore are not ideal for OPCPA pumping. In this content it is worth mentioning that a passively q-switched microchip laser has been successfully synchronized with a Ti:Sa oscillator, reducing the relative timing jitter between both lasers to 40 ps by bleaching the saturable absorber mirror with a femtosecond trigger pulse [77]. Unfortunately, the emission bandwidth of the Nd:YVO_4 based microchip laser is not ideal for amplification with short length Yb-doped fibers. Hence, this approach has not been implemented in pump lasers within the frame of this thesis, however remains an interesting option.

An optical synchronization scheme for femtosecond pulses has already been presented in sec. 5.2, though the pulse duration and spectral bandwidth is not adequate for sub-ns and ns pulses. Spectral filtering remains a possibility, which can be implemented easily in fiber amplifier chains via fiber Bragg gratings, and will be discussed in the next section. A further increase in pulse duration and generation of a flat-top temporal pulse shape is achieved by a pulse stacker, which is implemented in the preamplifier section as well. This pulse stacker will be the focus of the second sub-section. Finally the performance of the high energy ns fiber amplifier is presented.

Picosecond pulse generation via spectral filtering

Spectral filtering is an adequate method to reduce the bandwidth of optical pulses. For sub-100 pm bandwidth, dispersion is usually negligible and the pulses are nearly transform limited. This means that the optical spectrum directly translates into the temporal pulse profile via the Fourier-transform, assuming a flat-spectral phase.

Fiber Bragg gratings afford implementation of the spectral filter into a fiber amplifier chain. The corresponding experimental setup is shown in fig. 5.8. At first, the seed pulses delivered by a Ti:Sa oscillator are frequency shifted in a PCF NL-975 to the Yb-gain region, as introduced in sec. 5.2. The pulses are then directed to a Yb-doped fiber amplifier via a fiber optical circulator. The pump light is coupled to the active fiber via a wavelength division multiplexer (WDM). After the first pass through the fiber amplifier, a fraction ($\Delta\lambda$=1 nm) of the amplified spectrum is reflected by a FBG and amplified in a second pass. A second preamplifier is applied and a second FBG is used to reduce the spectral bandwidth down

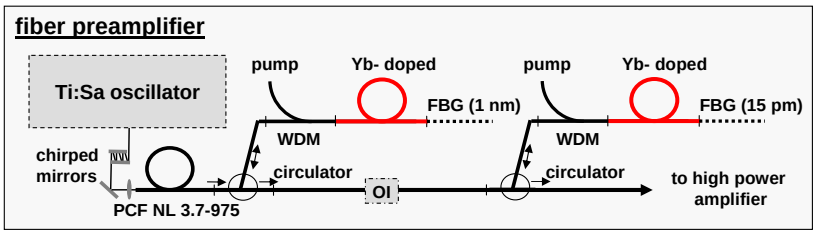

Figure 5.8 – Experimental setup of an all fiber preamplifier with FBGs for spectral filtering (OI-optical isolator, WDM-wavelength division multiplexer, FBG-fiber Bragg grating).

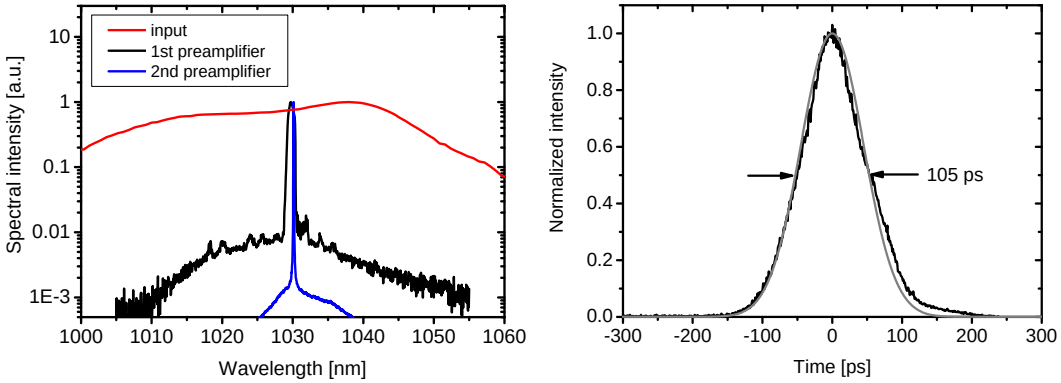

Figure 5.9 – a) Measured spectra of the amplifier seed (red), after the first preamplifier (black) and after the second preamplifier (blue), b) Measured pulse shape of the spectrally filtered pulses at the output of the second preamplifier (black) and corresponding Gaussian fit (grey).

to 15 pm. The corresponding measured spectra are displayed in fig. 5.9a and the resulting temporal pulse shape is shown in fig. 5.9b (black) together with a Gaussian fit (grey). The resulting pulse width is 105 ps (FWHM). As introduced in the second part of this chapter, fiber optical damage is strongly related to the peak power of the pulses. Consequently, a longer pulse can extract a higher energy from the fiber amplifier and is therefore desired. Certainly, the spectral bandwidth of a FBG can only be further reduced by increasing the refractive index modulation or the grating length [78], which both underlie practical limitations. The generation of longer pulses, which are composed of multiple sub-pulses will be in focus of the next section. Additionally, the presented methods allow for control of the temporal pulse shape, e.g. the generation of a flat-top like temporal pulse profile.

Birefringent pulse stacker for flat-top pulse generation

Pulse shapers are typically known for femtosecond pulses and are usually based on two gratings placed in the focal plane of a confocal lens or mirror pair and a spatial light modulator located in the Fourier plane [79]. However, for pico- and nanosecond pulses there is a simple and robust shaping method: the so-called pulse stacking. A pulse stacker splits an incident

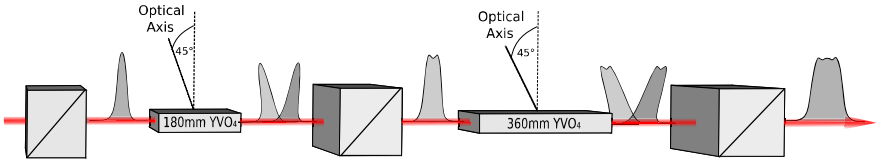

Figure 5.10 – Schematic setup of the two stage birefringent pulse shaper.

laser pulse into several replicas, which are then recombined after traveling different optical path lengths [80]. The output pulse is formed by interference of the sub-pulses. Especially pulse stackers based on birefringent crystals provide a simple experimental setup and phase control of the superimposed pulse replicas via tuning of the crystal temperature [81, 82].

As the stacked pulse is longer than the input pulse, it allows for higher pulse energies to be extracted from a fiber amplifier. In addition, a flat-top temporal pulse shape can be achieved, which potentially enhances the conversion efficiency and reduces spectral narrowing of the chirped signal within an OPCPA (see sec. 4.3). Furthermore, the pulse shaping abilities are sufficient to pre-compensate altering of the pulses during amplification, which is a well known phenomenon for saturated laser amplifiers [83].

The principle of a two stage birefringent pulse stacker is shown in fig. 5.10. The device is based on birefringent Yttrium Orthovanadate (YVO_4) crystals. For flat-top pulse generation, the polarization of the optical pulses is set 45 degrees with respect to the optical axis of the crystal in front of each stage. Therefore, the same ammount of optical power is polarized ordinaryly and extraordinaryly. At the end of each crystal two pulse replicas experience a temporal delay and interfere at a polarizer, which is orientated 45 degrees with respect to the optical axis and is located at the crystal output. The two stages provide 133 ps and 266 ps delay with a crystal length of 180 mm and 360 mm, respectively. Temperature control of the crystals allows for fine tuning of the relative phases of the interfering sub-pulses. The relative amplitudes of the sub-pulses can be controlled by half-wave plates in front of each stage. The generated pulses consist of four sub-pulses, which are measured at the shaper output and displayed in fig. 5.11a. If the polarization in front of the second YVO_4 is set to ordinary (fast axis), the second stage is inoperable and the shaped output pulse contains only two sub-pulses. The corresponding measured temporal profiles are shown in fig. 5.11b. Temperature tuning of the crystal allows for the control of the relative phase between the two sub-pulses, resulting in either constructive (black curve) or destructive interference (green curve) in the overlap region of both pulses. For a temperature of 31.8 °C, a nearly flat-top pulse shape is achieved (blue curve). The second stage follows the same physical principles and stacks the two pulse replica of the flat-top pulse emerging from the first stage with a doubled temporal delay. The resulting pulse shape (black) and the fast- and slow-axis pulse replica (red / blue) are displayed in fig. 5.11c, together with the measured angle between input polarization and optical axis. The generated flat-top like pulses feature a pulse duration of 460 ps (FWHM).

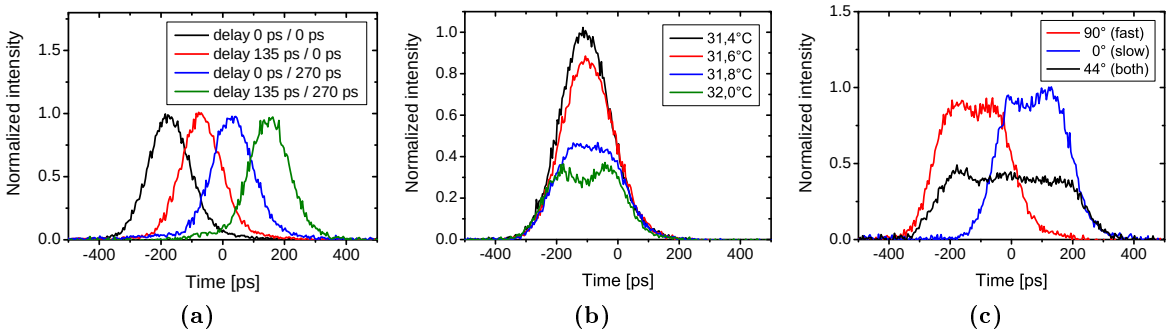

Figure 5.11 – Measured temporal pulse profiles at the output of the two-stage birefringent pulse shaper: a) Measured four pulse replica with different temporal delay with respect to the first pulse, b) Influence of temperature tuning on the pulse shape. For clearness this measurement shows the combination of two sub-pulses. c) Temporal shape of the output pulses of the two stage pulse stacker, demonstrating the influence of polarization. The angle, measured between the axis of linear polarization prior to the second crystal and the optical axis of the crystal, is displayed in the legend.

Figure 5.12 – Schematic of a fiber optical pulse shaper consisting of a circulator (circ) and four fiber Bragg gratings (FBG1, ... , FBG4)

Fiber Bragg grating pulse stacker for flat-top pulse generation

In fiber based pump lasers or amplifiers an alignment-free fiber-integrated pulse shaper is especially desirable. A picosecond pulse stacker based on fiber couplers has been reported [84]. However, phase control of the interfering sub-pulses was not given during this experiment, which led to strongly modulated pulse shapes.

Within the frame of this work, a very simple pulse shaper based on fiber Bragg gratings (FBGs) has been developed. The FBGs are arranged linearly in a fiber with a certain distance, as shown in fig. 5.12, giving a corresponding temporal delay. Every grating reflects a sub-pulse and these sub-pulses interfere in backwards direction. Splicing this fiber to a fiber optical circulator leads to a simple, compact, monolithic and alignment free pulse shaper. More details on the specific design, fabrication and characterization of the device can be found in [85]. Please note that the relative phases and amplitudes of the interfering sub-pulses are controlled via temperature tuning of the FBGs and the intermediate fiber sections. Characteristic measured pulse profiles at the output of the fiber pulse stacker are displayed in fig. 5.13. Fine tuning of the temperature allows, to enhance the leading or trailing edge of the pulse, displayed by the blue and black curve in fig. 5.13a.

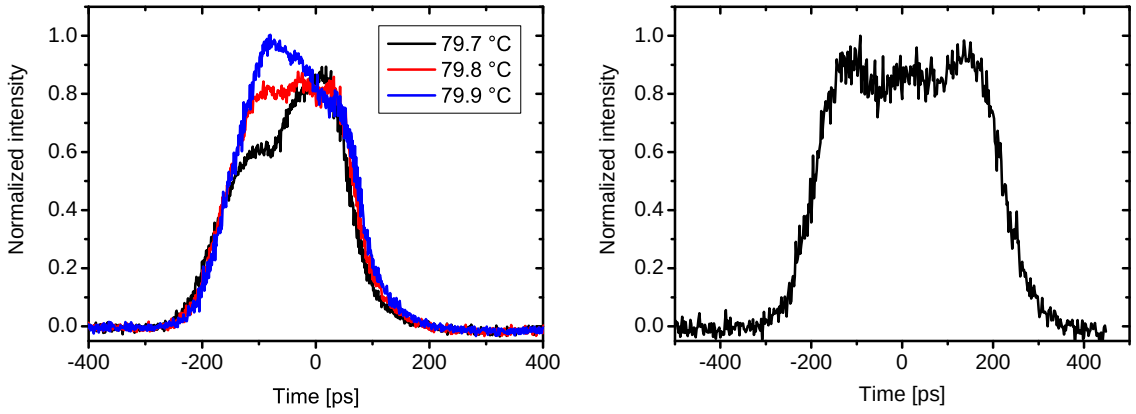

Figure 5.13 – a) Temporal pulse profiles generated with two FBGs: flat-top at 79.8°C (red), slightly lowered leading (black) and trailing edge (blue) at 79.7 °C and 79.9 °C, b) Temporal pulse profile of a flat-top pulse generated with four FBGs at 42.9 °C.

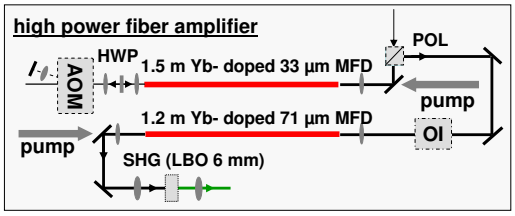

Figure 5.14 – Schematic of the experimental setup of the high energy ns fiber amplifier including the preamplifier in double pass configuration, the main amplifier and a 6 mm long LBO for frequency doubling. (AOM - acousto-optical modulator, HWP - half wave plate, OI - optical isolator)

Pulses with a duration of 235 ps / 416 ps with rising and falling edges shorter than 100 ps have been achieved with the two / four FBG device respectively. In contrast to other pulse shaping techniques the setup is very robust, alignment-free and can be spliced easily to fiber based lasers and amplifiers. The power throughput of the two FBG shaper is measured to be -13.5 dB (5 %), where a loss of -5.5 dB is caused by the circulator and FC-APC connectors used for input and output. By increasing the FBG reflectivity, such a device will have low transmission losses, which are mainly determined by the circulator. Care has to be taken on the post-pulse contrast caused by multiple reflections. If high reflectivity FBGs are employed a trade-off between post-pulse contrast and transmission loss has to be found. Nevertheless, these fiber-based pulse stackers represent an interesting alternative for pulse shaping in nanosecond fiber amplifiers.

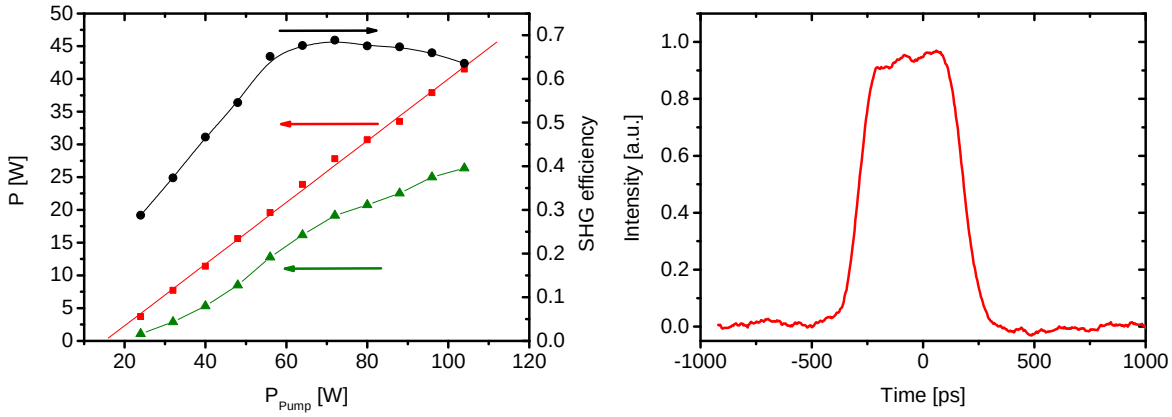

Figure 5.15 – a) Infrared (red) output power of the main amplifier and generated second harmonic power (green) versus launched pump power, and resulting SHG efficiency (black). b) Temporal pulse shape of the amplified infrared pulses at 1 mJ pulse energy.

Performance of the high energy ns fiber amplifier

The spectrally filtered and temporally shaped 460 ps long flat-top like pulses are seeded into in a 1.5 m long double-clad Yb-doped photonic crystal fiber which possesses a mode field diameter of 33 µm. The amplifier is used in a double pass configuration, while a Tellurium Dioxide (TeO_2) acousto-optical modulator (AOM) is used to reduce the repetition rate to 40 kHz after the first pass of the amplifier fiber. The AOM provides a modulation contrast better than 10^{-5}, when operated in double pass. However due to the rise- and fall-time of the modulator the neighboring pulses are suppressed just by 10^{-2}. In the second amplification pass the pulse energy is increased to 5 µJ, which corresponds to an average power of 200 mW. The seed pulses and the amplified pulses are separated by a polarizer located at the input (output) of the fiber amplifier and a half-wave plate is applied to rotate the linear polarization axis after the first amplification pass.

The power amplifier consists of a 1.2 m long Yb-doped rod-type photonic crystal fiber with a mode field diameter of 71 µm, which is presented in sec. 5.3. It delivers up to 41.5 W of average output power, and is pumped by a 976 nm fiber coupled laser diode, imaged into the 200 µm diameter pump core of the rod-type fiber. The maximum pump power coupled to the rod-type fiber is 105 W and the slope efficiency of the main amplifier is as high as 47 %. The amount of amplified spontaneous emission (ASE) is measured to be below 2 % and unwanted pre- and post-pulses amount to another 2 %, hence the pulse energy of the amplified pulses is as large as 1 mJ. It is worth mentioning that even at the highest output power no significant degradation of the polarization contrast is observed. In addition, this amplifier is operated at a B-Integral as high as 25 rad. It has to be stressed that such a high accumulated nonlinear phase leads to severe degradation of the pulse quality in FCPA systems [86, 73, 87]. For example, the presented mJ-FCPA system (sec. 5.3) shows extensive pulse

quality degradation already at a B-Integral of 7 rad. In contrast, self-phase modulation only results in moderate spectral broadening in the amplifier presented herein. Most importantly, the amplified picosecond pulses are not distorted by the nonlinear phase in the temporal domain. The measured spectral bandwidth of the amplified pulses is below 0.2 nm (FWHM), which is acceptable for efficient SHG. When focusing into a 6 mm long LBO crystal, efficient second harmonic generation is observed, resulting in up to 660 µJ pulses at 515 nm wavelength. The corresponding conversion efficiency is as high as 66 %, owing to the uniform temporal pulse profile (see fig. 5.15b), the excellent beam quality of the fiber amplifier, and the small spectral bandwidth. The output characteristics of the fiber amplifier and the generated second harmonic are shown in fig. 5.15a (red and green curve), together with the SHG efficiency (black curve). Measurements with a similar laser system revealed that due to the SHG process both raising and trailing edge of the pulses are steepened [88], while the plateau region of the pulses remains unchanged, leading to a slightly reduced pulse duration for the second harmonic pulses.

Summary

This chapter dealt with fiber based pump lasers for OPCPA. At first an optical synchronization method for signal and pump, which is based on nonlinear frequency shift in photonic crystal fibers, has been presented. Experimental results, as well as numerical studies for two different types of dispersion shifted PCF have been included.

To reach the required pulse energies and pulse peak powers, two different approaches have been discussed for the pump laser. The first approach is to use the well known CPA technique. In that regard, a FCPA system delivering up to 1 mJ pulse energy with sub 1-ps pulse duration is presented. It comprises a large dielectric grating stretcher-, compressor-unit and an ultra-large mode area rod-type PCF to avoid nonlinear distortions.

An alternative is direct amplification of ns-pulses within ultra-large mode area fibers, superseeding a large stretcher and compressor in the pump laser, thus resulting in a more compact and less complex setup. Spectral filtering an pulse stacking generated 460 ps long flat-top like pulses. A high energy ns-amplifier, incorporating a rod-type PCF as gain medium, delivered up to 1 mJ pulse energy which has been efficiently frequency doubled, providing 660 µJ pulse energy as pump for OPCPA.

Both the FCPA system and the ns fiber amplifier fulfill the pump lasers requirements for OPCPA and will be applied as high power pump laser in OPCPA systems.

6 Performance of the developed OPCPA systems and application

The principle setup of an OPCPA laser system has already been presented in the introduction of this thesis (fig. 2.1). Generally, a broadband signal pulse is generated, stretched, parametrically amplified in the nonlinear crystal (OPA) and recompressed to an ultra-short pulse at the end. The pump laser, which drives the parametric process, determines several important parameters of the OPCPA system. It mainly defines the achievable pulse energy and average power of the amplified signal. Furthermore, the stretched pulse duration of the broadband signal has to be about the same as the pulse duration of the pump pulse for efficient energy transfer[1]. Consequently, a ns-pump pulse requires a large stretching ratio of the broadband signal, which can only be achieved by grating stretchers and compressors [89]. Aberrations of the imposed telescope and surface deviations of the applied mirrors limit the pulse contrast of the re-compressed pulses [90, 91]. Hence, this approach is usually not suitable for sub-20 fs pulses.

In contrast, the use of sub-ps pump pulses, as delivered by the presented FCPA system, relaxes the requirements on stretcher and compressor. In this case the stretching ratio is below 100. In consequence, prism pairs [92] as well as broadband chirped mirrors [93] can be applied in combination with material dispersion as stretcher and compressor or vice-versa. Nevertheless, precise dispersion management becomes important for few-cycle pulses due to their enormous spectral bandwidth. Naturally, the pump pulse duration also determines the characteristics of the OPA. As presented in sec. 4.2, the amplification of few-cycle laser pulses normally requires sub-10 ps pump pulses. However, nanosecond pulses are sufficient for parametric amplification of sub-20 fs pulses.

In this chapter the concept, experimental setup and the performance of three different OPCPA systems are presented. The first OPCPA system is operated at degeneracy and uses the frequency doubled mJ-FCPA system as pump laser. The broadband signal is generated via spectral broadening in a step-index fiber. The system emits 29 fs pulses at 1030 nm central wavelength with 2 GW pulse peak power at 30 kHz repetition rate.

Secondly, a compact Gigawatt OPCPA system is presented which incorporates the second harmonic of the ns-fiber amplifier as pump. A broadband Ti:Sa oscillator is seeding both the OPCPA and the ns-fiber amplifier. The system delivers 35 fs pulses with 1 GW pulse peak

[1] In order to avoid gain narrowing effects to the signal spectrum, the stretched signal pulse duration is chosen to be shorter than the pump pulse duration if non flat-top pump pulses are applied.

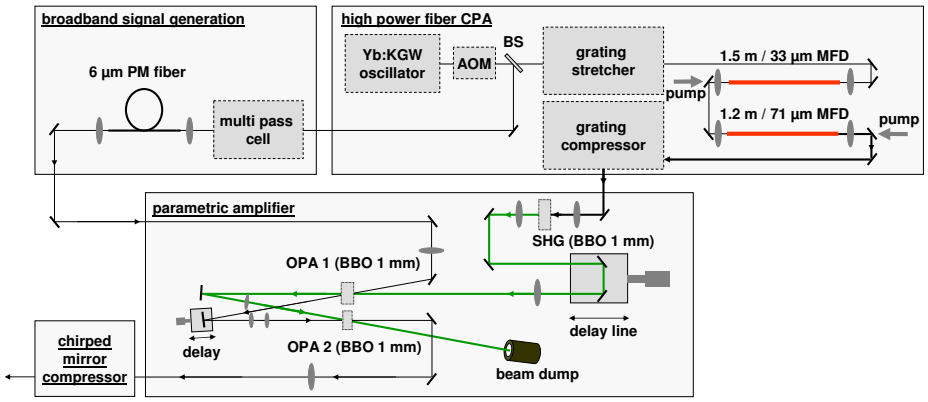

Figure 6.1 – Schematic of the OPCPA system at degeneracy.

power at 800 nm central wavelength and 40 kHz repetition rate.

Finally, a few-cycle OPCPA system is presented. All components of this OPCPA system have been optimized in order to provide the shortest output pulses. An ultra-broadband Ti:Sa oscillator, whose bandwidth supports sub-6 fs pulses, serves as seed for OPCPA and pump laser. In order to provide adequate gain bandwidth, the mJ-FCPA system is used to pump two optimized noncollinear OPA stages. The dispersion of the involved optical elements is compensated up to the 6th order via a liquid crystal spatial light modulator, enabling recompression of the amplified pulses to 8.0 fs pulse duration. The corresponding pulse peak power is as high as 6 GW and represents the highest peak power of any fiber driven laser system. In addition this system is operated at 96 kHz repetition rate and emits an average power as high as 6.7 W, which is a record value for high repetition rate sub-10 fs laser systems.

6.1 Gigawatt peak power OPCPA at degeneracy

In this section a degenerated optical parametric amplifier, operated at ∼1030 nm central wavelength, is presented. The OPA is pumped by the frequency doubled output of the mJ-FCPA system. A schematic of the experiment is shown in fig. 6.1. Both the FCPA and the OPA are seeded by the same Yb:KGW oscillator. Additionally, spectral broadening of the OPCPA seed pulses in a polarization-maintaining step-index fiber provides enough bandwidth for ultra-short pulse generation. Temporal synchronization of signal and pump pulses is achieved by a multipass cell configuration with 45 m optical path length. The broadband signal is amplified in two OPA stages and subsequently recompressed with chirped mirrors .

Broadband signal generation

In order to obtain ultra-short pulses, emphasis is put on the generation of a suitable seed signal for the optical parametric amplifier. Most commonly, a broadband signal for para-

metric amplification is generated by filamentation [94]. Fiber-based spectral broadening [95] which is employed in the presented OPCPA system offers several advantages. An excellent beam profile is inherently given by the use of single mode fibers, the fiber can act as signal stretcher simultaneously and the stretched pulse duration can be controlled by the fiber length. After parametric amplification the pulses are recompressed by means of chirped mirrors. The achievable minimum pulse duration strongly depends on the initial pulse shape which determines the shape of the nonlinear phase. In a first experiment a part of the FCPA output pulses was split and applied for spectral broadening and OPCPA seeding [72]. However, the minimum pulse duration of this OPCPA system was limited to 52 fs. The distorted pulse shape delivered by the FCPA system leads to higher order spectral phase terms on the broadened spectrum, which prevented recompression to shorter pulse durations. In order to achieve the shortest pulses, the output of the Yb:KGW seed oscillator is therefore split to seed both the FCPA and the broadband signal generation stage with clean sech^2 pulses.

To study the process of fiber based spectral broadening in detail, a numerical simulation solving the extended nonlinear Schrödinger equation based on the split-step Fourier method is performed. The simulation includes self-phase modulation (SPM) (n_2=2.8·10^{20} m^2/W), stimulated Raman scattering (SRS) and self-steepening[2] in the fiber as well as group velocity dispersion (GVD) and third order dispersion (TOD) of the fiber ($\beta^{(2)}$=0.025 ps^2/m, $\beta^{(3)}$=6·10^{-5} $\text{ps}s^3$/m). Chirped mirrors providing a constant GVD over a large spectral range will be applied for pulse compression later. Hence, a constant negative GVD is assumed in the simulation. The dispersion of the OPA crystals, lenses, wave plates and polarizers are neglected. For spectral broadening a polarization-maintaining step index fiber with 6 µm core diameter is employed. The pulse parameters of the sech^2 input pulses are 400 fs pulse duration and 40 nJ pulse energy. The results of a the numerical simulation for various fiber lengths are displayed in fig. 6.2a. The simulation reveals the highest effective pulse peak power (34 GW/mJ) and shortest pulse duration of 25.1 fs if a fiber length of 14 cm is chosen. However, in this case a GVD of -5800 fs^2 is needed to recompress the pulses. Experimentally, 58 bounces on suitable chirped mirrors which provide -100 fs^2 per bounce between 980 nm and 1130 nm wavelength would be necessary. For practical reasons, a different configuration is chosen instead. A fiber length of 6 cm already provides enough bandwidth for 35 fs pulses, however requires only a GVD of -3800 fs^2 for recompression. In addition, the pulse duration at the fiber output (∼600 fs) is convenient for parametric amplification later. Furthermore, the generated spectrum ranges from 980 nm to 1060 nm, which allows for the employment of highly dispersive chirped mirrors. These mirrors provide a constant GVD of -250 fs^2 per bounce in a limited spectral range between 1000 nm and 1080 nm, resulting in a compact and high throughput compressor setup.

Fig. 6.2b displays the measured spectrum of a 40 nJ, 400 fs input pulse at the output of

[2]Self-steepening is a higher order nonlinear effect which results from the intensity dependence of the group velocity. As a result, the peak of a pulse moves slower, leading to a steepening of the trailing slope of the pulse [35].

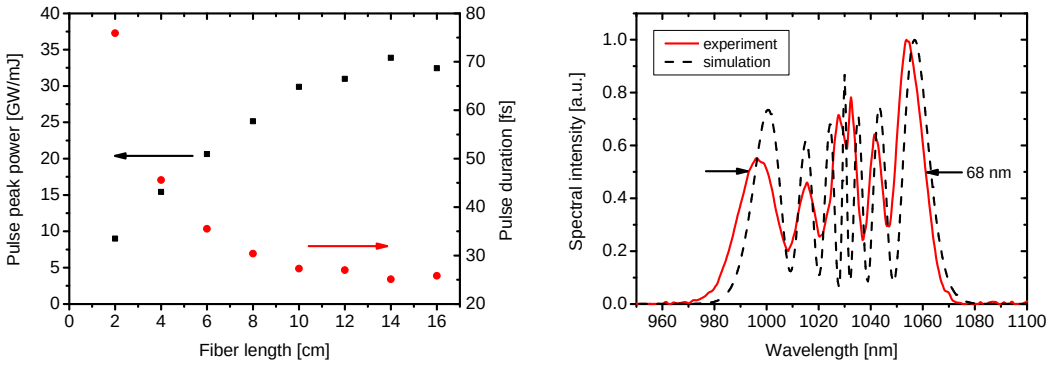

Figure 6.2 – a) Results of a numerical study of spectral broadening in PM-980 fiber and re-compression with chirped mirrors. The peak power and the pulse duration of the re-compressed pulses are shown with respect to the fiber length. b) Spectrum broadened by self-phase modulation in 6 cm of PM-980 fiber with 6 µm core diameter (red) and corresponding numerical simulation (black dots).

a 6 cm long fiber as well as the corresponding numerical simulation, indicating a spectral bandwidth of 68 nm.

To suppress intermediate unamplified pulses at the OPCPA output, the oscillator pulses are split after the repetition rate has already been reduced by an AOM. The pulses which later serve as pump for the OPCPA pass about 45 m of optical path length within the FCPA system. Consequently, the signal pulses need to be delayed according to the optical path of the pump pulses. A multipass cell is used in order to reduce the required space and maintain a reasonable beam size.

Pump laser and second harmonic generation

The already presented mJ-FCPA system is applied as pump laser. For this particular experiment it delivers 1 mJ of compressed pulse energy with a pulse duration of 650 fs. The repetition rate is set to 30 kHz which equals an average infrared power of 30 W. For efficient second harmonic generation a 1 mm BBO crystal is used. The beam size is chosen to 2 mm by means of a Galilean telescope, resulting in $\sim$60 GW/cm^2 of infrared intensity. A conversion efficiency of 55 % could be achieved yielding a pulse energy of 550 µJ at an average power of 16.5 W at 515 nm central wavelength. The corresponding autocorrelation trace of the second harmonic pulses is shown in fig. 6.3. It shows a nearly triangular shape, indicating a close to rectangular pulse shape of the second harmonic pulse which results from saturation of the SHG process. The autocorrelation width is measured to be 700 fs which is equal to the pulse duration of a rectangular pulse shape.

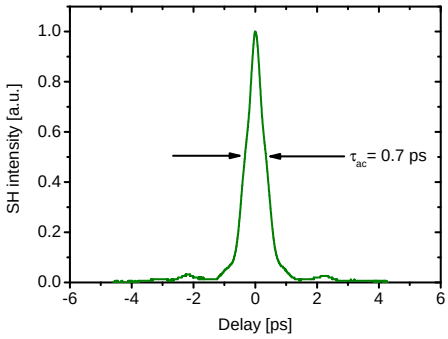

Figure 6.3 – Measured autocorrelation trace of the frequency doubled pump pulses.

Two-stage optical parametric amplifier

The optical parametric amplifier itself consists of two stages. The first amplifier stage comprises a 1 mm long BBO crystal and is pumped by the frequency doubled output of the mJ-FCPA system. A very small noncollinear angle ($\sim 0.5\,^{\circ}$) is introduced between pump and signal, which allows for spatial separation of pump, signal and idler beam after amplification. It is worth mentioning that such a small noncollinear angle does not affect the spectral bandwidth of the OPA significantly. In order to achieve the highest small signal gain, a configuration with perfect phase matching at the central wavelength (1030 nm) is chosen and the calculated gain curve is similar to the curve already shown in fig. 4.3a. The calculated small signal parametric gain is nearly flat, providing variations smaller than 3 % in the used spectral range of 980 nm to 1100 nm.

In order to achieve a high gain in the short crystal length, a Galilean telescope is applied to reduce the pump beam diameter to about 450 µm, resulting in a peak intensity as high as 300 GW/cm^2 which is close to the crystal damage threshold. This first stage is capable of amplifying the seed signal to 60 µJ pulse energy, corresponding to 1.8 W average power, which equals a gain factor of 1500. The calculated small signal gain in the central part of the pump beam is as large as $1.5 \cdot 10^7$. However, this stage is already driven into saturation and the achieved pump to signal conversion efficiency is as large as 11 %. Since the remainder of the pump is used to pump another optical parametric amplifier, the first stage is optimized for a symmetrically depleted pump beam profile. The power amplifier stage consists of another 1 mm BBO crystal. The pump intensity is set to $\sim$30 GW/cm^2, resulting in a small signal gain factor of 75, and the signal beam size is adjusted to be slightly larger than the pump beam size utilizing a telescope. The second stage, also in strong saturation, enables amplification up to 90 µJ of pulse energy which corresponds to 16 % total conversion efficiency from the initial pump to the signal. The far field beam profiles of the seed signal after the spectral broadening fiber, the first amplifier and the second amplifier are shown in fig. 6.4. No significant super-fluorescence has been observed and all amplifier stages have been optimized for best signal beam quality. At this point it is worth mentioning that a measurement of the

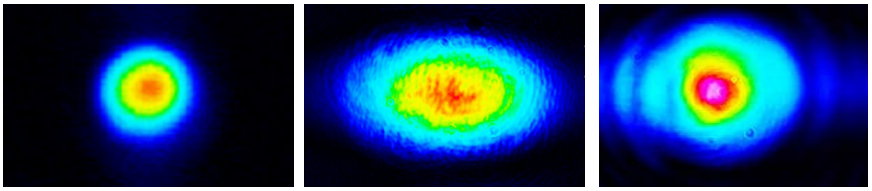

(a) (b) (c)

Figure 6.4 – Far field beam profiles of: a) the signal after spectral broadening in the step index fiber, b) after the first amplification stage and c) after the second amplification stage. The images are taken on different scales.

beam quality (4σ - method) at the output of the OPCPA system results in remarkable M^2 values of M_x^2=1.79 and M_y^2=1.77.

Characterization of the output pulses

The measured spectra of the broadband signal prior amplification (black), after the pre-amplifier (red) and at the output of the power amplifier (blue) are displayed in fig. 6.5a. Due to the saturated amplification regime and large amplification bandwidth the spectral bandwidth is increased to 74 nm. Furthermore, the modulations on the signal spectrum are reduced due to the saturated amplifiers. After collimation of the output beam, the pulses are compressed by a sequence of chirped mirrors. Applying a GVD of $-3600\,\mathrm{fs}^2$ results in pulses with an autocorrelation width of 42 fs (see fig. 6.5b). A deconvolution factor of 1.45 is found by stretching the Fourier transform of the measured spectrum to the measured autocorrelation width by third order dispersion (blue curve fig. 6.5b). Both autocorrelation curves agree very well, and the resulting pulse duration is 29 fs which is only slightly above the Fourier limit of 27 fs (red dotted curve). The compressor throughput is measured to be 90 % yielding a pulse energy of 81 µJ. Based on the numerical simulation, a pulse peak power of 2 GW is estimated with a Strehl ratio of 0.78.

Summary

In summary, the presented system delivers 29 fs pulses with 81 µJ pulse energy and 2 GW pulse peak power at ∼1030 nm central wavelength and 2.7 W average power. This has been achieved by a two-stage OPCPA operated at degeneracy and pumped by the second harmonic the mJ-FCPA system. The broadband signal has been generated in a short piece of step-index fiber. A chirped mirror compressor enabled recompression to nearly the Fourier limit with a high throughput. The beam quality factor M^2 has been measured to M_x^2=1.79 and M_y^2=1.77, ensuring good focusing properties for high-field applications. Unfortunately, the pulse duration of this system is limited by the spectral broadening and recompression process.

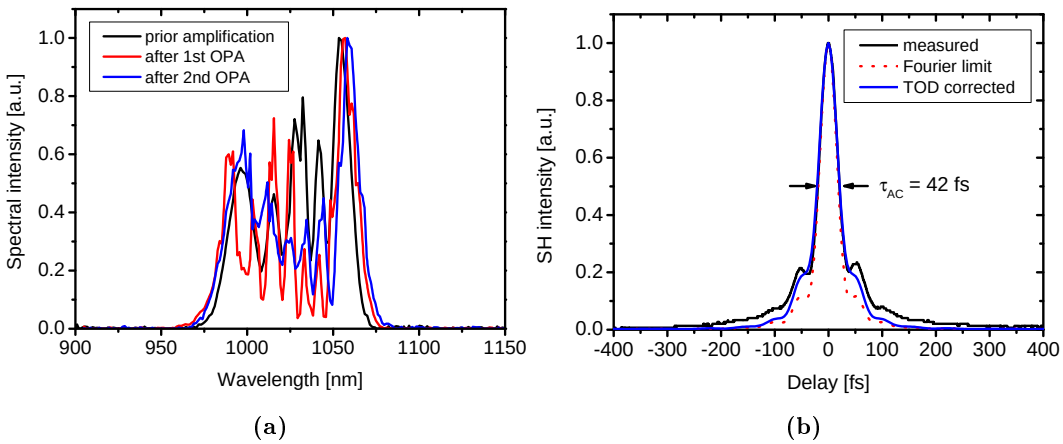

Figure 6.5 – a) Spectra of the signal prior to amplification (black) after the first amplifier (red) and after the second amplifier (blue). b) Measured autocorrelation trace of the compressed output pulses (black). For comparison the Fourier transform of measured spectrum is plotted assuming flat-spectral phase (red dots) and corrected by 3rd order dispersion (blue).

In order to achieve even shorter pulse durations more sophisticated compensation of the spectral phase and high order dispersion would be required. An alternative is to generate the broadband signal directly with a Ti:Sa oscillator, with the potential of shorter pulse durations and a clean pulse shape, which will be applied in the following OPCPA systems.

6.2 Compact Gigawatt OPCPA

The aim of the development of this laser system was to achieve Gigawatt peak power ultrashort pulses at high repetition rate with a more compact experimental setup. Consequently, the ns-fiber amplifier is applied as pump, replacing the large and complex FCPA system. An overview of the experimental setup of the OPCPA system is given in fig. 6.6. The ns-pump laser has already been introduced in sec. 5.4 and consists of a preamplifier section, including spectral filtering, a pulse shaper to generate flat-top like pump pulses, the power amplifier and a SHG stage. Both the OPCPA and the pump laser (via wavelength shift in 1m long PCF NL-3.7-975 as presented in sec. 5.2) are seeded by a cavity-dumped Ti:Sa oscillator, emitting about 100 nm spectral bandwidth (FWHM) at 780 nm central wavelength. The pump laser is seeded by the full repetition rate pulse train emerging at the output coupler of the oscillator. The broadband signal pulses are coupled out of the cavity at 40 kHz repetition rate via an acousto-optical modulator so that no unamplified intermediate pulses are present at the OPCPA output. The signal pulses are stretched by a grating stretcher and the parametrically amplified in two OPA stages applying BBO crystals. The pulse compressor consists of two dielectric transmission gratings which provide high diffraction efficiency and high power capability.

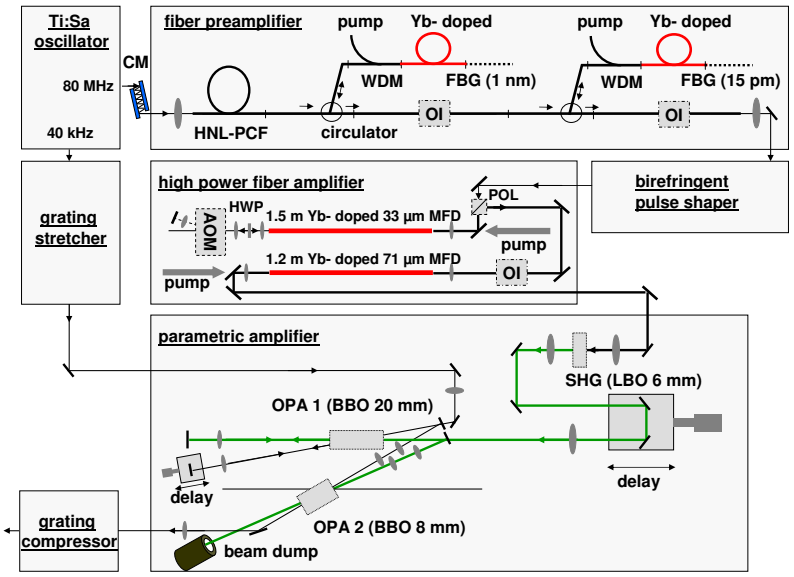

Figure 6.6 – Overview of the experimental setup. The setup is divided into its main parts: the Ti:Sapphire oscillator, the fiber pre- amplifier including spectral filtering, the birefringent pulse shaper for flat-top pulse generation, the high power fiber amplifier, the parametric amplifier section, including second harmonic generation (SHG) and two optical parametric amplifiers (OPA), and the grating stretcher and grating compressor.

Grating stretcher

The signal pulses are stretched to match the pump pulse duration prior to parametric amplification. For this purpose a compact Martinez-type [96] grating stretcher has been developed. It is based on a highly efficient dielectric transmission grating with 700 nm period used under Littrow angle. The material dispersion of the 5 mm thick fused silica substrate can be compensated easily at least in the 2nd and 3rd order by the compressor, and is therefore negligible even for sub-20 fs pulses. The stretcher provides low aberrations, e.g. no noticeable spatial chirp, and a stretched pulse duration of 400 ps for 90 nm transmitted bandwidth. The spectral bandwidth of the OPCPA system is determined by the transmission bandwidth of the stretcher which is chosen to range from 720 nm to 870 nm, with regard to a compact size of the incorporated mirrors. Consequently, the stretcher fits on a 20 cm x 60 cm board and it's transmission bandwidth supports pulses as short as 15 fs, assuming a rectangular spectrum.

Design of the optical parametric amplifier

The frequency doubled pump pulses for the OPCPA have a pulse energy of 660 µJ and a pulse peak power of ∼1.4 MW. Due to the relatively low pump pulse peak power, the single pass gain of the parametric amplifier is limited, as already discussed in sec. 4.1. Table 6.1 summarizes the limits for the small signal gain and the parasitic SHG free wavelength ranges,

Crystal material	BBO		LBO		BIBO	
	PVWC	TPM	PVWC	TPM	PVWC	TPM
SHG free wavelength range [nm]	<860	<1119	758 ... 963	722 ... 1012	660 ... 889	<1025
calculated max. small signal gain	480	38	398	131	$\sim 10^6$	322

Table 6.1 – Summary of the calculated parasitic SHG free wavelength range and the calculated small signal gain for BBO, LBO and BiBO in PVWC and TPM in noncollinear configuration (M^2=1.0).

which have been calculated in chapter 4 for BBO, LBO and BiBO. Within the spectral range of the signal which is defined by the transmission bandwidth of the stretcher, parasitic SHG effects should be avoided. Due to its large nonlinear coefficient, BiBO in PVWC configuration offers the largest small signal gain and it does not suffer from parasitic SHG in the desired wavelength range.

It is worth mentioning that a similar OPCPA system has been operated with BiBO as the nonlinear medium successfully [88]. The system demonstrated broadband amplification around 800 nm central wavelength in BIBO crystals for the first time. However, the output pulses did not possess Gigawatt peak power, and therefore this system will not be presented in the framework of this thesis. Moreover, scaling of this OPCPA system to higher average output powers has been prevented by BiBO as nonlinear material. When pumped at 515 nm, two photon absorption and photo-induced damages occur, which make these crystals unsuitable for high power operation [97]. Gain reduction, beam distortions and reduced damage threshold have been observed experimentally, with BiBO as nonlinear medium in the presented system.

For this reason, BBO is chosen as nonlinear material although the single pass gain is low compared to BiBO. The angle between the wave vectors of signal and pump is chosen to be 2.6 ° inside the crystal in order to provide broadband phase matching. In PVWC geometry parasitic SHG of the signal is observed and therefore the TPM geometry is applied, revealing a calculated small signal gain of 38. Experimentally, a single pass gain of 50 is measured for a pump pulse peak power of 1.4 MW. In consequence, the first parametric amplifier (20 mm long BBO) is used in double pass configuration to achieve sufficient gain. A second stage is used as low gain single pass amplifier. The experimental setup of this two stage parametric amplifier is included in fig. 6.6.

When a pump intensity of 1.3 GW/cm^2 is applied, the 4.4 nJ stretched signal pulses are amplified to 11 µJ in the first stage, and the corresponding gain factor is 2500. The second amplifier is an 8 mm long BBO crystal operated at 2.1 GW/cm^2 pump intensity. Due to the TPM geometry, the walk-off length in this amplifier is only 3.1 mm. A numerical simulation, assuming Gaussian beam profiles for signal and pump, revealed a signal energy of 76 µJ at

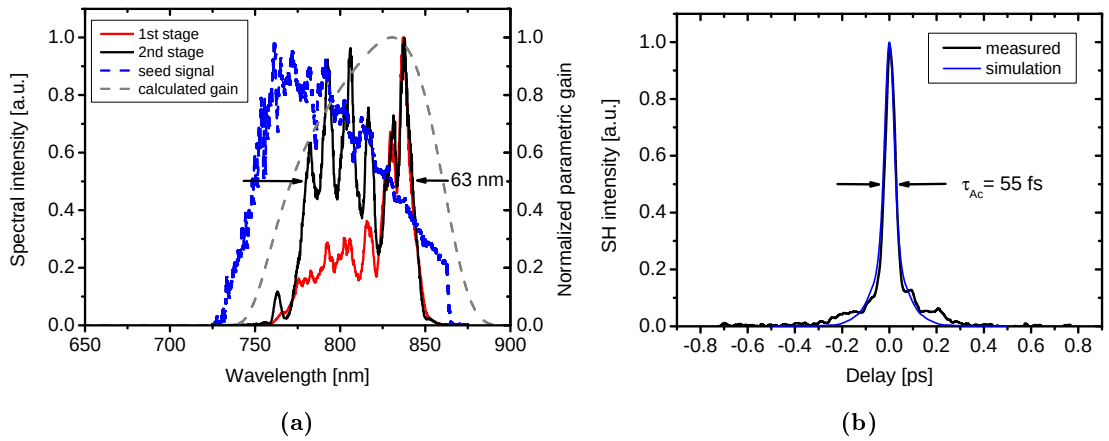

(a) (b)

Figure 6.7 – a) Measured amplified spectra with one (red) and both (black) OPAs pumped. Blue dashed: Seed spectrum, grey dashed: calculated OPA gain curve for 20 mm BBO crystal. b) Measured Autocorrelation trace (black), and 4th order Dispersion corrected Fourier transform of the measured spectrum (blue).

the output when the crystal length is set to the walk-off length. In the experiment the pulse energy is boosted to 72 µJ which corresponds to an overall pump to signal conversion efficiency of 11 %. Note that in each OPA stage the signal beam diameters in the nonlinear crystals have been chosen to be slightly larger than the pump diameters in order to compensate for spatial gain narrowing effects which occur during each amplification pass. The calculated gain spectrum for a 20 mm long BBO used in this configuration is shown in fig. 6.7a (grey dashed) together with the measured seed spectrum (blue dashed) and the amplified spectra for only the first OPA pumped (red) and both OPAs pumped (black). The amplified spectral bandwidth is 63 nm (FWHM) which corresponds to a Fourier-limited pulse duration of 22 fs.

Grating compressor

For recompression, the amplified pulses are sent through a grating compressor which consists of the same type of dielectric transmission gratings which have been already used in the stretcher. A compressor throughput as large as 74 % is measured, including reflection losses at a silver coated roof mirror, resulting in 53 µJ energy of the compressed pulses. In contrast to gold-coated reflection gratings, these dielectric gratings provide negligible absorption and therefore high average power capability. The incident angles and the grating distance are optimized for compensation of 2nd and 3rd order dispersion to achieve the minimum compressed pulse duration. The measured autocorrelation trace is shown in Fig. 5 b) (black). For comparison a Fourier transform of the measured spectrum is shown (blue). It is corrected by 4th order dispersion to the same autocorrelation width. Both curves agree well, despite small pre- or post- pulses which are present in the measured trace and caused by higher order phase distortions. The corresponding pulse duration is 35 fs. The assumption of 90 % peak

power of the corresponding numerical result leads to a pulse peak power as high as 1.1 GW for the recompressed pulses and a Strehl ratio of 0.52.

Summary

In summary, the presented OPCPA system delivers 35 fs pulses with 53 µJ pulse energy and 1.1 GW pulse peak power. Emphasis has been placed on the average power scalability of the laser system. Highly efficient dielectric transmission gratings are used in the compressor and provide high average power capability and high efficiency. The use of BBO crystals as nonlinear material avoids thermo- optical distortion as well as crystal damage.

In contrast to other fiber driven OPCPA systems, it is pumped by a ns-fiber amplifier. Therefore, this system offers lower complexity and is easier to operate, since no stretcher and compressor is needed for the pump laser. Naturally, the signal stretcher (150 nm / 660 ps hard-cut) is very compact in comparison to the stretcher unit of the FCPA system, leading to a compact experimental setup of the whole system. The current experimental setup fits on a 1.5 m x 2.5 m footprint, with potential for further downsizing. This is comparable with today's Ti:Sa multipass- or regenerative amplifier systems, e.g. a Spectra Physics Spitfire amplifier system.

It is worth mentioning that in the current experimental setup higher-order phase distortions inhibited shorter re-compressed pulses. In this regards, the use of an active phase shaper for the broadband signal could be helpful in order to reduce the compressed pulse duration of the system close to the Fourier limit. If the full gain bandwidth of the parametric amplifier is exploited, potentially sub-20 fs pulses could be delivered by such a laser system which are significantly shorter than typical Ti:Sa laser pulses. If even shorter optical pulses are required, a different approach should be adopted which will be presented in the following section.

6.3 Few - cycle OPCPA

As presented in sec. 4.2, sub-5 fs pulse durations, which corresponds to less than two optical cycles, are supported by an optimized noncollinear OPA. The purpose of the now presented OPCPA system is to make use of this large amplification bandwidth as far as possible. Besides the optimized OPA itself, three key components are needed to achieve these pulse durations. First, a pump laser which provides preferably sub-picosecond pump pulses, thus reducing the required crystal length and the signal stretching factor. The presented FCPA system already fulfills this requirement. Second, accurate dispersion management is required in order to achieve the shortest recompressed pulse durations. For this purpose, in the presented OPCPA system a liquid crystal phase modulator is implemented. Third, a source of ultra-short few-cycle pulses is required to seed the OPCPA. The experimental setup of the laser system is shown in fig. 6.8. Each grey box represents a sub-part of the system. Starting

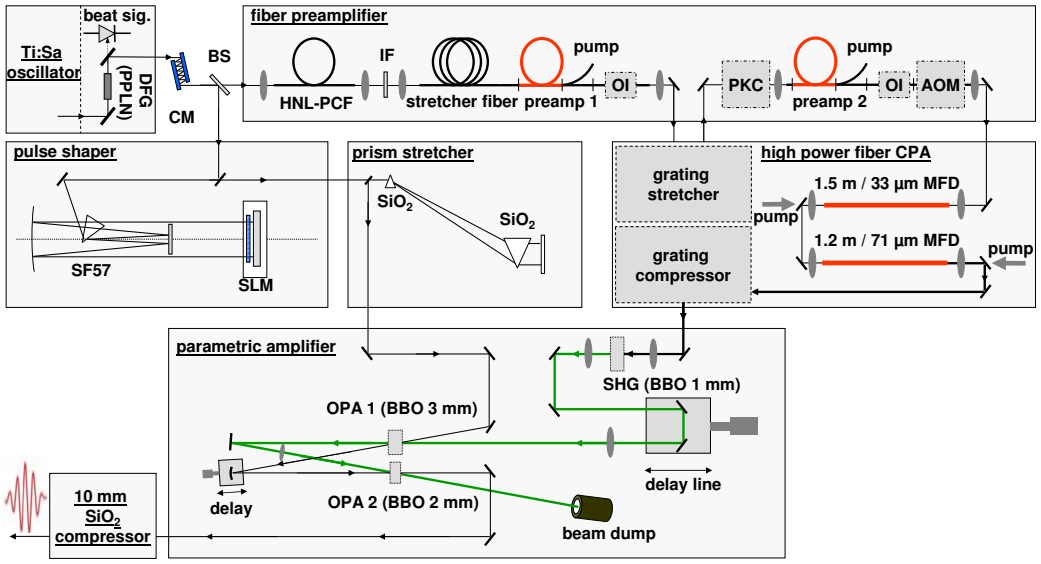

Figure 6.8 – Schematic experimental setup of the few-cycle OPCPA system including Ti:Sa oscillator, DFG- difference frequency generator , CM- chirped mirror, BS- beam splitter, HNL-PCF- highly nonlinear photonic crystal fiber, IF-interference filter, stretcher fiber, two fiber pre-amplifiers, high power fiber CPA system, SHG- second harmonic generation, pulse shaper based on SLM- spatial light modulator, prism stretcher, two stage optical parametric amplifier and fused silica bulk compressor (AOM- acousto-optical modulator, PKC- Pockels- cell, OI- optical isolator).

point and source of the few-cycle pulses is a Ti:Sa oscillator (Femtolasers, Rainbow). It delivers ∼2 nJ pulses with ∼300 nm optical bandwidth (-10 dB) at 108 MHz repetition rate and is used to seed the OPCPA as well as the pump laser. In addition, CEP stabilization of the oscillator is feasible by a monolithic stabilization scheme [98].

Pump laser

Soliton self-frequency shift of the oscillator pulses in a 20 cm long photonic crystal fiber (NL-PM 750) generates synchronized seed pulses for the pump laser. A reasonable amount of 5 pJ pulse energy within the Yb-gain region is selected by an interference filter (IF, 1030 nm ± 2.5 nm). A 100 m long fiber stretcher prevents the pulses from nonlinear distortions in the pre-amplifiers. A Pockels-cell (PKC) and an acousto-optical modulator (AOM) are used to reduce the repetition rate to either 48 kHz or 96 kHz in the preamplifier section. The high power FCPA system is applied as power amplifier for the pump pulses, delivering 910 fs pulses with 550 µJ pulse energy. Due to the excellent beam quality (M^2<1.3) and the good pulse contrast (ASE < 1 %, unwanted intermediate pulses < 1 %) efficient frequency doubling is possible in a 1 mm long BBO, resulting in 780 fs long 330 µJ pulses for OPA pumping.

optical element	$\beta^{(2)}$[fs^2]	$\beta^{(3)}$[fs^3]	$\beta^{(4)}$[fs^4]	$\beta^{(5)}$[fs^5]	$\beta^{(6)}$[fs^6]
12 mm SF57	2683	1694	592	1049	193
SiO2 prim pair	-3623	-487	-6598	7600	-30000
5 mm BBO	374	252	-43	243	-393
15.6 m air	336	143	0	0	0
2 mm PPLN	662	302	-72	125	-240
chirped mirrors	-600	0	0	0	0
10 mm SiO2	363	274	-121	405	-745
residual	195	2178	-6242	9422	-31185

Table 6.2 – Dispersion of the involved optical components in the OPCPA setup calculated from Sellmeier equations [99, 100, 101].

Dispersion management

In order to generate the beat signal for CEP stabilization of the oscillator, a 2 mm long PPLN[3] crystal is inserted for spectral broadening due to SPM and difference frequency generation (DFG) at the oscillator output [98]. Its group velocity dispersion is mainly compensated via 12 bounces on an ultra-broadband chirped mirror pair (CM, $-50\,\mathrm{fs}^2$ / bounce). For efficient parametric amplification, the broadband pulses have to be stretched to $\sim$500 fs duration and recompressed afterwards. Precise control of the spectral phase, which is necessary to achieve few-cycle pulse durations, is provided by a prism (SF57) based phase shaper. It utilizes a 640 pixel single-mask spatial light modulator (SLM), which is placed in the Fourier-plane of a 4-f zero-dispersion stretcher. A fused silica Brewster-prism stretcher is applied to compensate for the material dispersion of the SF57 prism and chirp the pulses negatively prior to optical parametric amplification. In consequence, a simple bulk compressor (10 mm long fused silica block) can be employed as final pulse compressor with high throughput (measured 95 %). Table 6.2 shows the calculated dispersion at 800 nm central wavelength for every optical element within the setup up to the 6th order. The last row contains the residual dispersion which is corrected by the phase shaper.

Optical parametric amplifier

The optical parametric amplifier consists of two amplification stages, incorporating BBO as nonlinear material. Both stages are operated at $\sim$100 GW/cm^2 pump intensity, which allows for very short crystal lengths. A first high gain stage, consisting of a 3 mm long BBO, provides a gain factor of $\sim 5 \cdot 10^4$ and amplifies the signal up to 25 µJ pulse energy. This agrees well with the calculated gain ($\sim 6 \cdot 10^4$) when assuming Gaussian beams. A 2 mm long BBO crystal, driven by the remainder of the pump, is used to achieve high conversion efficiency in a second amplification stage. Indeed, the pulse energy is increased to 74 µJ which corresponds to a gain factor of ~ 3, and the total pump to signal conversion efficiency is as

[3] Periodically poled lithium niobate ($LiNbO_3$)

high as 22 %. In order to achieve good beam quality, careful mode matching of pump and signal in the crystals is carried out. The diameter of the signal beam is chosen to be 20 % larger than the pump which partly compensates spatial gain narrowing within the OPA (see sec. 4.3). The achieved gain and conversion efficiency compares well with the corresponding numerical result. A gain factor of 3.2 and 80 µJ signal pulse energy is predicted if Gaussian beams are assumed and the signal beam is chosen to be 20 % larger than the pump beam, such as in the experimental setup. In order to avoid parasitic SHG of the signal pulses, the TPM matching scheme is applied. The amount of parasitic signal SHG is measured to be smaller than 1 %. The noncollinear angle is chosen to be 2.3 ° which ensures a smooth gain curve matched to the seed spectrum of the Ti:Sa oscillator (see sec. 4.2.3).

Laser system performance

The achieved output power of the two stage OPA (measured after the compressor) is plotted versus the incident pump power in fig. 6.9a. For pump powers below 10 W and exponential increase of the OPA gain is observed due to negligible pump depletion (<5 %). At higher pump power pump depletion and saturation effects occur. The maximum output power is as high as 6.7 W with a corresponding pulse energy of 70 µJ. Figure 6.9b shows the normalized amplified spectra measured after the first and second OPA. The amplified spectrum covers a bandwidth (-10 dB) as large as 320 nm. The Fourier limit of the measured spectrum is 5.6 fs pulse duration, which would result in 10.2 GW peak power. The spectral modulations are caused by the oscillator, the PPLN for SPM and DFG, spectral clipping in the prism compressor and phase jumps at the SLM due to wrapping of the spectral phase curve. Therefore, SPIDER[4] measurements of the output pulses are strongly disturbed, hence not successful. Thus, characterization of the temporal pulse profile is performed with an interferometric autocorrelator supporting 5 fs pulse durations. The measured autocorrelation trace is presented in fig. 6.10a and indicates a pulse duration of 8.0 fs. It is worth mentioning that measurements with this autocorrelator agreed well with SPIDER reconstructions in a previous OPCPA experiment, employing only one OPA stage and lower pulse energy (20 µJ) [104]. A larger scan range autocorrelation measurement indicates no significant pulse content outside the plotted ± 75 fs window. Experimentally, pulse compression is performed by compensating the calculated residual dispersion (tab. 6.2) up to the 6th order with the phase shaper. Additional fine-tuning of the second and third order dispersion is applied to achieve the shortest pulse duration. Consequently, for comparison the Fourier transform of the measured spectrum is stretched with 4th order dispersion to 8.0 fs pulse duration. This corresponds to 6.5 GW peak power and a Strehl ratio of 0.64. Please note that more than 80 % of the pulse energy is found within a ±10 fs wide temporal window containing only the main pulse. In consequence, a pulse peak power >6 GW can be assumed. This value is

[4] Spectral Phase Interferometry for Direct Electric-field Reconstruction (SPIDER) is a method for characterization of ultra short laser pulses. More details on this method can be found in [102] and [103].

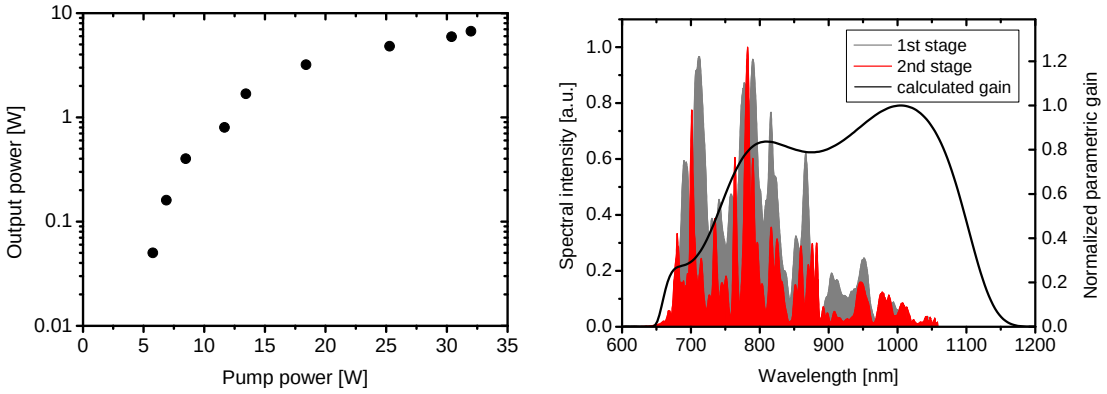

Figure 6.9 – Fig. 2. a) Compressed output power of the OPCPA versus incident pump power b) Measured amplified spectra with one (grey) and both (red) OPAs pumped. The calculated gain curve for a 3 mm BBO crystal in optimized geometry ($\alpha = 2.3\,^{\circ}$, $\theta = 24.15^{\circ}$) is shown as black line.

validated by a HHG experiment which will be presented in chapter 6.4 of this thesis. The amount of super-fluorescence is measured to be <15 mW (<20 mW) for the first (second) OPA when the seed is blocked. Significant reduction of the fluorescence level is expected and numerically predicted for the seeded OPA [105]. The far field beam profile at the OPCPA output is shown in fig. 6.10b together with the intensity profile at the focus of a f=200 mm curved mirror (inset). The focal spot is slightly elliptic (69 µm x 91 µm, $1/e^2$ diameter), due to a small deviation from the optical axis of the curved mirror, which could be avoided in future by employing an off-axis parabolic mirror.

CEP stability

The full advantage of few-cycle lasers can only be exploited when stabilizing the carrier-envelope phase offset (CEP) [10] which allows the control of the electric field of the laser pulse. For this purpose, a DFG beat signal is generated in a PPLN crystal, located at the oscillator output [98]. The CEP beat note with a signal-to-noise ratio of 32 dB in a 100-kHz resolution bandwidth was observed by a spectrum analyzer. The CEP of the oscillator pulses is stabilized with Menlo Systems XPS800 stabilization electronics, driving an AOM which is modulating the pump power of the oscillator. In addition, fused silica wedges inside the cavity are electronically controlled to ensure long term CEP stability. The stabilization electronics are operated at one fifth of the laser repetition rate, meaning every 5th pulse at the oscillator output has the same CEP. In consequence, the pump laser repetition rate is chosen to amplify only pulses with the same CEP in the OPCPA system. The optical parametric amplifier itself preserves the CEP stability [8, 106] of the amplified signal, because phase drifts of the pump are transferred to the idler (see sec. 3.3.3).

For experimental investigation of the CEP stability of the OPCPA output pulses, their

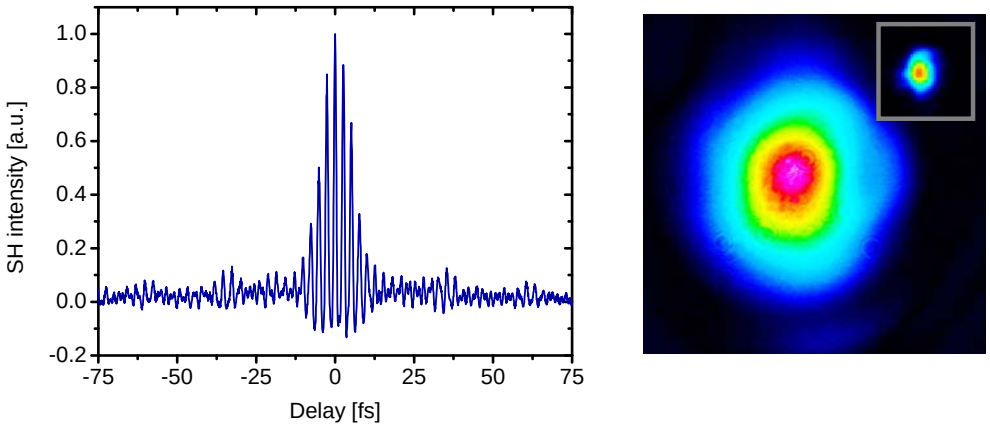

Figure 6.10 – a) Measured interferometric autocorrelation trace revealing 8.0 fs pulse duration. b) Far field intensity profile of the OPCPA output beam, inset: Intensity profile in the focus of a f=200 mm curved mirror.

CEP is measured with an f-2f interferometer (Menlo Systems APS800) incorporating white light generation in sapphire and frequency doubling in a thin BBO crystal. The spectral interference pattern is observed with a fast CCD spectrometer and displayed in fig. 6.11a. For the CEP measurements presented here, the laser is operated at 48 kHz repetition rate, which has been chosen for extremely stable long term operation of the laser system. The spectrometer acquisition time is 21 µs, so each measurement point contains two laser pulses. Fig. 6.11b shows the CEP over a measurement time of 1.0 s. Due to the limited spectrometer readout speed and the Fourier transform algorithm, which is used for CEP analysis, the update rate of this measurement is only 60 Hz. A standard deviation of 0.47 rad is observed, which is satisfying, keeping in mind that the laser system emits about 50'000 laser pulses within this period. It has to be stressed that the laser is operated in a rough environment with plenty of acoustical and vibrational noise sources as well as turbulent air flow caused by the air conditioning system. Under these circumstances, the obtained results can be seen as a proof of principle measurement. Certainly, CEP stable operation over a longer time scale would require a slow feedback loop, additional CEP servos such as movable fused silica wedges, and isolation of the entire laser systems from any mechanical and thermal noise sources. It is worth mentioning that due to the low stretching ratio, the CEP of the output pulses of the presented system is less sensitive to beam pointing fluctuations within the stretcher compared to other CEP stable few-cycle OPCPA systems [106].

Summary

The presented high power few-cycle OPCPA system delivers 8.0 fs pulses at 96 kHz repetition rate. The corresponding average power is as high as 6.7 W which is the highest average output

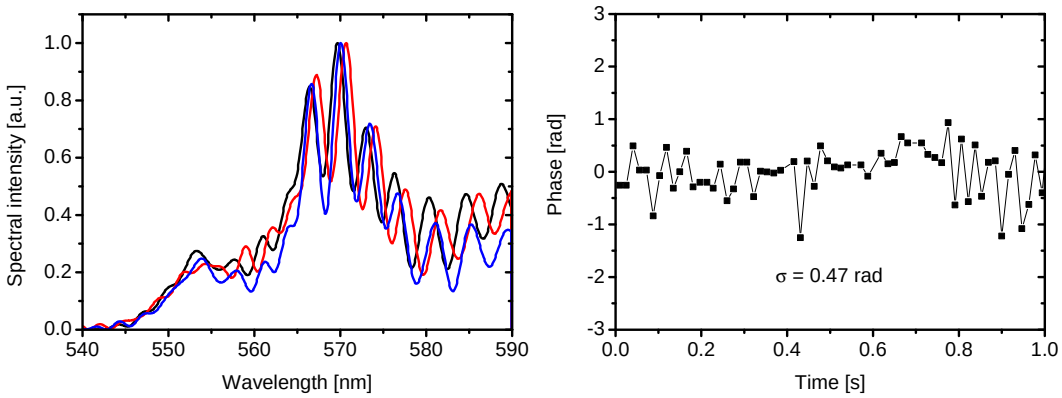

(a) (b)

Figure 6.11 – Three successive f-2f interference patterns observed with the spectrometer (spectrometer acquisition time: 21 µs - containing 2 laser pulses), b) CEP measurement over a short measurement time of 1.0 s.

power reported for a few-cycle laser so far. These outstanding laser parameters have been enabled the high power pump laser as well as by the high conversion efficiency achieved in both SHG and OPA stage. In particular, a pump- to signal conversion efficiency as large as 22 % has been achieved with a carefully optimized two stage OPA scheme. Additionally, a bulk compressor allows for a throughput as high as 95%, yielding 70 µJ compressed pulse energy. The resulting pulse peak power is more than 6 GW which is the highest value ever reported for a fiber driven laser system. This record performance is also achieved by optimization of the whole setup for an ultra-large spectral bandwidth, including the oscillator, the optical parametric amplifier and the dispersion management. In addition, the CEP of the amplified pulses is characterized. When stabilizing only the oscillator, the best CEP standard deviation measured is 0.47 rad over a short period of time.

Due to the short pulse duration and the high peak power, this laser system is an ideal source for high field physics e.g. efficient generation of high order harmonics which will be in focus of the next section.

6.4 High field physics application: High harmonic generation in Krypton

High harmonic generation of infrared laser light enabled table-top sources of spatially and temporally coherent radiation in the extreme ultraviolet (XUV) as an alternative to large scale facilities. The outstanding properties of the generated radiation paved the way for numerous applications, such as the study of molecular motion [5], new high resolution XUV imaging techniques [107], investigation of surface processes [7] and attosecond physics [10]. A major drawback of high harmonic generation, so far, is the small number of generated

photons per second (average power) due to low conversion efficiency (typically lower than 10^{-6}) [108]. However, there is a growing interest in high repetition rate laser sources for use in high harmonic generation, e.g. for XUV spectroscopy [109] or seeding of free electron lasers [12]. Furthermore, plenty of already existing applications of HHG radiation will benefit from a higher signal to noise ratio and shorter detection times, if a higher XUV average power would be available. The presented OPCPA laser systems, and especially the few-cycle OPCPA system, provide sufficient peak power for efficient HHG at a very high laser repetition rate.

This section therefore is focused on the application of the few-cycle OPCPA system for HHG in a noble gas. At first, the physical background is briefly introduced. Then the experimental setup and the results are presented. Finally, the results are compared with experimental results of direct HHG of the FCPA output pulses and conclusions and scaling considerations are given.

6.4.1 High harmonic generation - single atom response

A typical spectrum of generated high order harmonics shows emission at odd multiples of the driving laser frequency. The conversion efficiency is observed to decrease rapidly for the first few harmonic orders, then remains nearly constant in the so called plateau region, and sharply decreases at a specific photon energy named the cut-off energy. These observations required a new description of the response of atoms on intense optical fields. A semi-classical model has been developed by Corkum [110]. It describes the main characteristics of HHG and has been expanded to a semi-analytical, quantum mechanical description by Lewenstein later [111]. To illustrate the basic physics of the three steps of HHG, the semi-classical view is sufficient and therefore introduced in the following section. The model outlines three basic steps of HHG which are illustrated in fig. 6.12:

1. Tunneling ionization of the atom through a suppressed Coulomb barrier: The coulomb potential of the atom is strongly distorted by the electric field, lowering the potential barrier. In consequence, the electron may tunnel through this barrier with a certain probability. Tunnel ionization is the relevant process for HHG and becomes dominant at intensities of the order of 10^{14} $\mathrm{W}/c m^2$ for typical noble gases and near infrared driving lasers. Ionization rates for the tunneling regime can be described by the so called ADK model [112]. The fraction of ionized atoms is especially important to estimate the phase mismatch of fundamental and harmonic light, which will be discussed in more detail later.

2. The free electron is accelerated by the electrical field of the laser light. When the electric field changes its sign, the electron is accelerated towards the parent ion.

3. There is a certain probability of recombination with the parent ion. This recombination is accompanied by emission of an EUV or soft X-ray photon.

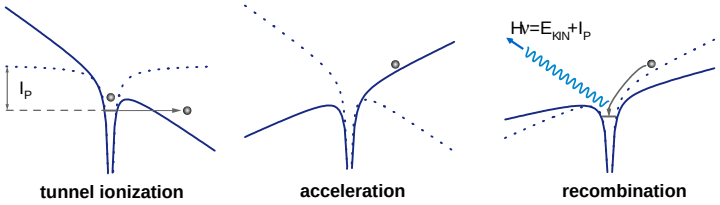

Figure 6.12 – Illustration of the three step model: The atom is irradiated by the intense laser field and ionized. The free electron is accelerated in the electrical field and can make a transition back to the initial state linked with the emission of an XUV or soft x-ray photon.

The kinetic energy of the electron is typically given in units of U_p, which is the ponderomotive energy and represents the time-average of the kinetic energy obtained by an electron in the oscillating electric field. It is calculated as

$$U_p = \frac{e^2 E^2}{4m\omega^2} = \frac{e^2 I}{2m\epsilon_0 c_0 \omega^2}, \tag{6.1}$$

where e and m are the charge and the mass of the electron while ω is the angular frequency and E is the electric field strength of the incident laser field, ϵ_0 is the vacuum permittivity and c_0 is the vacuum speed of light. In the semi-classical model, the freed electron is assumed to have zero velocity after ionization. It is then purely driven by the electric field of the laser. As a result, the specific path of the electron depends on the phase of the driving laser field at the time of ionization $\varphi_0{=}\omega t_0$. Consequently, the kinematic energy of the electron at the return to its parent ion is also dependent on the phase φ_0. The maximum kinematic energy of $3.17{\cdot}U_p$ is found for $\varphi_0{\simeq}0.09\pi$. Lower photon energies can be achieved for smaller and higher phase φ_0 resulting in long and short trajectories, respectively. The recombination of the electron to its ground state leads to the emission of a photon with an energy equal to the sum of ionization potential I_p and kinetic energy of the electron and the cut-off photon energy is given by

$$\hbar\omega_c = I_p + 3.17U_p. \tag{6.2}$$

Interestingly, extension of the cut-off energy may be obtained by increasing the intensity. However, increased intensity may lead to strong ionization of the gas medium which disturbs the coherent buildup of the HHG radiation due to dephasing.

6.4.2 Phase matching

Just as described for $\chi^{(2)}$ processes in chapter 3, efficient conversion from the fundamental light to the high order harmonics requires phase matching to ensure coherent build up of the harmonic wave. For generation of the q^{th} harmonic, phase mismatch is calculated as $\Delta k = qk_0 - k_q$, where k_0 is the wave vector of the fundamental light and k_q is the wave vector of the q^{th} harmonic. For HHG in a focused geometry several phase therms have to

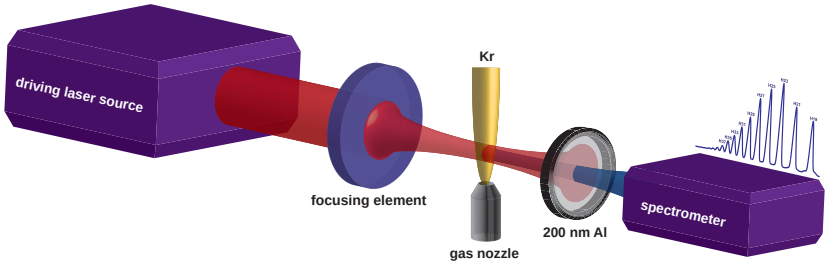

Figure 6.13 – Schematic of the experimental setup for high harmonic generation. The driving laser sources is focused with a focusing element (lens or mirror) onto a Krypton gas jet. The fundamental light is blocked by a 200 nm thick aluminum filter and spectral analysis is performed by an XUV spectrometer [114].

be considered originating from neutral gas dispersion, plasma dispersion (free electrons) and the Gouy shift. By balancing the various phase mismatch terms, phase matching can be achieved [113]. Note that for high intensities phase matching is limited mainly by ionization. If the ionization fraction is higher than a critical value, the electron density will cause a phase mismatch that cannot be compensated for. For long laser pulses the critical ionization level is typically achieved before the peak and therefore avoids the phase matched generation of the highest harmonics. In this context, few-cycle laser pulses are advantageous as they possess a minor number of half optical cycles, which lead to ionization before the peak of the laser pulse. The calculated critical fraction of ionization is 7.2 % for Krypton gas [113] which is used in the later presented experiments.

6.4.3 Experimental setup and results

The principle experimental setup for HHG is shown in fig. 6.13. Either a lens or a curved mirror has been employed for focusing onto a gas jet. A 50 µm gas nozzle enables high particle densities in the focal region while keeping the overall gas load to the vacuum system low. A continuous gas flow is needed because of the high laser repetition rates which do not allow for a pulsed gas jet. The high harmonic radiation has been separated from the fundamental by a 200 nm aluminum filter and a grazing incidence monochromator (McPherson Inc., 248/310G) and a channel electron multiplier (Photonics CEM 5900 SL Magnum) are applied for spectral characterization of the generated radiation.

HHG with FCPA

In a first experiment the FCPA system, which typically serves as pump laser for the OPCPA, is used as driving laser source directly. At 50 kHz repetition rate, 800 fs pulses with 400 µJ pulse energy are focused onto a 45 µm diameter spot, resulting in $1.1{\cdot}10^{14}\,\mathrm{W}/cm^2$ peak intensity. The obtained harmonic spectrum is shown in fig. 6.14a. Harmonic orders up to the 35th (29.8 nm) are observed. A main limitation for the generation of shorter wavelengths is ionization due to the long pulse duration. The fraction of ionized medium can be estimated

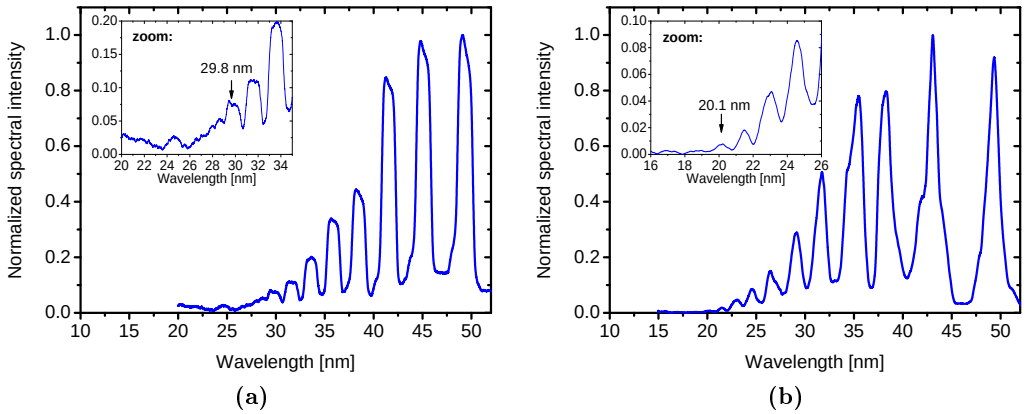

Figure 6.14 – Measured HHG spectra: a) With FCPA system as driving laser, 800 fs pulse duration and 400 µJ pulse energy. b) With few-cycle OPCPA system as driving laser, 8 fs pulse duration and 53 µJ pulse energy.

by calculating ionization rates with the ADK model [112]. The calculated ionization fraction at the pulse peak is already $\eta = 9\,\%$ and, therefore, higher than the critical value. In consequence, only a part of the pulse takes part in phase matched HHG and the peak of the laser pulse is not involved in phase matched HHG. The experiment yields a conversion efficiency between $1.4 \cdot 10^{-11}$ to $1.3 \cdot 10^{-10}$ into the strongest harmonics at 44.8 nm and 49.2 nm [114]. As the system is operated at 50 kHz repetition rate, this already corresponds to an average power of 0.3 to 3 nW ($6 \cdot 10^7$ photons/s - $6 \cdot 10^8$ photons/s).

HHG with OPCPA

In a second experiment the developed few-cycle OPCPA system is applied as driving laser for HHG. For this purpose it is focused by a f=200 mm curved silver mirror to a focal spot measuring 69 µm x 91 µm in diameter. The OPCPA system is operated at 730 nm central wavelength, providing 53 µJ pulse energy, a pulse duration of about 8 fs and a peak power of ~5 GW at the target. The obtained harmonic spectrum is shown in fig. 6.14b. The shortest detected wavelength is 20.1 nm, which corresponds to the 35th harmonic, and represents a significant improvement compared to HHG with the FCPA system directly. Moreover, HHG with the few-cycle laser pulse has been remarkably more efficient due to reduced ionization resulting from the about two orders of magnitude shorter pulse duration. This allows for higher possible peak intensities in the focal region without exceeding the critical fraction of ionization (6 % at the peak of the laser pulse). Part of this enhancement can also be attributed to the single atom response wavelength scaling law. The experimentally achieved conversion efficiency is estimated to be between $2 \cdot 10^{-8}$ and $3 \cdot 10^{-7}$ at the strongest harmonic of 42.9 nm [114]. Considering the input average power of 5 W, this conversion efficiency already belongs to µW level harmonic power with $> 10^{11}$ photon/s.

	FCPA	OPCPA
	Parameters of the Laser system	
Pulse duration	800 fs	8 fs
Pulse energy	400 µJ	53 µJ
Pulse peak power	~ 0.5 GW	~ 6 GW
Central wavelength	1030 nm	730 nm
Repetition rate	50 kHz	96 kHz
	HHG results	
Peak intensity	$1.1{\cdot}10^{14}\mathrm{W}/cm^2$	$>2.4{\cdot}10^{14}\mathrm{W}/cm^2$
cut-off wavelength	29.8 nm (35th harmonic)	20.9 nm (35th harmonic)
conversion efficiency	$1.4 \cdot 10^{-11}$ to $1.3 \cdot 10^{-10}$	$2 \cdot 10^{.8}$ to $3 \cdot 10^{-7}$
average power	0.3 to 3 nW	0.1 to 1.5 µW
photon flux	$6 \cdot 10^{7}$ to $6 \cdot 10^{8}$photons/s	$1.4 \cdot 10^{11}$to $2 \cdot 10^{12}$photon/s

Table 6.3 – Summary of the Laser parameters of FCPA and OPCPA system and the experimental results of HHG in a Krypton gas jet.

6.4.4 Comparison and conclusion

The parameters of both laser systems and the achieved HHG results with Krypton as gas target are summarized in tab. 6.3. The FCPA has been used to either drive HHG directly (400 µJ pulse energy at target / 800 fs) or to pump the few-cycle OPCPA system (550 µJ pulse energy / 910 fs). Although the OPCPA system provides a lower pulse energy, the peak power of the laser pulses is significantly enhanced due to enormously reduced pulse duration.

As a result of the increased peak power and the few-cycle pulse duration, the obtained conversion efficiency of the HHG process is increased by three orders of magnitude. In addition, significantly shorter wavelengths were generated and the average power as well as the photon flux were increased by three orders of magnitude. The achieved wavelength of 20.9 nm represents the shortest wavelength generated so far with a fiber based laser system. The results compare well with HHG of high energy low repetition rate laser [24], waveguide based high harmonic generation [17] or cavity enhancement [13]. The estimated high photon flux has the potential to significantly improve the performance of XUV studies in the future. Nevertheless, prior to any applications, a full characterization of the spatial profile and coherence properties of the generated XUV radiation [115] is required, which is subject of ongoing experiments.

It is also worth to mention that calculation of the peak intensity from the cut-off law (eq. 6.2) reveals a pulse peak power as high as 6.4 GW for the few-cycle laser pulses. This value absolutely confirms the temporal characterization of the pulses, which has been presented in sec. 6.3 of this thesis. Lastly, the generation of isolated attosecond pulses [10] seems feasible with an improved version of the presented laser system, however requires precise CEP stabilization and even shorter pulses.

7 Future prospects and scaling considerations

In a first part of this chapter the scaling properties of the optical parametric amplifier itself are discussed. However, scaling of the optical parametric amplifier is always related to scaling of the pump laser. Consequently, the limitations and scaling possibilities of the fiber based pump lasers are presented in a second part of this chapter. Furthermore, strategies for combining the energy and power of multiple pumps are presented.

7.1 Scaling of the optical parametric amplifier

7.1.1 Pulse duration

OPCPA with sub-ps pump pulses

The shortest pulses, delivered by an OPCPA system presented in this thesis had a pulse duration of 8.0 fs. The numerical results given in sec. 4.2, revealed amplification bandwidths which support sub-5 fs pulses for sub-ps pump pulses. However, recompression of such ultra-broad spectra remains challenging. In principle, the spectral phase of octave-spanning spectra can be controlled by an SLM based phase shaper [116]. However, a precondition for successful phase correction is the exact measurement of the spectral phase which itself is an area of ongoing research [8]. Nevertheless, nearly Fourier-limited sub-5 fs pulses seem feasible with fiber driven OPCPA systems in the future. A further increase in amplification bandwidth can be achieved by more sophisticated techniques such as chirped femtosecond pump pulses [117] or angular dispersion of the pump beam [118]. Such techniques could open the way for single-cycle pulse amplifiers in the future. It this regard, it is worth mentioning that with a noncollinear phase matching and angularly dispersed pump technique, pulses as short as 3.9 fs have been achieved with an OPA at ∼600 nm central wavelength [18].

OPCPA with ns pump pulses

Pulse durations of several nanoseconds can be applied to extract the highest pulse energies from a fiber amplifier. When using nanosecond pulses as OPCPA pump two facts have to be considered. At first, the lower damage threshold intensities require long nonlinear crystals. Hence, the amplification bandwidth is reduced and does not support sub-10 fs pulses, according to calculations in sec. 4.2.1. In addition, due to aberrations in stretcher and

compressor as well as surface deviations of the applied mirrors, a reduced pulse contrast is typically observed for sub-20 fs pulses [90, 91, 119]. Even if an active phase shaper would be included, such OPCPA systems will therefore be limited to pulse durations longer than 10 fs.

7.1.2 Energy and average power scaling

In principle, scaling of the pulse energy of an OPCPA system can be achieved by increasing the beam size and the aperture of the nonlinear crystals. Today, BBO crystals are fabricated up to several centimeters aperture, which would allow to increase the pulse energies of the presented OPCPA systems by two orders of magnitude. Other nonlinear crystals, such as KDP[1] and DKDP[2], can be grown to apertures of 40 cm and more, and allow for tens of Joules of pulse energy in 0.5 PW peak power OPCPA systems [120]. Energy scaling of high repetition rate OPCPA systems is therefore mainly a matter of the pump laser.

In contrast, scaling of the average power may be limited by thermal effects arising form the residual absorption. Although the absorption coefficient is typically low (BBO: $<1\,\%$/cm at 532 nm [52]), absorption of the pump will lead to a temperature gradient within the nonlinear crystal at high average power and consequently generate a phase mismatch distribution in transverse and longitudinal direction. Numerical modeling of a BBO based OPCPA revealed a 10 % drop in conversion efficiency at 700 W average pump power, when assuming 6 mm beam diameter [52]. However, this model did not include stress-optical effects and angular effects arising from thermal lensing. In order to investigate thermal dephasing experimentally, a high power SHG experiment was carried out. A high power fiber laser, delivering 50 µJ, 690 fs pulses was focused into a 0.5 mm long BBO crystal (peak intensity: $\sim$50 GW/cm^2). The incident infrared and the generated second harmonic power were measured for different repetition rates of the laser and the results are plotted in fig. 7.1. A linear increase of the second harmonic power is observed with increased repetition rate and the conversion efficiency remains constant at $55\pm1\,\%$. The highest average power of the second harmonic was measured to be 125 W. Of course, an OPA will suffer from stronger dephasing, because the high power second harmonic beam propagates through the full crystal length, in contrast to SHG where it is generated along the crystal. Nevertheless, this experiment is a proof that today's nonlinear crystals can handle these average power levels and average power scaling is also primary limited by the pump laser. If thermal problems should occur, techniques such as thin slices of nonlinear crystals, amplification in multiple crystals with distributed pump power or crystal surface cooling techniques could relax them.

[1] KDP - Potassium Dihydrogen Phosphate
[2] DKDP- Potassium Dideuterium Phosphate

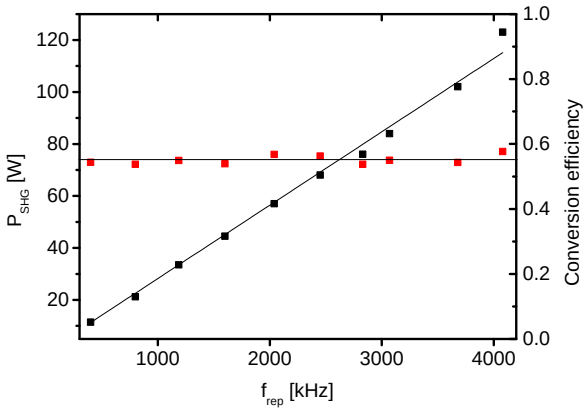

Figure 7.1 – Measured average power of the generated second harmonic (black) and achieved conversion efficiency (red) versus the laser repetition rate.

7.2 Limits of the pump laser and scaling considerations

Having seen that the optical parametric amplifier itself is not limited in pulse energy and average power, this section is now focused on how to further scale fiber based pump lasers for OPCPA. Of course, alternative laser concepts such as inno-slab [121] or thin-disk [122] have to be considered as pump laser for future high power OPCPA systems as well, but are not in focus of this thesis.

7.2.1 Pulse energy scaling in FCPA

Measurements and calculations, which have been presented in chapter 5, already stated that the pulse quality of FCPA systems strongly degrades with increasing pulse energy. This is caused by the nonlinear phase which is imposed onto the stretched pulse, resulting in a spectral phase due to the time / spectrum mapping [86]. The spectral phase is determined by the temporal pulse shape of the chirped pulse, hence the spectral shape. The second order phase can be compensated by the GVD of the compressor, but higher order phase terms remain uncompensated. For high values of the B-Integral the effective pulse peak power is reduced, and satellite pulses arise. In order to avoid this pulse quality degradation several methods can be applied:

1. Temporal scaling: An increased stretched pulse duration reduces the pulse peak power in the amplifier. However, stretching of femtosecond pulses is limited to several nanoseconds by practical reasons, mainly by the required grating size in the stretcher and compressor.

2. Control or compensation of the nonlinear phase: The generation of a parabolic spectrum results in a linear chirp which can be compensated by GVD of the pulse compressor. In a proof of principle experiment this technique has been successfully demonstrated up to a B-Integral of 16, though at low pulse energy ($<1\,\mu J$) [123]. Furthermore, compensation

of the residual nonlinear phase by a phase shaper has been demonstrated [86]. The pulse quality at a B-Integral of 8 has been improved significantly, revealing nearly transform-limited pulses and the pulse peak power has been increased by a factor of two compared to the system without phase shaping. Multiple passes through the pulse shaper and wrapping of the compensated phase function would allow for phase compensation at higher B-Integrals, although the phase deviation of the applied spatial light modulator is limited. Another remaining option is the use of materials with negative n_2, such as semiconductors or cascaded second order nonlinear effects [124], to compensate the nonlinear phase.

3. Spatial scaling: Increasing the mode field diameter remains an option to reduce the B-Integral. The presented 200/85 rod-type fiber already represents a state-of the art ultra-large mode area fiber which is not strictly single mode. Especially in combination with the short fiber lengths, higher order mode suppression is difficult. Fiber designs which combine ultra-large mode areas (>100 µm), low losses for the fundamental mode and high propagation losses for the higher order modes are under development. In this content, the PCF provides multiple degrees of freedom which will be exploit in future.

Figure 7.2 displays the limitations on the output pulse energy versus the mode field diameter for linearly polarized light. Except the varying MFD, a fiber structure similar to the 200/85 rod- type fiber is assumed. The fiber length is set to 1.2 m in order to provide sufficient pump light absorption and small signal gain [73]. The stretched pulse duration has been set to a meaningful value of 2 ns. It can be seen that at a B-integral of 10 rad (green line) a MFD of 100 µm would allow for 2.7 mJ pulse energy to be extracted from the fiber amplifier. At this point, it is worth mentioning that surface damage of the fiber end facet (brown dashed line, calculated according to [76]) can be avoided by core-less fiber end caps which allow the beam to expand before it reaches the surface.

7.2.2 Pulse energy scaling in ns fiber amplifiers

In contrast to FCPA, direct amplification of ns pulses is not limited by the accumulated B-Integral, since the nonlinear phase is imposed onto an unchirped pulse. Spectral broadening due to SPM is normally negligible, e.g. a moderate spectral bandwidth of 0.2 nm has been measured at the output of the presented ns-amplifier. In consequence, a higher pulse energy can be extracted at the same pulse duration compared with a chirped pulse in FCPA. As displayed in fig. 7.2 (blue curve), SRS is not a limiting factor[3] especially for large MFD>70 µm and the extracted energy is ultimately limited by self-focusing and beam collapse (red curve). Unfortunately, mode-shrinking can be already expected well below the critical power of self-focusing, thus reducing the effective damage threshold [64]. This effect is considered in the

[3]The SRS threshold can be roughly estimated [35], however this estimation is only truly valid for cw radiation and exponential gain.

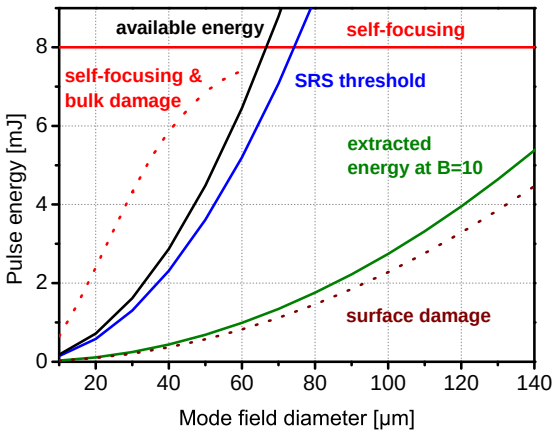

Figure 7.2 – Pulse energy limit for a 2 ns pulse plotted versus the mode field diameter. Basis of the calculations is the 85/200 rod-type fiber with 1.2 m length (Data taken from [126, 73]).

dotted part of the red curve, which displays calculations of the bulk damage threshold at 1064 nm wavelength including self-focusing [64]. For large MFD>70 µm, the bulk damage curve converges with the critical energy of self-focusing (red horizontal line). Nevertheless, record peak powers as high as 4.5 MW have been reported for linear polarized light [74], which coincides with the theoretical limit [125]. In the end, self-focusing is determined by the exact value of the nonlinear refractive index which depends on the fiber composition and is discussed in detail e.g. in Appendix B of [35]. A value of 4 MW is therefore chosen as a reasonable limit yielding a pulse energy limit as high as 8 mJ for 2 ns pulse duration. However, the pulse energy which is stored in a 1 m long 85/200 rod type fiber at the maximum inversion level, assuming 976 nm pump wavelength, is only 8 mJ [73]. Hence, a longer fiber would be required to extract higher pulse energies.

7.2.3 The influence of polarization on the pulse energy limits

The above mentioned limits, such as B-Integral and self-focusing, are due to the nonlinear index of refraction n_2. It is theoretically well known that n_2 is different for circularly polarized light [42]. Theoretically predicted and experimentally measured, it is only 2/3 of the value for linear polarized light [127]. Non-polarization-maintaining fibers exhibit negligible birefringence, and therefore permit amplification of circular polarized light with reduced Kerr nonlinearity. Hence, the B-Integral can be reduced and the self-focusing threshold can be increased by a factor of 1.5, respectively.

7.2.4 Average power scaling

In principle, fiber amplifiers are well suited for high average power, due to their outstanding properties. Recently, a FCPA system emitting 830 W of average power has been reported [25]. This laser incorporated a 8 m long 27 µm MFD fiber, limiting the pulse peak power

to 12 MW. Substitution by a e.g. 85/200 rod-type PCF would be beneficial in terms of reduced nonlinearity, hence a higher pulse peak power could be achieved. However, at an average power level higher than ∼100 W the fiber suffers from a threshold-like onset of mode instabilities. Higher order mode content in combination with transverse spatial hole burning effects [10,11] are possible causes and subject of ongoing research. Future ultra-large mode area fiber designs therefore require high losses for the higher order modes for stable high power operation.

7.2.5 Combining multiple pumps

In principle, multiple pump lasers can be used to drive one OPCPA stage [55]. For this purpose, multiple pump beams can be overlapped in the nonlinear crystal under different angles. In order to meet the same phase matching conditions, the pump beam can be aligned around the signal at the same noncollinear angle as illustrated in fig. 7.3a. Application of this concept possesses scaling possibilities both in terms of pulse energy and average power. The concept has already been demonstrated successfully, incorporating three incoherent pump lasers. However, 10 % of the amplified energy are found in multiple beams due to parasitic second harmonic and sum-frequency generation. When using multiple coherent pump beams another problem arises. Interference, results in spatial intensity modulation and a transient grating is formed. This intensity modulation is not necessarily carried onto the amplified signal beam due to a smear out effect caused by the Poynting vector walk-off or slightly different noncollinear angles [128].

Another method to increase the pulse energy, which has not been suggested nor demonstrated so far, is amplification of multiple pump pulses within a single fiber amplifier. Each pulse then contains the maximum pulse energy that can be extracted from the fiber amplifier without damage or nonlinear distortions. To gain energy from all pump pulses, several amplifier stages or multiple passes through the parametric amplifier are required. The principle is displayed in fig. 7.3b for two pulses. In the first amplification pass the signal is temporally overlapped with the first pump pulse. The signal is parametrically amplified and the first pump pulse is depleted. Prior to the second amplification pass the signal pulse is temporally delayed with respect to the pump pulses. In consequence, the signal overlaps with the second pump pulse, gets amplified further, and depletes the second pump pulse as well.

It is worth mentioning that in principle the number of pump pulses is not limited, however the complex optical setup of the multi-pass or multistage parametric amplifier sets a practical limitation. Furthermore, the energy which can be extracted from the fiber amplifier within a very short time is limited. As already mentioned this amounts to ∼8 mJ per meter fiber length for the 85/200 rod-type PCF, 976 nm pump and 1030 nm emission wavelength. Nevertheless, a substantial increase in output pulse energy of fiber driven OPCPA seems feasible by using multiple pump pulses.

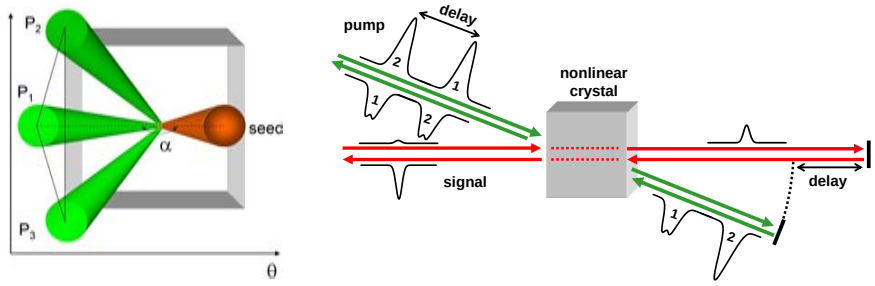

(a) (b)

Figure 7.3 – a) Illustration of a three beam pumped OPA whereas three pump beams (P1, P2, P3) amplify one seed beam [55], b) Single beam, two pump pulse scheme for pulse energy scaling.

Summary

In principle, the spectral bandwidth of an optimized OPCPA system which is pumped by sub-ps pulses can support sub-two cycle pulses. More sophisticated phase matching techniques, such as angular dispersed pump, will allow to extend the bandwidth to support single-cycle pulses as well.

Furthermore, optical parametric amplifiers can be scaled to higher pulse energy by increasing the crystal aperture. It has been experimentally shown that today's BBO crystals can handle 125 W average power at 515 nm without any thermal distortions and calculations indicate that thermo-optical distortions will appear if the kilowatt level is approached. By using special techniques, such as dividing the nonlinear crystals in thin slices or multiple cascaded OPAs, this limit could be shifted even further.

Consequently, the performance of future OPCPA systems will depend on the pump lasers. Yb-doped fiber amplifier systems are known for high average powers and 830 W of average power have been recently demonstrated with femtosecond pulses. Nonetheless, it will be a challenging task to achieve these average power levels with millijoule pulse energies in the future. Management or compensation of the nonlinear phase, which is known to distort the pulse quality, will allow for several millijoule pulse energy in sub-ps pulses from FCPA systems in the near future. Alternatively, pulses with several nanoseconds duration could fully extract the stored energy from a 85/200 rod-type PCF, which is in the order of 8 mJ per meter fiber length (976 nm pumping). In addition, multiple pump pulses or pump lasers can be employed to increase the pulse energy further.

As a result, fiber driven OPCPA systems will approach 1 mJ pulse energy in the future. The pulse durations could be reduced below 5 fs and the pulse peak power could be increased up to 0.1 TW. In addition, the repetition rates and average powers of such laser systems will be at least one order of magnitude higher than today's Ti:Sa amplifier systems.

8 Conclusion and Outlook

The main objective of this thesis was merging OPCPA technology with state-of-the-art high power fiber lasers in order to achieve high pulse peak powers with ultra-short pulses at the highest possible repetition rates. Based on modeling of the optical parametric amplifier, important requirements on the OPCPA pump were found which were adopted in choice and development of the pump laser later. Furthermore, the geometry of the optical parametric amplifier was optimized for ultra-broadband amplification in order to achieve the highest pulses peak power at the OPCPA output. Gain narrowing and saturation effects were investigated and in consequence a two stage design of the parametric amplifier was found to be most suitable for high conversion efficiency. Furthermore, a flat-top temporal pump pulse profile was identified to improve the conversion efficiency. In addition, parasitic nonlinear effects, such as SHG of signal and idler wave, were studied and configurations were found which effectively avoid these unwanted effects.

A mJ-FCPA system emitting sub-ps pulses was found as the most suitable pump laser for few-cycle OPCPA. In a first step it was employed to drive an OPCPA system at degeneracy, emitting 29 fs pulses with 2 GW peak power at 1030 nm central wavelength. Measurement of the output beam quality of this laser system revealed a remarkable value of $M^2 < 1.8$ which is beneficial for applications.

A further improvement in performance was achieved by employing an ultra-broadband Ti:Sa seed oscillator and rigorous optimization of the whole system in order to support the largest spectral bandwidth. Optical parametric amplification of a spectral bandwidth as large as 320 nm (-10 dB width) was achieved by applying the optimized noncollinear geometry at both amplifier stages. The amplified pulses were recompressed to few-cycle pulse durations as short as 8 fs and the achieved pulse peak power was as large as 6 GW. These values represent the shortest pulse duration and the highest peak power which has been reported for any fiber driven laser system so far. Compared to previous work on fiber driven OPCPA, an improvement of nearly three orders of magnitude in pulse peak power was achieved. It is also worth mentioning that the presented few-cycle OPCPA system was operated at a repetition rate as high as 96 kHz. Thus, the corresponding average power was as large as 6.7 W which represents a record value for high repetition rate few-cycle lasers. Such average power levels have not been achieved with post-compressed Ti:Sa lasers so far. In addition, a measurement of the carrier envelope phase revealed a standard deviation of 0.47 rad over a short measurement time.

Future developments should address the CEP stabilization on a longer timescale, offering

control of the electric field of the laser pulses which would open the way for many exciting applications in attoscience [10]. Even shorter pulse durations close to the Fourier-limit of 5.6 fs could be obtained in future by adaptive shaping of the spectral phase, incorporating pulse characterization techniques, such as FROG [129], SPIDER [102] or MIIPS [130]. In consequence, pulse peak powers in excess of 10 GW will be reached soon. Future scaling of few-cycle OPCPA towards 1 mJ output pulse energy and 0.1 TW pulse peak power can be expected from femtosecond FCPA pump lasers with prudent management of nonlinearity [33].

Additionally, an alternative approach has been explored with the development of an OPCPA system employing a ns-fiber amplifier as pump. As a result, the experimental setup is very compact and its size is comparable with Ti:Sa regenerative amplifiers. The laser system delivered Gigawatt peak power pulses with 35 fs pulse duration, demonstrating the potential of this approach. In principle, this laser system would support sub-20 fs pulse durations if an active phase shaper was implemented. Furthermore, this approach offers further scaling potential as longer pump pulses will allow for higher pump pulse energies. Even multiple fiber amplifiers could serve as OPCPA pump owing to the simple and compact setup. Such a laser system is a suitable candidate for substitution of today's regenerative Ti:Sa amplifiers being superior in all laser parameters especially in average output power.

In order to demonstrate the potential of the developed unique laser sources for applications, high harmonic generation was performed with the few-cycle OPCPA system using a Krypton gas target. High order harmonics were observed down to a wavelength of 20.9 nm which represents the shortest wavelength generated with a fiber based laser system so far. Compared to HHG with 800 fs pulses, delivered by the mJ-FCPA directly, the conversion efficiency of the HHG process is increased outstandingly by three orders of magnitude. The photon flux has been increased accordingly, approaching the µW average power level. Further improvement of this performance is essential to fulfill the FEL seeding requirements (nJ pulse energy per harmonic) and will potentially be achieved in future with quasi phase matching techniques [131] or two-color HHG schemes [132].

Lastly, the scaling potential of OPCPA to even higher average output powers was explored experimentally by high power SHG. The generation of 125 W average power at the second harmonic wavelength demonstrated impressively the high power capability of today's BBO crystals. Remarkably, the measured SHG efficiency remained unchanged when increasing the laser repetition rate, indicating that thermal dephasing is not an issue for second harmonic generation at this power level. Consequently, 100 W average power from fiber driven few-cycle OPCPA systems can be expected in the future, which will significantly improve the performance of many ultra-fast applications in the infrared as well as in the XUV spectral region and open the way for new exciting investigations in physics, chemistry and biology in the future.

Bibliography

[1] P. Hannaford, *Femtosecond laser spectroscopy* (Springer, 2005).

[2] A. Zewail, *Femtochemistry - Atomic scale dynamics of the chemical bond using ultrafast lasers* (World Scientific Printing Co., 2003).

[3] T. Udem et al., "Optical frequency metrology," Nature **416**, 233–237 (2002).

[4] M. Ferray et al., "Multiple-harmonic conversion of 1064 nm radiation in rare gases," Journal of Physics B: Atomic, Molecular and Optical Physics **21**, L31 (1988).

[5] E. Gagnon et al., "Soft X-ray-Driven Femtosecond Molecular Dynamics," Science **317**, 1374–1378 (2007).

[6] R. L. Sandberg et al., "Lensless Diffractive Imaging Using Tabletop Coherent High-Harmonic Soft-X-Ray Beams," Phys. Rev. Lett. **99**, 98–103 (2007).

[7] T. Haarlammert and H. Zacharias, "Application of high harmonic radiation in surface science," Current Opinion in Solid State and Materials Science **13**, 13–27 (2009).

[8] F. Kärntner, *Few-Cycle Laser Pulse Generation and Its Applications* (Springer, 2004).

[9] E. Goulielmakis et al., "Single-Cycle Nonlinear Optics," Science **320**, 1614–1617 (2008).

[10] F. Krausz and M. Ivanov, "Attosecond physics," Rev. Mod. Phys. **81**, 163–234 (2009).

[11] W. Ackermann et al., "Operation of a free-electron laser from the extreme ultraviolet to the water window," Nature Photonics **1**, 336–342 (2007).

[12] G. Lambert et al., "Injection of harmonics generated in gas in a free-electron laser providing intense and coherent extreme-ultraviolet light," Nature Physics **4**, 296–300 (2008).

[13] D. E. Spence et al., "60-fsec pulse generation from a self-mode-locked Ti:sapphire laser," Opt. Lett. **16**, 42–44 (1991).

[14] R. Ell et al., "Generation of 5-fs pulses and octave-spanning spectra directly from a Ti:sapphire laser," Opt. Lett. **26**, 373–375 (2001).

[15] M. Nisoli et al., "Compression of high-energy laser pulses below 5 fs," Opt. Lett. **22**, 522–524 (1997).

[16] C. Hauri et al., "Generation of intense, carrier-envelope phase-locked few-cycle laser pulses through filamentation," Applied Physics B: Lasers and Optics **79**, 673–677 (2004).

[17] I. Matsushima et al., "10 kHz 40 W Ti:sapphire regenerative ring amplifier," Opt. Lett. **31**, 2066–2068 (2006).

[18] A. Baltuška et al., "Visible pulse compression to 4 fs by optical parametric amplification and programmable dispersion control," Opt. Lett. **27**, 306–308 (2002).

[19] A. Dubietis et al., "Powerful femtosecond pulse generation by chirped and stretched pulse parametric amplification in BBO crystal," Optics Communications **88**, 437–440 (1992).

[20] G. Cerullo and S. Silvestri, "Ultrafast optical parametric amplifiers," Review of Scientific Instruments **74**, 1–18 (2003).

[21] R. Butkus et al., "Progress in chirped pulse optical parametric amplifiers," Applied Physics B: Lasers and Optics **79**, 693–700 (2004).

[22] A. Dubietis et al., "Trends in chirped pulse optical parametric amplification," IEEE Journal of Selected Topics in Quantum Electronics **12**, 163–172 (2006).

[23] F. Tavella et al., "90 mJ parametric chirped pulse amplification of 10 fs pulses," Opt. Express **14**, 12 822–12 827 (2006).

[24] I. P. Corporation", "IPG Photonics Successfully Tests Worlds First 10 Kilowatt Single-Mode Production Laser," press release (2009).

[25] T. Eidam et al., "Femtosecond fiber CPA system emitting 830 W average output power," Opt. Lett. **35**, 94–96 (2010).

[26] T. V. Andersen et al., "High repetition rate tunable femtosecond pulses and broadband amplification from fiber laser pumped parametric amplifier," Opt. Express **14**, 4765–4773 (2006).

[27] M. Aoyama et al., "0.85-PW, 33-fs Ti:sapphire laser," Opt. Lett. **28**, 1594–1596 (2003).

[28] J. Seres et al., "Sub-10-fs, terawatt-scale Ti:sapphire laser system," Opt. Lett. **28**, 1832–1834 (2003).

[29] Femtolasers, "Femtopower PRO product leaflet," (2010).

[30] J. Park et al., "Generation of 1.5 cycle 0.3 TW laser pulses using a hollow-fiber pulse compressor," Opt. Lett. **34**, 2342–2344 (2009).

[31] A. Roberts et al., "Optimization of few-cycle pulse generation: Spatial size, mode quality and focal volume effects in filamentation based pulse compression," Opt. Express **17**, 23 894–23 902 (2009).

[32] C. Ruillère, *Femtosecond Laser Pulses, Principles and Experiments* (Springer, 2003).

[33] D. N. Schimpf, *Pulse-shaping strategies in short-pulse fiber amplifiers*, Ph.D. thesis, Friedrich-Schiller-University Jena, Institute of Applied Physics (2010).

[34] M. E. Ferman, A. Galvanauskas, and G. Sucha, *Ultrafast Lasers, Technology and Applications* (Marcel Dekker Inc., 2003).

[35] G. P. Agrawal, *Nonlinear Fiber Optics* (Academic Press, 1995).

[36] R. L. Sutherland, *Handbook of Nonlinear Optics* (Marcel Dekker, 1996).

[37] P. A. Franken et al., "Generation of optical harmonics," Physica Review Letters **7**, 118–120 (1961).

[38] C. L. Tang et al., "Optical parametric processes and broadly tunable femtosecond sources," Applied Physics B: Lasers and Optics **58**, 243–248 (1994).

[39] G. M. Gale et al., "Sub-20-fs tunable pulses in the visible from an 82-MHz optical parametric oscillator," Opt. Lett. **20**, 1562–1564 (1995).

[40] I. N. Ross et al., "Analysis and optimization of optical parametric chirped pulse amplification," J. Opt. Soc. Am. B **19**, 2945–2956 (2002).

[41] A. Galvanauskas et al., "High-energy femtosecond pulse amlification in a quasi-phase-matched parametric amplifier," Opt. Lett. **23**, 210–212 (1998).

[42] G. D. Boyd and D. Kleinmann, "Parametric interactions of focused Gaussian light beams," Journal of Applied Physics **39**, 3597 (1968).

[43] D. Schimpf et al., "Theoretical analysis of the gain bandwidth for noncollinear parametric amplification of ultrafast pulses," J. Opt. Soc. Am. B **24**, 2837–2846 (2007).

[44] A. L. Oien et al., "Efficient, low-threshold collinear and noncollinear β-barium borate optical parametric oscillators," Opt. Lett. **22**, 859–861 (1997).

[45] A. V. Smith, "SNLO nonlinear optics code," AS-Photonics, Albuquerque.

[46] V. Petrov et al., "Femtosecond nonlinear frequency conversion based on BiBO," Laser & Photonics Reviews **4**, 53–98 (2010).

[47] B. Zhao et al., "Ultrabroadband noncollinear optical parametric amplification with LBO crystal," Opt. Express **16**, 18 863–18 868 (2008).

[48] B. C. Stuart et al., "Nanosecond-to-femtosecond laser-induced breakdown in dielectrics," Phys. Rev. B **53**, 1749–1761 (1996).

[49] S. Witte et al., "Generation of few-cycle terawatt light pulses using optical parametric chirped pulse amplification," Opt. Express **13**, 4903–4908 (2005).

[50] S. Witte et al., "A source of 2 terawatt, 2.7 cycle laser pulses based on noncollinear optical parametric chirped pulse amplification," Opt. Express **14**, 8168–8177 (2006).

[51] S. Adachi et al., "1.5 mJ, 6.4 fs parametric chirped-pulse amplification system at 1 kHz," Opt. Lett. **32**, 2487–2489 (2007).

[52] I. Jovanovicl, *Optical Parametric Amplification for High Peak and Average Power*, Ph.D. thesis, University of California, Berkeley (2001).

[53] G. Arisholm et al., "Limits to the power scalability of high-gain optical parametric amplifiers," J. Opt. Soc. Am. B **21**, 578–590 (2004).

[54] L. J. Waxer et al., "High-conversion-efficiency optical parametric chirped-pulse amplification system using spatiotemporally shaped pump pulses," Opt. Lett. **28**, 1245–1247 (2003).

[55] S. Alisauskas et al., "Prospects for increasing average power of optical parametric chirped pulse amplifiers via multi-beam pumping," Optics Communications **283**, 469–473 (2010).

[56] R. Paschotta, J. Nilsson, A. Tropper, and D. Hanna, "Ytterbium-doped fiber amplifiers," Quantum Electronics, IEEE Journal of **33**, 1049 –1056 (1997).

[57] O. Schmidt et al., "Millijoule pulse energy Q-switched short-length fiber laser," Opt. Lett. **32**, 1551–1553 (2007).

[58] F. Röser et al., "Millijoule pulse energy high repetition rate femtosecond fiber chirped-pulse amplification system," Opt. Lett. **32**, 3495–3497 (2007).

[59] D. Strickland and G. Mourou, "Compression of amplified chirped optical pulses," Optics Communications **56**, 219 – 221 (1985).

[60] E. Snitzer et al., "Double Clad, offset core Nd fiber laser," in *Optical Fiber Sensors* (1988).

[61] J. Limpert et al., "Extended single-mode photonic crystal fiber lasers," Opt. Express **14**, 2715–2720 (2006).

[62] L. Corporation, "Data sheet, LIEKKI Yb1200-6/125DC Single mode double clad ytterbium doped fiber," (2010).

[63] R. W. Boyd, *Nonlinear Optics* (Academic Press, 2002), 2nd edn.

[64] A. Smith et al., "Optical Damage Limits to Pulse Energy From Fibers," IEEE Journal of Selected Topics in Quantum Electronics **15**, 153–158 (2009).

[65] R. L. Farrow et al., "Peak-power limits on fiber amplifiers imposed by self-focusing," Opt. Lett. **31**, 3423–3425 (2006).

[66] R. T. Zinkstok et al., "High-power parametric amplification of 11.8-fs laser pulses with carrier-envelope phase control," Opt. Lett. **30**, 78–80 (2005).

[67] U. Morgner et al., "Sub-two-cycle pulses from a Kerr-lens mode-locked Ti:sapphire laser," Opt. Lett. **24**, 411–413 (1999).

[68] M. Schultze et al., "Few-cycle OPCPA system at 143 kHz with more than 1 μJ of pulse energy," Opt. Express **18**, 2836–2841 (2010).

[69] C. Teisset et al., "Soliton-based pump-seed synchronization for few-cycle OPCPA," Opt. Express **13**, 6550–6557 (2005).

[70] J. Limpert et al., "Low-nonlinearity single-transverse-mode ytterbium-doped photonic crystal fiber amplifier," Opt. Express **12**, 1313–1319 (2004).

[71] S. Hädrich et al., "Degenerate optical parametric amplifier delivering sub 30 fs pulses with 2 GW peak power," Opt. Express **16**, 19 812–19 820 (2008).

[72] J. Rothhardt et al., "500 MW peak power degenerated optical parametric amplifier delivering 52 fs pulses at 97 kHz repetition rate," Opt. Express **16**, 8981–8988 (2008).

[73] F. Röser, *Power scaling of ultrashort pulse fiber laser systems*, Ph.D. thesis, Friedrich-Schiller-University Jena, Institute of Applied Physics (2009).

[74] C. D. Brooks and F. D. Teodoro, "Multimegawatt peak-power, single-transverse-mode operation of a 100 μm core diameter, Yb-doped rodlike photonic crystal fiber amplifier," Applied Physics Letters **89**, 111–119 (2006).

[75] O. Schmidt, T. V. Andersen, J. Limpert, and A. Tünnermann, "187 W, 3.7 mJ from spectrally combined pulsed 2 ns fiber amplifiers," Opt. Lett. **34**, 226–228 (2009).

[76] W. Koechner, *Solid-State Laser Engineering* (Springer, Berlin, 2006), 6th edn.

[77] D. Nodop et al., "Wavelength-independent all-optical synchronization of a Q-switched 100-ps microchip laser to a femtosecond laser reference source," Applied Physics B: Lasers and Optics **94b**, 399–401 (2009).

[78] R. Kashyap, *Fiber Bragg gratings* (Academic Press, 1999).

[79] A. M. Weiner et al., "High-resolution femtosecond pulse shaping," J. Opt. Soc. Am. B **5**, 1563–1572 (1988).

[80] H. E. Bates et al., "Picosecond pulse stacking in calcite," Appl. Opt. **18**, 947–949 (1979).

[81] I. Will and G. Klemz, "Generation of flat-top picosecond pulses by coherent pulse stacking in a multicrystal birefringent filter," Opt. Express **16**, 14 922–14 937 (2008).

[82] I. Will, "Generation of flat-top picosecond pulses by means of a two-stage birefringent filter," Nuclear Instruments and Methods in Physics Research A **594**, 119–125 (2008).

[83] D. Schimpf et al., "Compensation of pulse-distortion in saturated laser amplifiers," Opt. Express **16**, 17 637–17 646 (2008).

[84] F. Li et al., "Shaping ability of all fiber coherent pulse stacker," Optics & Laser Technology **39**, 1120–1124 (2007).

[85] J. Rothhardt et al., "Generation of flattop pump pulses for OPCPA by coherent pulse stacking with fiber Bragg gratings," Opt. Express **17**, 16 332–16 341 (2009).

[86] D. Schimpf et al., "Control of the optical Kerr effect in chirped-pulse-amplification systems using model-based phase shaping," Opt. Lett. **34**, 3788–3790 (2009).

[87] J. Limpert et al., "High Repetition Rate Gigawatt Peak Power Fiber Laser-Systems: Challenges, Design, and Experiment," IEEE Journal of Selected Topics In Quantum Electronics **15**, 159–169 (2009).

[88] J. Rothhardt et al., "80 kHz repetition rate high power fiber amplifier flat-top pulse pumped OPCPA based on BiB_3O_6," Opt. Express **17**, 2508–2517 (2009).

[89] M. Pessot et al., "1000 times expansion/compression of optical pulses for chirped pulse amplification," Optics Communications **62**, 419–421 (1987).

[90] V. Bagnoud and F. Salin, "Influence of optical quality on chirped-pulse amplification: characterization of a 150-nm-bandwidth stretcher," J. Opt. Soc. Am. B **16**, 188–193 (1999).

[91] G. Cheriaux et al., "Aberration-free stretcher design for ultrashort-pulse amplification," Opt. Lett. **21**, 414–416 (1996).

[92] R. L. Fork, O. E. Martinez, and J. P. Gordon, "Negative dispersion using pairs of prisms," Opt. Lett. **9**, 150–152 (1984).

[93] R. Szipöcs et al., "Chirped multilayer coatings for broadband dispersion control in femtosecond lasers," Opt. Lett. **19**, 201–203 (1994).

[94] C. Homann et al., "Octave wide tunable UV-pumped NOPA: pulses down to 20 fs at 0.5 MHz repetition rate," Opt. Express **16**, 5746–5756 (2008).

[95] W. J. Tomlinson et al., "Compression of optical pulses chirped by self-phase modulation in fibers," J. Opt. Soc. Am. B **1**, 139–149 (1984).

[96] O. Martinez, "3000 times grating compressor with positive group velocity dispersion: Application to fiber compensation in 1.3-1.6 μm region," IEEE Journal of Quantum Electronics **23**, 59–64 (1987).

[97] J. H. Jang, I. H. Yoon, and C. S. Yoon, "Cause and repair of optical damage in nonlinear optical crystals of BiB_3O_6," Optical Materials **31**, 781–783 (2009).

[98] T. Fuji et al., "Monolithic carrier-envelope phase-stabilization scheme," Opt. Lett. **30**, 332–334 (2005).

[99] M. Nakazawa, T. Nakashima, and H. Kubota, "Optical pulse compression using a TeO_2 acousto-optical light deflector," Opt. Lett. **13**, 120–122 (1988).

[100] F. Tavella, *Multiterawatt few-cycle pulse OPCPA for applications in high-field physics*, Ph.D. thesis, LMU München (2007).

[101] L. Deng et al., "Improvement to Sellmeier equation for periodically poled LiNbO3 crystal using mid-infrared difference-frequency generation," Optics Communications **268**, 110–114 (2006).

[102] C. Iaconis and I. Walmsley, "Spectral phase interferometry for direct electric-field reconstruction of ultrashort optical pulses," Opt. Lett. **23**, 792–794 (1998).

[103] L. Gallmann et al., "Characterization of sub-6-fs optical pulses with spectral phase interferometry for direct electric-field reconstruction," Opt. Lett. **24**, 1314–1316 (1999).

[104] F. Tavella et al., "Fiber-amplifier pumped high average power few-cycle pulse non-collinear OPCPA," Opt. Express **18**, 4689–4694 (2010).

[105] F. Tavella et al., "Investigation of the superfluorescence and signal amplification in an ultrabroadband multiterawatt optical parametric chirped pulse amplifier system," New Journal of Physics **8**, 219 (2006).

[106] S. Adachi et al., "5-fs, multi-mJ, CEP-locked parametric chirped-pulse amplifier pumped by a 450-nm source at 1 kHz," Opt. Express **16**, 14 341–14 352 (2008).

[107] R. L. Sandberg et al., "Tabletop soft-x-ray Fourier transform holography with 50 nm resolution," Opt. Lett. **34**, 1618–1620 (2009).

[108] J. G. Eden, "High-order harmonic generation and other intense optical field-matter interactions: review of recent experimental and theoretical advances," Progress in Quantum Electronics **28**, 197–246 (2004).

[109] C. Winterfeldt et al., "Colloquium: Optimal control of high-harmonic generation," Rev. Mod. Phys. **80**, 117–140 (2008).

[110] P. B. Corkum, "Plasma perspective on strong field multiphoton ionization," Phys. Rev. Lett. **71**, 1994–1997 (1993).

[111] M. Lewenstein et al., "Theory of high-harmonic generation by low-frequency laser fields," Phys. Rev. A **49**, 2117–2132 (1994).

[112] M. V. Ammosov et al., "Tunnel ionization of complex atoms and of atomic ions in an alternating electromagnetic field," Soviet Physics - JETP **64**, 1191–1194 (1986).

[113] A. Paul et al., "Phase-matching techniques for coherent soft X-ray generation," IEEE Journal of Quantum Electronics **42**, 14–26 (2006).

[114] S. Hädrich et al., "High harmonic generation by novel fiber amplifier based sources," submitted to Opt. Express (2010).

[115] P. Salières et al., "Coherence Control of High-Order Harmonics," Phys. Rev. Lett. **74**, 3776–3779 (1995).

[116] T. Binhammer et al., "Prism Based Pulse Shaper for Direct Phase Manipulation of Octave Spanning Spectra," in *Conference on Lasers and Electro-Optics* (2005).

[117] J. Limpert et al., "Ultra-broad bandwidth parametric amplification at degeneracy," Opt. Express **13**, 7386–7392 (2005).

[118] C. Aguergaray et al., "Ultra-wide parametric amplificationat 800 nm toward octave spanning," Opt. Express **17**, 5153–5162 (2009).

[119] B. C. Walker et al., "Theoretical and experimental spectral phase error analysis for pulsed laser fields," J. Opt. Soc. Am. B **16**, 1292–1299 (1999).

[120] E. A. Khazanov and A. M. Sergeev, "Petawatt lasers based on optical parametric amplifiers: their state and prospects," Physics-Uspekhi **51**, 969 (2008).

[121] P. Russbueldt et al., "400W Yb:YAG Innoslab fs-Amplifier," Opt. Express **17**, 12 230–12 245 (2009).

[122] A. Giesen et al., "Scalable concept for diode-pumped high-power solid-state lasers," Applied Physics B: Lasers and Optics **58**, 365–372 (1994).

[123] D. Schimpf et al., "Controlling the influence of SPM in fiber-based chirped-pulse amplification systems by using an actively shaped parabolic spectrum," Opt. Express **15**, 16 945–16 953 (2007).

[124] H. J. Bakker, P. C. M. Planken, L. Kuipers, and A. Lagendijk, "Phase modulation in second-order nonlinear-optical processes," Phys. Rev. A **42**, 4085–4101 (1990).

[125] R. L. Farrow et al., "Numerical modeling of self-focusing beams in fiber amplifiers," Proc. SPIE **6453**, 645 309 (2007).

[126] O. Schmidt, *Leistungsskalierung kurzgepulster Faserlasersysteme*, Ph.D. thesis, Friedrich-Schiller-University Jena, Institute of Applied Physics (2010).

[127] D. Schimpf et al., "Circular versus linear polarization in laser-amplifiers with Kerr-nonlinearity," Opt. Express **17**, 18 774–18 781 (2009).

[128] D. Herrmann et al., "Investigation of two-beam-pumped noncollinear optical parametric chirped-pulse amplification for the generation of few-cycle light pulses," Opt. Express **18**, 4170–4183 (2010).

[129] R. Trebino and D. J. Kane, "Using phase retrieval to measure the intensity and phase of ultrashort pulses: frequency-resolved optical gating," J. Opt. Soc. Am. A **10**, 1101–1111 (1993).

[130] V. V. Lozovoy et al., "Multiphoton intrapulse interference. IV. Ultrashort laserpulse spectral phase characterization and compensation," Opt. Lett. **29**, 775–777 (2004).

[131] J. Seres et al., "Coherent superposition of laser-driven soft-X-ray harmonics from successive sources," Nature Physics **3**, 878–883 (2007).

[132] I. J. Kim et al., "Highly Efficient High-Harmonic Generation in an Orthogonally Polarized Two-Color Laser Field," Phys. Rev. Lett. **94**, 243 901 (2005).

Ehrenwörtliche Erklärung

Ich erkläre hiermit ehrenwörtlich, dass ich die vorliegende Arbeit selbständig, ohne unzulässige Hilfe Dritter und ohne Benutzung anderer als der angegebenen Hilfsmittel und Literatur angefertigt habe. Die aus anderen Quellen direkt oder indirekt übernommenen Daten und Konzepte sind unter Angabe der Quellen gekennzeichnet. Bei der Auswahl und Auswertung folgenden Materials haben mir die nachstehend aufgeführten Personen in der jeweils beschriebenen Weise unentgeltlich geholfen:

Alexander Heidt (Stellenbosch, Südafrika), Englischkorrektur

Weitere Personen waren an der inhaltlich-materiellen Erstellung der vorliegenden Arbeit nicht beteiligt. Insbesondere habe ich hierfür nicht die entgeltliche Hilfe von Vermittlungs- bzw. Beratungsdiensten (Promotionsberater oder andere Personen) in Anspruch genommen. Niemand hat von mir unmittelbar oder mittelbar geldwerte Leistungen für Arbeiten erhalten, die im Zusammenhang mit dem Inhalt der vorgelegten Dissertation stehen.

Die Arbeit wurde bisher weder im In- noch im Ausland in gleicher oder ähnlicher Form einer anderen Prüfungsbehörde vorgelegt. Teile dieser Arbeit wurden aus Prioritätsgründen bereits veröffentlicht oder zur Veröffentlichung eingereicht.

Die geltende Promotionsordnung der Physikalisch-Astronomischen Fakultät ist mir bekannt.

Ich versichere ehrenwörtlich, dass ich nach bestem Wissen die reine Wahrheit gesagt und nichts verschwiegen habe.

Jena, den 14.07.2010